Université de Pau et des Pays de l'Adour

École Doctorale Sciences Exactes et leurs applications

THÈSE DE DOCTORAT
Spécialité : Génie Électrique

présenté par

Martinus Dobbelaar

A study and realisation of nanosecond plasma exposure devices for biomedical applications

Conception et réalisation de systèmes d'exposition plasma pour des applications bio-médicales

---

dirigé par Pr Jean Paillol et co-dirigé par Philippe Lévêque

Soutenue le 22 décembre 2017

Pour le jury :

Les rapporteurs :

M. ZHADOBOV Maxim CR HDR	Université de Rennes
M. ZOUZOU Noureddine MC HDR	Université de Poitiers

Les autres membres :

M. GRENIER Katia CR HDR	LAAS-CNRS
M. PÉCASTAING Laurent Professeur	Université de Pau et des Pays de l'Adour
M. PAILLOL Jean Professeur	Université de Pau et des Pays de l'Adour
M. LÉVÊQUE Philippe Directeur CNRS	Université de Limoges

Les membres invités :

M. ANDRIEU Joël Professeur	Université de Limoges
Mme. ARNAUD-CORMOS Delia MC HDR	Université de Limoges
Mme. BESSIÈRES Delphine MC	Université de Pau et des Pays de l'Adour

Laboratoire des sciences pour l'ingénieur appliquées
à la mécanique et au génie électrique (SIAME)
EA 4581
Fédération de recherche CNRS IPRA FR 2952

Ecole Doctorale Sciences exactes et leurs applications
UPPA / UFR DEG
Avenue du Doyen Poplawski
BP 1633
F-64016 PAU CEDEX

Acknowledgments

Tout d'abord je voudrais remercier mon directeur de thèse Jean Paillol et Delphine Bessières (maître de conférences), pour toute leur aide et efforts pendant ma thèse depuis Pau et même de temps en temps à Limoges. La distance physique n'a pas toujours facilité le travail, mais grâce aux nombreux coups de fil et courriels on a réussi quand même.
Je tient aussi à remercier mon co-directeur de thèse Philippe Lévêque et Delia Arnaud-Cormos (habilitation à diriger des recherches [HDR]) pour leur aide, toutes nos réunions et le support technique à XLIM, malgré mes dispositifs plasma un peu particulier au sein de notre équipe.
Je remercie bien également le jury de ma soutenance et en particulier les rapporteurs qui ont lu et fait leurs rapports précieux dans un temps très restraint.
Puis un grand merci à mon secrétaire à XLIM Nadine Aymard.
Ensuite mes remerciements à Sylvia Bardet-Coste (maître de conférences) et Paul Daccord pour leur travail indispensable lors les expériences biologiques.
Un chaleureux merci à Damien Boudesocque, qui m'a vraiment aidé par automatiser le sauvegarde des données résultantes des mesures avec, notamment, l'oscilloscope. Sinon j'aurais dû utiliser les anciennes disquettes lentes. Notre temps commun dans la salle de manips m'a vraiment plu.
I also would like to thank my former office mates Miguel Angel Garcia-Fernandez, Malak Soueid, Sabrina Bentouati, Nathalie Ghazi and Amani Nefzi for their pleasant company and help.
Furthermore I want to express my gratitude towards my other (former) colleagues Nicolas Bui, Lynn Carr, Sergii Romanenko, Marta Wawrzyniak, Rod O'Connor (HDR) and Denise O'Connor for the nice times we have spent together.
A big and sincere *hubba hubba* to Ryan and Melanie Burke, who were much more than fantastic roommates during this last year. I wish you the best of luck at your new place and I will definitely see you soon.
I am very glad I met you, Ryan, in our lab and I want to thank you for who you are, for your help, your way of life and for wanting to share this with others in a very pleasant way and for being so nice, despite all the difficulties that you have encountered during your PhD. I hope we both find or create a satisfying job, which may bring us again really close to one another.
Jeg vil oprigtigt takke Stine for at være den sødeste kvinde i verden. Her vil jeg især gerne udtrykke min taknemmelighed for din hjælp med min afhandling, især ved bestilling af mine referencer, nogle artikler, for de super billeder af plasmaenhederne og for at ville komme helt til Sydfrankrig til min ph.d.-afhandling. Jeg elsker dig og glæder mig meget til at tilbringe resten af vores liv sammen.
Als laatste, maar zeker niet als minste, wil ik mijn geweldige en hele lieve ouders ontzettend bedanken. Voor alle steun in alle vormen en in al die jaren in Nederland, Frankrijk en

daarbuiten, voor alle gezelligheid, voor de fantastische opvoeding en jeugd van Vincent en mij die ons helemaal heeft gebracht waar we nu zijn.

Abstract

In this Ph.D. thesis, the nanosecond pulse method was implemented to generate Dielectric Barrier Discharges (DBD) and Surface Dielectric Barrier Discharges (SDBD) for plasma treatment of biological samples. The plasma was created using short (10-14 ns of FWHM) high-voltage (up to 11 kV) pulses of fast rise times (2-5 ns). The biological targets are cancer cells in a liquid culture medium contained in a standard Petri dish. Both exposure devices were designed in a same way (dimensions and polarity) and were inserted into the same experimental set-up, which is a waveguide matched by a load impedance. A high voltage tap-off measures the incident and reflected voltage pulses. The current is measured via a measure resistor in series with the discharge device, which ensures a large frequency bandwidth measurement.

The work was mainly experimental. We focused on the electrical characteristics of discharges. The electrical parameters, including the voltage across the air gap, the discharge current and the energy deposited into plasma per pulse, were given as a function of the measured waveforms. A same equivalent electrical circuit was proposed to model both ns-DBD and ns-SDBD devices. To support the experimental approach, we developed a numerical model based on the propagation equations along transmission line. The lumped elements of the equivalent circuit end the line. The model was used in the numerical treatment of experimental waveforms.

We first studied the electrical characteristics of discharges in a reference case without a Petri dish. In the ns-DBD configuration, the measured currents rise in 600 ps up to several tens of amperes. A negative current is still recorded after the voltage pulse ends. The discharge current presents a sharp peak, then the current decays to the trailing edge, and finally a peak of current of the opposite polarity is observed. It was related to the reversal of electric field sign in the gap because of a high surface charge density on the dielectric layer. The surface charges are then driven in the remaining plasma channel, that leads to a discharge current in the electrical circuit after the voltage pulse ends. The energy deposited into plasma per pulse is in the order of millijoule. In the ns-SDBD configuration, the characterization is more challenging as the discharge currents are very low (few amperes). We calculated the energy deposited per pulse in a range of tens of microjoules.

Then, we investigated the influence of the exposure conditions on discharges. The presence of the solution promotes reproducible results. In the case of the ns-DBD, the measured current waveforms are repeatable in terms of time-lag, amplitude and shape. The energy deposited per pulse is thus reproducible that is a key feature for exposure. For the ns-SDBD case, the solution has a weak influence on the deposited energy whatever the treatment distance. However the rise time of the voltage pulse has a strong impact on the energy. Finally, a preliminary study on biological treatment by ns-SDBD plasma was performed. Results revealed that the ns-SDBD plasma has an influence on the viability of the glioblastoma cells in the given conditions.

Résumé

Dans ce travail de thèse, la méthode des décharges nanosecondes a été mise en oeuvre afin générer des Décharges à Barrières Diélectriques (DBD) et des Décharges de Surface à Barrières Diélectriques (SDBD) pour le traitement plasma d'échantillons biologiques. Les plasmas ont été générés par des impulsions haute tension (jusqu'à 11 kV), très courtes (de 10 à 14 ns de largeur à mi-hauteur) et de temps de montée très brefs (2-5 ns). Les cibles biologiques sont des cellules cancéreuses cultivées dans un milieu biologique liquide placé dans une boîte de Pétri classique. Les deux systèmes d'exposition ont été conçus selon la même stratégie (dimensions et polarité), et s'insèrent dans le même montage expérimental qui est constitué d'un guide d'onde terminé par une impédance d'adaptation. Un diviseur de tension mesure l'impulsion de tension incidente et réfléchie. Le courant de décharge est mesuré via une résistance de mesure placée en série avec le système d'électrodes, ce qui permet d'obtenir une mesure sur une large bande de fréquence.
Le travail est principalement expérimental. Nous nous sommes intéressés aux caractéristiques électriques de la décharge. Les paramètres électriques, comprenant la tension aux bornes de l'intervalle d'air, le courant de décharge et l'énergie déposée dans le plasma par impulsion, sont définis en fonction des signaux mesurés. Un même circuit électrique équivalent a été proposé pour modéliser les deux systèmes d'exposition, ns-DBD et ns-SDBD. En appui de l'approche expérimentale, nous avons développé un modèle numérique basé sur les équations de propagation dans une ligne de transmission. Les éléments localisés du circuit équivalent terminent la ligne. Le modèle a été utilisé pour le traitement numériques des données expérimentales.
Nous avons d'abord étudié les caractéristiques électriques de la décharge sans boîte de Pétri, comme cas de référence. En configuration ns-DBD, le courant mesuré croît en 600 ps pour atteindre plusieurs dizaines d'Ampères. Un courant négatif est encore mesuré après la fin de l'impulsion de tension. Le courant de décharge présente un pic étroit, puis décroît jusqu'à la fin de l'impulsion de tension, et enfin un pic de polarité opposée est observé. Cette composante négative est due à l'inversion du champ électrique dans l'intervalle, causée par le stockage important de charges à la surface du diélectrique. Les charges sont alors transportées dans le canal de décharge résiduel. L'ordre de grandeur de l'énergie déposée par la décharge par impulsion est de l'ordre du millijoule. Dans le cas de la ns-SDBD, une caractérisation électrique de la décharge se révèle plus complexe car les courants mesurés sont de faible amplitude (quelques ampères). Nous avons néanmoins calculé l'énergie déposée dans le plasma par la décharge, elle est de l'ordre de quelques dizaines de microjoules par impulsion.
Ensuite, nous avons étudié l'influence des conditions d'exposition sur les décharges. La présence de la solution biologique dans la boite de Pétri est à l'origine d'une meilleure reproductibilité de la décharge. Dans le cas des décharges ns-DBD, les courants de décharge sont reproductibles en termes de temps d'apparition, d'amplitude et d'allure. L'énergie

déposée par la décharge est par conséquent aussi reproductible, ce qui est appréciable pour une exposition plasma. Dans la configuration ns-SDBD, la présence de la solution influence peu la valeur de l'énergie déposée par la décharge, quelque soit la distance de traitement. Par contre, le temps de montée de l'impulsion de tension a une influence importante sur l'énergie déposée. Enfin, une étude préliminaire a été réalisée sur le traitement de d'échantillons biologiques par plasma ns-SDBD. Les résultats montrent que le plasma généré a une influence sur la viabilité des cellules de type glioblastome exposées dans les conditions de l'étude.

Contents

Introduction

Motivation and Context

Cold plasmas in atmospheric pressure air have been used in many different applications during the past few years. Because of its high chemical reactivity, cold plasma treatment appears to be a promising solution for biomedical applications. In cold plasmas, electrons are heated up to a few tens of thousands of degrees Kelvin, while the heavy species such as neutral species or ions remain at room temperature. Cold plasmas are an appropriate solution for biological applications (Kong et al., 2009; Weltmann and Woedtke, 2017). Promising results have been obtained in cancer treatment (Vandamme et al., 2012; Chen et al., 2017; Lin et al., 2017).
A simple way to generate cold plasmas is to use electrodes at high-voltage separated by a gaseous gap. However, at atmospheric pressure, the originally cold plasma rapidly becomes a high-conducting junction that evolves into a thermal plasma. This discharge regime must be avoid for biological applications. Dielectric Barrier Discharge (DBD) is a solution to prevent this regime. DBDs are self-sustaining electrical discharges in electrode configurations containing an insulating material in the discharge path. This so-called dielectric barrier is responsible for the formation of a non thermal plasma at atmospheric pressure (Kogelschatz, 2003; Bazinette et al., 2016; Boisvert et al., 2017). The most common discharge regime is filamentary. Depending on the electrode configurations, the discharge develops in the gas volume or along the surface of the dielectric layer (Gibalov and Pietsch, 2000). Since the 1990s they have been explored for many applications, for example the biological decontamination of medical devices or as sources for the electric wind in aerodynamic control systems (Brandenburg, 2017).

Research on the use of non-thermal plasma effects in medicine can be split into two categories: direct plasma treatment and indirect plasma treatment. In direct plasma treatment, biological targets play the role of one of the two electrodes. Some current may then flow through the biological target. Direct plasma treatment can induce a flux of various active species (atoms and molecules and charged species), as well as radiation in the UV band to the surface of the biological sample. Nowadays two major families of devices for generating cold plasma for biological and medical applications are plasma jets and dielectric barrier discharges (DBDs). In jets, most of the plasma is generated at a distance of the target, and reactive species generated in the plasma are drifted via a carrier gas. Ionization waves can also produce some plasma at the treatment surface. In contrast DBDs generate plasma directly at the surface being treated. The active species deposited on target surfaces (charged particles and short-lived reactive species) are different between the two systems (Lin et al., 2017). Indirect plasma treatment mainly involves uncharged atoms and molecules that are generated in plasma. The active uncharged species are typically delivered to the surface via diffusion or flow of gas through a plasma region (Fridman et al., 2008). Recently a dielectric barrier discharge apparatus has been mounted just above a petri dish containing human cancer cells. Active species are produced within the discharge area and are melted in the medium, thus reaching biomolecules (Han and M, 2017).

The biological target can be biological tissues or cells. However cells to be treated can also be in biological sample. In that case the interface plasma-liquid plays a role. Plasma liquid interactions are complex, including plasma characteristics, the control of the reactivity transfer at the plasma-liquid interface and interfacial charging. Interfacial processes are still poorly diagnosed. Charging of liquid materials by dielectric barrier discharges and jets recently received a lot of attention. However the effect of plasma-liquid interfaces and the effect of solution properties is missing. On the other hand interfacial charging may play a role on the discharge dynamics. These aspects are still not well known (Adamovich et al., 2017).

The induction of apoptosis, i.e. the programmed cell death after plasma treatment, has been explored in the literature using different cell models. This effect has been used in typical cancer treatment applications. Scientific research on cancerous diseases has been carried out on the cytotoxic effect of plasmas, which can induce apoptosis of cancer cells in vitro (Fridman et al., 2007; Keidar et al., 2013; Ma et al., 2014). In particular, high concentrations of reactive oxygen species (ROS) generated by plasmas were able to induce a cytotoxic effect after destabilization of the mitochondrial membrane (Stoffels et al., 2006). On the other hand, the charge of the cell and its poration after application of nanosecond pulsed electric fields (nsPEF) can also contribute to the induction of apoptosis. More subtle damage such as damage to the cytoskeleton after deformity of the cell can affect the functionality of cells that can cause cell death (Bardet et al., 2016; Haas et al., 2017). Electric fields induced by the discharge may affect cell processes (Babaeva and Kushner, 2010).

This thesis is based on a partnership of two teams, Xlim (Limoges) and SIAME Laboratory (Pau). Xlim's group is experienced in delivery devices for exposure of biological cells to nanosecond pulsed electric fields (Bardet et al., 2016; Soueid et al., 2017). Cold plasma or ns-PEF interaction with cells are often studied separately (Carr et al., 2017). A potentially attractive objective is to combine these processes in order to study their interaction with biological media. In this context, the objective of this Ph.D. thesis is to study and realize nanosecond plasma exposure devices for biomedical applications :

- the first exposure device generates DBD on a nanosecond time scale (ns-DBD). The biological sample acts as an electrode. The discharges develops in the air gap between the dielectric layer and the biological sample. The exposure device is based on the work of Fridman's group (Lin et al., 2017).

- the second exposure device generates surface DBD on a nanosecond time scale (ns-SDBD). The discharge develops along the dielectric layer surface close to an active electrode. During the plasma exposure, the biological sample faces the discharge device. By contrast to the DBD configuration, the discharge is not in direct contact with the surface of the solution. The discharge device conception is in the continuity of the design of plasma actuators for flow control (Moreau et al., 2016) or for plasma assisted combustion systems (Soloviev et al., 2017).

Scope of the Ph.D. thesis

The biological targets are cancer cells in a liquid culture medium contained in a standard Petri dish. Both exposures devices are optimized for the given application in terms of dimensions, voltage polarity and prevention of electromagnetic interferences. The work is mainly experimental. We focus on the electrical characteristics of discharges. Electrical measurements are a part of the device circuit in order to monitor the electrical activity of the discharge during the plasma treatment.
Chapter I presents the basic principles of the nanosecond pulse method implemented for both exposure devices. The description of the experimental facility used in this work is detailed. We present an equivalent electrical circuit that stands for a suitable model for both ns-DBD and ns-SDBD devices. To support the experimental approach, we develop a numerical model in which the lumped elements of the equivalent circuit ends a transmission line. The developed model will be used for the numerical treatment of experimental waveforms in the next chapters.
Chapter II is dedicated to the ns-DBD exposure device. We describe the experimental set-up of the device. In exposure conditions, the discharge develops in the air gap between the dielectric layer and the solution that is the counter electrode. We will discuss on the difficulty in electrically modeling the solution. Therefore we study the discharge generated between the dielectric layer and a metallic plane cathode as a reference case. We present the electrical characteristics of the discharge. Then we carry out a preliminary study on the discharge in the exposure conditions.
Chapter III addresses the ns-SDBD device. We describe the experimental set-up of the device. In exposure conditions the Petri dish is located near the discharge. We present the

electrical characteristics of the discharge without a Petri dish. Then we study the influence of the exposure conditions on the discharge. Finally we present preliminary results of glioblastoma cells treated by ns-SDBD.

Introduction

Contexte

Les plasmas froids à pression atmosphérique sont utilisés dans de nombreuses applications depuis ces dernières années. Ils constituent une solution prometteuse dans le domaine bio-médical grâce à la chimie réactive générée. Dans un plasma froid, les électrons sont portés à quelques milliers de degrés Kelvin tandis que les particules lourdes restent à temperature ambiante. Les plasmas froids sont aujourd'hui une solution appropriée pour les applications biologiques (Kong et al., 2009; Weltmann and Woedtke, 2017). Ainsi des résultats prometteurs viennent d'être obtenus récemment dans le traitement du cancer (Vandamme et al., 2012; Chen et al., 2017; Lin et al., 2017).
Une façon simple de générer un plasma froid est d'utiliser un système d'électrodes séparées par un gaz, une électrode est portée à la haute tension l'autre est connectée à la masse. Cependant, à pression atmosphérique, le plasma froid généré devient rapidement très conducteur et évolue en plasma thermique. Ce régime de décharge doit être évité pour les applications bio-médicales. Les décharges à barrière diélectrique (DBD) sont une solution pour prévenir ce passage à l'arc. Les DBDs sont des décharges auto-entretenues générées par un système inter-électrodes présentant un matériau isolant sur au moins une des électrodes. Ces décharges à barrière diélectrique génèrent un plasma froid à pression atmosphérique (Kogelschatz, 2003; Bazinette et al., 2016; Boisvert et al., 2017). Le régime le plus commun est le régime filamentaire. Suivant la configuration du système, la décharge se développe en volume ou en surface du matériau isolant (Gibalov and Pietsch, 2000). Depuis les années 90, les DBD ont été étudiées dans le cadre de nombreuses applications comme, par exemple, la décontamination en milieu médical ou la création de flux d'air ionique pour le contrôle d'écoulement en aéronautique (Brandenburg, 2017).

Les applications des plasmas froids en médecine peuvent être séparées en deux catégories : le traitement plasma direct et indirect. Pour le traitement direct, la cible biologique joue le rôle d'une électrode. Une partie du courant peut alors traverser la cible. Le traitement plasma direct peut induire un flux d'espèces actives (atomes, molécules et espèces chargées) aussi bien que des radiations UV à la surface de l'échantillon à traiter. De nos jours, Il existe principalement deux façons de générer des plasmas froids pour un traitement direct en médecine: en utilisant un jet de plasma et en configuration DBD. Dans le cas des jets plasmas, les espèces sont créées à distance puis transportées vers l'échantillon dans un flux de gaz porteur. En revanche, les DBDs génèrent le plasma directement à la surface de l'échantillon à traiter. Les espèces actives créées sont différentes dans les deux cas (Lin et al., 2017). Le traitement plasma indirect fait plutôt intervenir des atomes ou des molécules non chargés électriquement. Ces espèces actives non-chargées

sont transportées vers la surface de la cible par diffusion ou dans un flux de gaz porteur (Fridman et al., 2008). Récemment un système reposant sur la génération de DBDs de surface a été placé à proximité de la surface d'un échantillon à traiter contenant des cellules cancéreuses. Les espèces actives produites par la décharge sont alors mélangées à l'air au-dessus l'échantillon (Han and M, 2017).
La cible biologique à traiter peut être un tissu ou des cellules biologiques. Dans le cas où les cellules à traiter sont dans une solution biologique, l'interface plasma-liquide joue un rôle. L'interaction entre le plasma et la surface d'un liquide est un problème complexe qui fait intervenir la nature du plasma, le contrôle du transfert de réactivité au liquide, et la charge électrique de l'interface. Les processus d'échange plasma-surface sont jusqu'à aujourd'hui méconnus. La charge électrique de l'interface par DBD et par jets commence à être abordée dans les études récentes. Cependant l'action du plasma sur la modification des propriétés du liquide n'est pas encore complètement décrite. Enfin la rétroaction de la charge de la surface sur la dynamique de la décharge n'est pas encore complètement comprise (Adamovich et al., 2017).
Le déclenchement de l'apoptose, i.e. la mort programmées des cellules, après traitement plasma a été étudiée dans la littérature grâce à différents modèles de cellule. Cet effet a été clairement utilisé dans le traitement du cancer (Fridman et al., 2007; Keidar et al., 2013; Ma et al., 2014). En particulier, les espèces d'oxygène réactif (ROS) produites par plasma induisent un effet cytotoxique après déstabilisation de la membrane mitochondriale (Stoffels et al., 2006). Par ailleurs la charge des cellules par l'application de champs électriques pulsés nanosecondes (ns-PEF) peut conduire à la mort cellulaire par électroporation. Des dommages plus subtils peuvent affecter la fonctionnalité des cellules et entraîner leur mort (Bardet et al., 2016; Haas et al., 2017). Les champs électriques dus au développement de décharges peuvent affecter les processus cellulaires (Babaeva and Kushner, 2010).

Les travaux présentés dans cette thèse sont basés sur la collaboration entre deux équipes, Xlim (Limoges) et le Laboratoire Siame (Pau). L'équipe d'Xlim est expérimentée dans l'application de ns-PEF à des cibles biologiques (Bardet et al., 2016; Soueid et al., 2017). Les effets du champ électrique ou du plasma sur les cellules biologiques sont classiquement étudiés séparement. Il a semblé pertinent de combiner ces deux techniques pour étudier leur action sur des milieux biologiques. Dans ce contexte l'objectif de la thèse est l'étude et la réalisation de systèmes d'exposition nanoseconde pour des applications bio-médicales :

- le premier système d'exposition réalisé permet de générer des décharges à barrière diélectrique à l'échelle nanoseconde (ns-DBD). L'échantillon biologique se comporte comme une électrode. La décharge se développe dans l'air entre le diélectrique et la cible biologique. Le dispositif d'exposition ns-DBD est clairement basé sur le travail du groupe de Fridman dans ce domaine (Lin et al., 2017).

- le second système d'exposition permet de générer des décharges de surface à l'échelle de la nanoseconde (ns-SDBD). La décharge se développe à la surface du diélectrique à proximité de l'électrode active. La cible biologique est située face au plasma pendant l'exposition. Contrairement au traitement par ns-DBD, le plasma n'est pas en contact direct avec la surface de la solution. Cette technique se place dans la continuité de travaux réalisés pour le contrôle de vol par actionneurs plasmas (Moreau et al., 2016), ou pour la combustion assistée par plasma (Soloviev et al., 2017).

Objectif de la thèse

Les cibles biologiques considérées sont des cellules cancéreuses cultivées dans un milieu biologique liquide au sein d'une boîte de Pétri classique. Les deux systèmes d'exposition sont optimisés en termes de dimensions, de polarité et de compatibilité électromagnétique. Le travail présenté est essentiellement expérimental. Nous nous sommes concentrés sur la caractérisation électrique des décharges. Les mesures électriques sont directement intégrées au dispositif d'exposition pour enregistrer l'activité électrique des décharges pendant le traitement plasma.

Le chapitre I présente les principes fondamentaux de génération de nano-impulsions de tension utilisées dans les deux systèmes d'exposition. Le dispositif experimental commun est détaillé. Nous introduisons un modèle électrique équivalent du circuit identique pour les deux systèmes, ns-SDBD et ns-DBD. En support de l'approche expérimentale, nous développons un modèle numérique basé sur un modèle de ligne de transmission terminée par les éléments localisés du circuit équivalent proposé. Ce modèle sera utilisé dans les chapitres suivants pour le traitement numérique des données expérimentales.

Le chapitre II est dédié au système d'exposition ns-DBD. Le dispositif expérimental est décrit. Dans les conditions d'exposition plasma, la décharge électrique se développe dans l'air entre la couche diélectrique sur l'électrode active et la surface de la solution, qui joue le role contre-électrode. Nous discuterons de la difficulté à modéliser électriquement la solution. Dans ce contexte le cas de référence choisi consiste à remplacer la solution biologique par un plan métallique. Les caractéristiques électriques de la décharge sont présentées. Puis nous présentons une étude préliminaire sur l'influence des conditions d'exposition sur la décharge.

Le chapitre III présente le dispositif d'exposition ns-SDBD. Le système expérimental est présenté. En condition d'exposition la décharge est générée à proximité de la surface de la solution biologique. La décharge est tout d'abord étudiée électriquement sans la solution biologique, puis l'influence des conditions d'exposition sur la décharge est présentée. Enfin, nous présentons des résultats préliminaires de traitement plasma de cellules cancéreuses de type glioblastome.

Chapter I

Experimental set-up and electrical characterization

Contents

I.1 Introduction

This chapter aims to present the experimental set-up and the concept of electrical characterization of both exposure devices, i.e. the nanosecond-pulsed dielectric barrier discharge (ns-DBD) plasma and the nanosecond-pulsed surface barrier discharge (ns-SDBD) plasma.

Section I.2 presents the experimental set-up for nanosecond pulse discharge generation. To initiate the discharges in atmospheric air we use two different power supplies that generate high voltage pulses (5 – 10 kV) of 10 – 14 ns duration, with a fast rise time of 2−5 ns. Due to the timescales related to nanosecond pulses, the wave nature of the carried signal can not be neglected. The exposure device is inserted into a waveguide matched by a load impedance to avoid reflected pulses. Subsequently we present the voltage and current measurements. A high voltage tap-off is used to measure the incident and reflected voltage pulses. The current is measured via a measurement resistor in series with the discharge device. It ensures a large frequency bandwidth required to measure nanosecond pulsed discharge currents. Finally we present an equivalent circuit to outline the concept of the experimental set-up. The main characteristics of the whole system are detailed.

To complete the characterization of the experimental setup, Section I.3 presents a study on the reflection of nanosecond pulse voltage. The study is performed in the frequency domain and in the time domain. In the latter case we develop a numerical model based on the propagation equations along a transmission line. The equations are solved using a standard one dimensional finite difference time domain (FDTD) method. Simulations of incident and reflected voltage pulses are presented.

In Section I.4 we propose an equivalent electrical circuit that stands for a suitable model for both ns-DBD and ns-SDBD devices. The measured current is the total current flowing through the device, the discharge current is just one of its components. To characterize the discharge current component of the total measured current, we will present numerical circuit simulations. Simulations are based on the transmission line model developed in Section I.3. The lumped elements of the equivalent circuit will end the line, and a simplified model of a discharge is used. The developed model will be used in the numerical treatment of experimental waveforms in the next chapters. Finally, we present the experimental approach to determine electrical parameters of discharges. These parameters, including discharge current and voltages across the air gap and the dielectric layer, are given as a function of the measured waveforms according to the proposed equivalent circuit. An expression for the energy deposited per pulse by the plasma is also given.

I.2 Experimental set-up

A general experimental setup for nanosecond pulse discharges exposure of biological media is composed of a high-voltage pulse generator, an exposure device and measurement, and monitoring equipment. Figure I.1 presents a schematic of the experimental set-up.

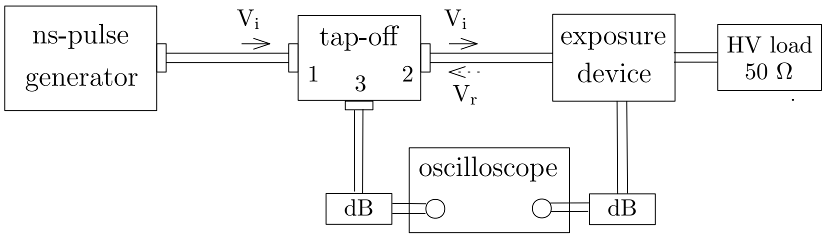

Figure I.1: Schematic of the experimental set-up.

I.2.1 Voltage pulses generation

To initiate plasma discharges we used two generators. The first pulse generator (FPG 10-1SM10 FiD Technology, Burbach, Germany) is a high-voltage generator delivering 14− ns duration pulses with adjustable voltage amplitude up to 10 kV. The rise time is approximately 4 ns and the pulse repetition frequency is adjustable up to 1 kHz. The second pulse generator (FPG 20-1NJ10 FiD Technology, Burbach, Germany) is a high-voltage generator that can deliver voltage of amplitude up to 20 kV. The pulse duration is adjustable from 1 to 10 ns; the rise time is approximately 2 ns. The pulse repetition frequency is adjustable up to 1 kHz.
Figure I.2 shows typical voltage pulses delivered by these two generators and their Fourier transforms. The decrease of the pulse generated by the 10 kV generator is followed by a plateau with non-negligible amplitude (20% of the maximum), and its duration is around 12 ns. This plateau is due to an internal reflection in the generator. As both pulse durations are similar, the amplitudes of the Fourier transform are similar at low frequency. The useful −20 dB bandwidth is same at 65 MHz. The main difference between pulses is the rise time that is two times larger for the 10 kV pulse generator. This leads to a difference at high frequency : the pulse voltage presents a significative energy (above the noise level) up to 400 MHz for the 10 kV pulse generator and up to 800 MHz for the 20 kV pulse generator. Therefore we mainly used the 10 kV pulse generator to study the discharges. However for a long-time used at a high repetition rate the 20 kV generator is preferred. Results obtained with the 20 kV generator will be studied in regard with those obtained with the 10 kV generator.

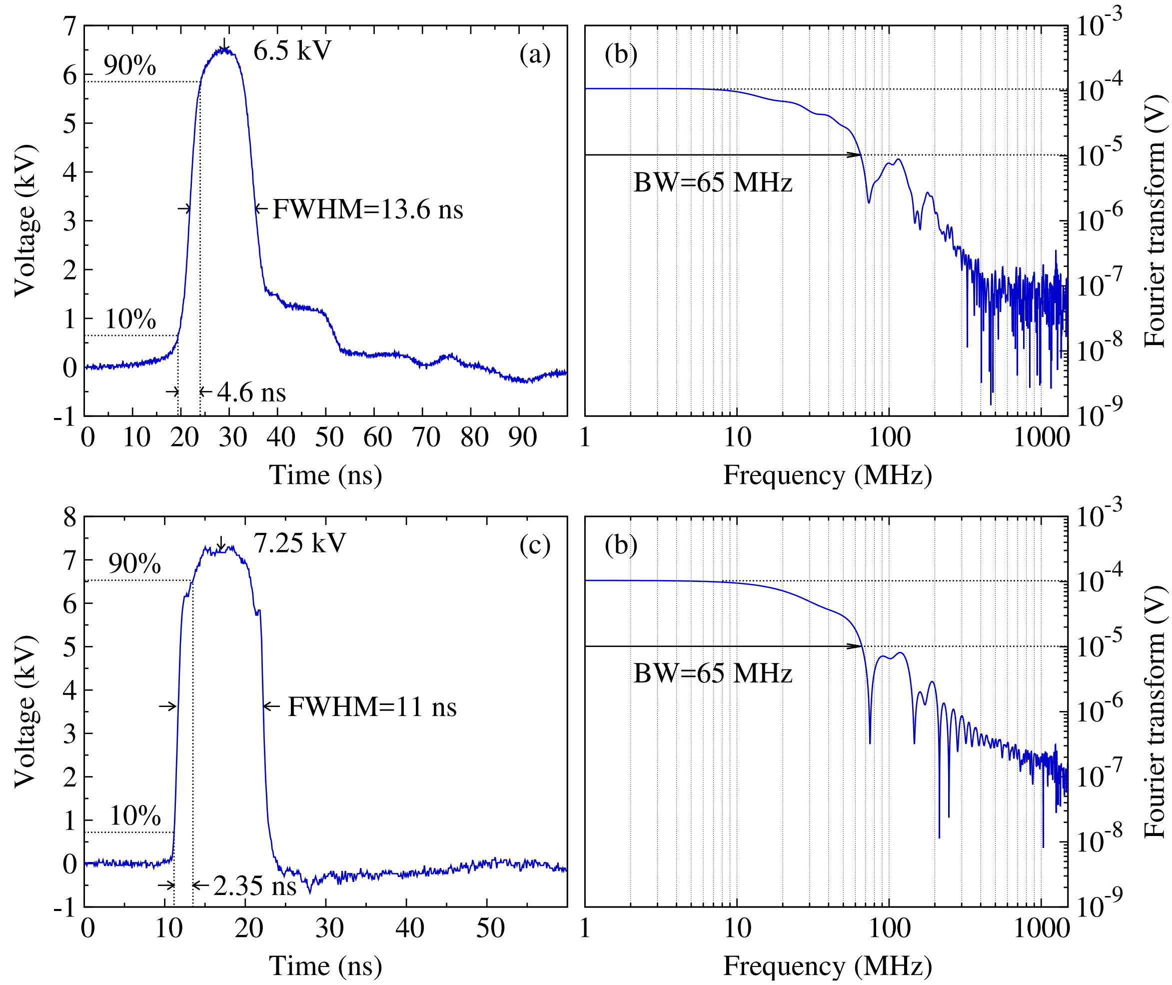

Figure I.2: Voltage pulses delivered by the 10 kV pulse generator (a) and by the 20 kV pulse generator (c). Fourier transform of pulses (b) and (d).

I.2.2 Connection and monitoring

To apply the nanosecond pulse voltage to the exposure device we use a HV coaxial cable (N cable) presenting a 50 Ω impedance. The maximum input voltage is 5.5 kV in DC. We assume that losses in the cable are negligible. Exposure devices are connected to the coaxial cable with HN connectors of 50 Ω impedance and a frequency bandwidth up to 3 GHz.

In order to acquire voltages, 10 dB, 20 dB and 30 dB attenuators are added. Their characteristic impedance is 50 Ω with a frequency bandwidth up to 3 GHz at least. The measured pulses are displayed on a 3 GHz bandwidth oscilloscope (DSO, TDS 694C, Tektronix, USA) presenting a sample rate of 10 GS/s and 50 Ω input impedance.

I.2.3 Impedance matching

The pulse generators have not a protective device to prevent them being damaged by reflected pulses, at long-time use. To reduce reflection the system is terminated by a matching load of 50 Ω impedance. The maximum input voltage of the high voltage load (2051-GHMP, Barth electronics, USA) is 10 kV during 100 ns. Figure I.3 shows impedance and reflection coefficient of the HV load. The real part of impedance is 50 Ω with a zero imaginary part till 300 MHz. The reflection coefficient shows a resonance at 850 MHz. The load impedance can be thus considered as an ideal 50 Ω resistor on a frequency bandwidth of 300 MHz.

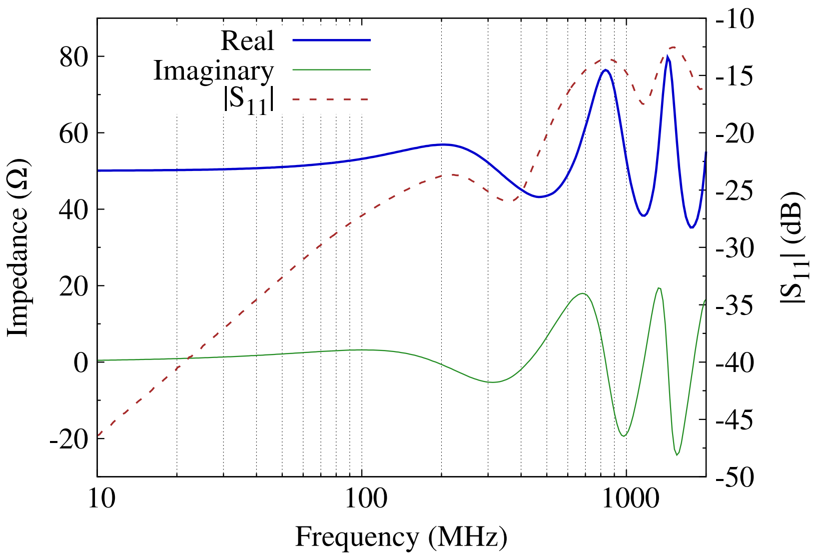

Figure I.3: Frequency characterization of the HV 50 Ω load. Reflexion coefficient, real and imaginary parts of the impedance.

The discharge device is thus inserted into a waveguide matched by a load impedance to reduce reflected pulses. However if apertures exist in the external conductors of the exposure device, common mode current has to be regarded. Figure I.4 shows the common mode current flowing the external conductor of the experimental set-up. A stray capacitance naturally exists in between the outer conductor of the device and the ground. Note that the exposure device is grounded by the stray capacitance. The common mode current flows around the loop : along the ground shielding mesh of the cable, through the stray capacitor in between the outer conductor of the device and the ground, and on the ground towards the generator. This current can generate electromagnetic interferences (EMI). In practical terms one limits EMI by reducing the loop surface. The matching impedance also contributes to reducing EMI.

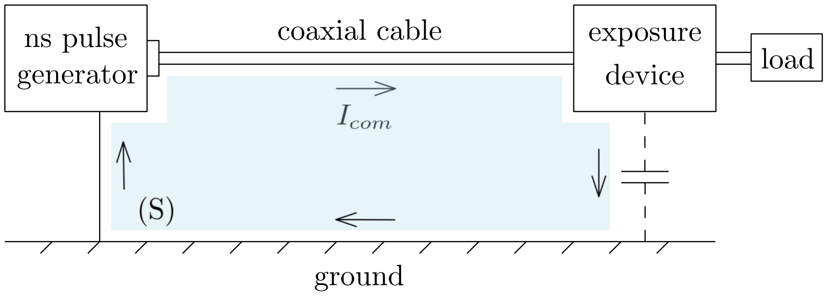

Figure I.4: Common mode current, I_{com}, flowing the external conductor of the set-up around the loop of surface S.

I.2.4 Voltage and current measurements

The high voltage pulse measurement requires a wide band. The HV pulse is measured via a tap-off (Model 241, Barth electronics, USA) connected between the generator and the device (Kenaan et al., 2011). The tap-off characterizes the incident and reflected pulses as seen in Figure I.1. The tap-off is a voltage divider of ratio 1/1 on the primary line (between port 1 and port 2) and 1/100 on the second line (between port 1 and port 3). It presents a minimal rise time through the mainline of 30 ps but of 1.5 ns through the second line. In other words, the measured rise time of the voltage pulse will be minimum equal to 1.5 ns. To determine frequency performance of the tap-off, we measured scattering parameters. Figure I.5 shows the S_{11} reflection coefficient as well as the S_{31} transmission coefficient. S_{11} parameter shows a very weak attenuation of the primary line signal without distortion. However S_{31} parameter reveals a useful −3 dB bandwidth of the measure line of only 270 MHz. The measured voltage waveform is then undistorted up to 270 MHz.

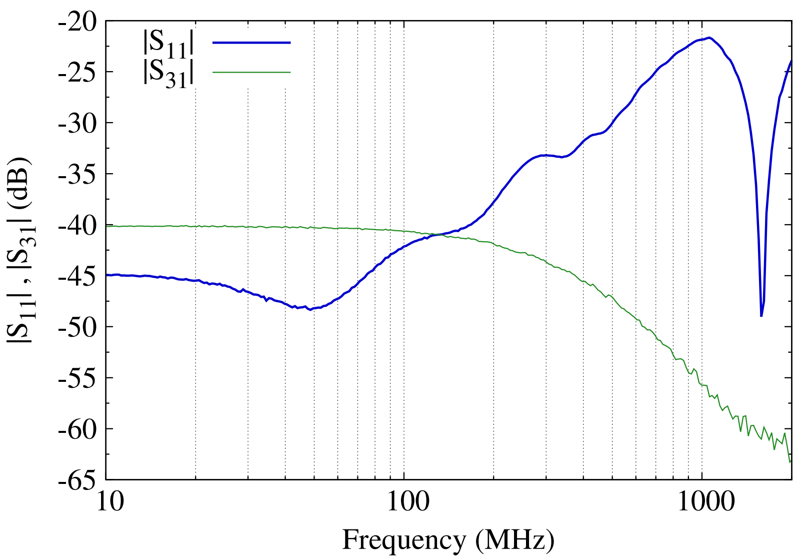

Figure I.5: Frequency characterization of the tap-off. Reflexion coefficient S_{11} and transmission coefficient S_{31}.

The discharge current pulse also has to be measured without a significant frequency bandwidth limitation. A common way is to use current probes as Rogowski coils (Benard et al., 2012; Pai, 2008; Shao et al., 2009; Zhang et al., 2006) inserted in series between the device and its outer conductor. In this work, we can not use this technique because of the discharge device dimension. To apply plasma directly to biological targets, exposure devices will be designed in circular shapes with a diameter just below a Petri dish (3.5 cm). Current probes are then too large to be inserted into the waveguide. Another technique is to use a back shunt resistor in series to the ground shielding mesh of the HV cable, in an open ended circuit. The discharge current is then calculated by comparing the incident current pulse to the reflected one (Anikin et al., 2004; Correale et al., 2015; Starikovskaia et al., 2010; Liu et al., 2014). This technique can be applied here by using the HV tap-off. However the measured rise time is limited to 1.5 ns. An alternative technique is the usage of a shunt resistor (Dawson and Little, 2013; Takashima et al., 2011a) in series with the discharge device and the ground. The impedance of the shunt resistor is negligible.
In this work, we use the same approach. However the measure resistor impedance is of 50 Ω. It should be noted that such a value is not negligible in the equivalent impedance of the experimental set-up. In practical terms, the measure resistor is made of a 50 Ω impedance coaxial cable ended by the 50 Ω input impedance of the oscilloscope. Thus the bandwidth is only limited by the input bandwidth of the oscilloscope and attenuators, i.e. 3 GHz. This technique was applied in (Arnaud-Cormos et al., 2014) to measure NRPD current pulses with rise time less than 1 ns (in a point-to plane electrodes system).This measurement is also used at low frequency (Bessières et al., 2004; Naudé et al., 2005; Bouzidi et al., 2014).

I.2.5 Equivalent electrical circuit

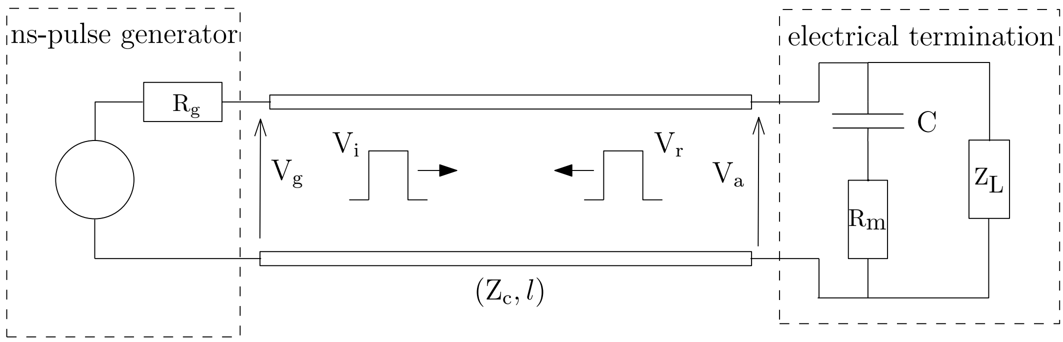

Figure I.6: Schematic of the electrical circuit for applying the voltage pulse and for measuring the current. $Z_c \equiv Z_L \equiv R_m = 50\ \Omega$.

Figure I.6 outlines the concept of the set-up equivalent electrical circuit. The voltage, V_g, delivered by the pulse generator is guided to the line termination using the coaxial cable of characteristic impedance $Z_c = 50\ \Omega$ and length l. A sufficiently long cabling should be used to avoid superposition of the incident and reflected pulse. V_a is the voltage actually applied to the electrical termination. The electrical termination represents the exposure device and the measure resistor. In a simple way both ns-SDBD and ns-DBD devices consist in two electrodes, one of which at least is covered with a dielectric layer, and an air gap where discharge develops. This is electrically modeled by one equivalent capacitor C as a first approximation. The discharge device is inserted into the waveguide matched by the 50 Ω load impedance. At the device location, the impedance due to the matched load is 50 Ω. The load impedance is thus considered as a lumped circuit element and denoted Z_L. The same assumption is applied to the measurement resistor, R_m. It should be noted that the tap-off is not modeled in the electrical circuit since it causes no distortion of waveforms over a 2 GHz bandwidth. This electrical circuit stands for a waveguide to apply and measure the pulse voltage, as well as to measure the current.

I.3 Reflection of voltage pulses

To complete the characterization of the experimental setup, we study reflection of nanosecond voltage pulse. We consider the circuit termination in Figure I.6 in which only the device capacitance can vary. We first determine the influence of the device capacitance on the reflection coefficient in the frequency domain. Then we study the reflection in the time domain. We developed a model of transmission line based on the telegrapher's equations. The equations are solved using a standard one dimensional finite difference time domain (FDTD) method. The model is briefly presented before showing the results of simulations on the incident and reflected pulses. The transmission line is ended by the lumped elements depicted in Figure I.6. We evaluate the reflection in view of capacitance variations but also stray inductance which can participate to a reflection increase.

I.3.1 Reflection in the frequency domain

Let's consider the reflection coefficient of the electrical circuit in Figure I.6

$$\Gamma(\omega) = \frac{Z - Z_c}{Z + Z_c} \quad \text{with} \quad Z = \frac{Z_L(1 + iR_m C\omega)}{1 + i(Z_L + R_m)C\omega}, \tag{I.1}$$

with $Z_c = R_m = Z_L = 50\ \Omega$.
Z is the equivalent impedance of the electrical termination. It tends to 50 Ω at low frequency but tends to 50 Ω/2 at high frequency.
Figure I.7 compares modulus of the reflection coefficient for various capacitances as a function of frequency. The range of capacitance is $1-20$ pF according to DBD and SDBD device dimensions. The reflection coefficient increases with capacitance for a given frequency. Using the matching impedance Z_L, the modulus tends to zero at low frequency and to a limit value of only 1/3 at high-frequency.

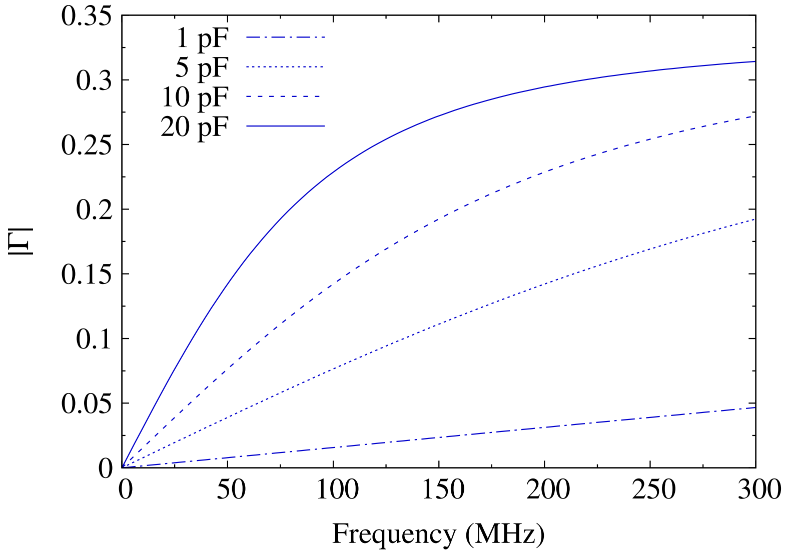

Figure I.7: Modulus of the reflection coefficient as a function of frequency for C = 1−20 pF.

I.3.2 Reflection in the time domain

Model formulation

In the nanosecond timescale, the propagation equations along transmission lines have to be solved to determine the reflected pulse due to the exposure device.
Standard methods for analyzing the propagation characteristics of transmission lines relies on the use a classical lumped element electrical model of the line. Losses are not considered during the propagation in the cable. The model is then constructed by considering the inductance and capacitance along a fixed length of the line, as depicted in Figure I.8. The length, along z axis, of a very short element of line is denoted Δz. The change in amplitude of voltage and current of a signal by passage through this element can be determined thanks to Kirchhoff's circuit laws

$$\begin{aligned} i(z,t) - i(z+\Delta z,t) &= \mathrm{C}_l \Delta z \frac{\partial v(z+\Delta z,t)}{\partial t}, \\ v(z,t) - v(z+\Delta z,t) &= \mathrm{L}_l \Delta z \frac{\partial i(z,t)}{\partial t}, \end{aligned} \tag{I.2}$$

with L_l the self-inductance for an unit length (in H / m) and C_l the capacitance for a unit length (in F / m).

A complete line can be viewed as a cascade of n_z very short elements of line as seen is Figure I.8. At any point of the line, the current and the voltage depend both on line position z and time t. This leads to the following set of partial differential equations

$$\begin{aligned} \frac{\partial i(z,t)}{\partial z} &= -\mathrm{C}_l \frac{\partial v(z,t)}{\partial t}, \\ \frac{\partial v(z,t)}{\partial z} &= -\mathrm{L}_l \frac{\partial i(z,t)}{\partial t}. \end{aligned} \tag{I.3}$$

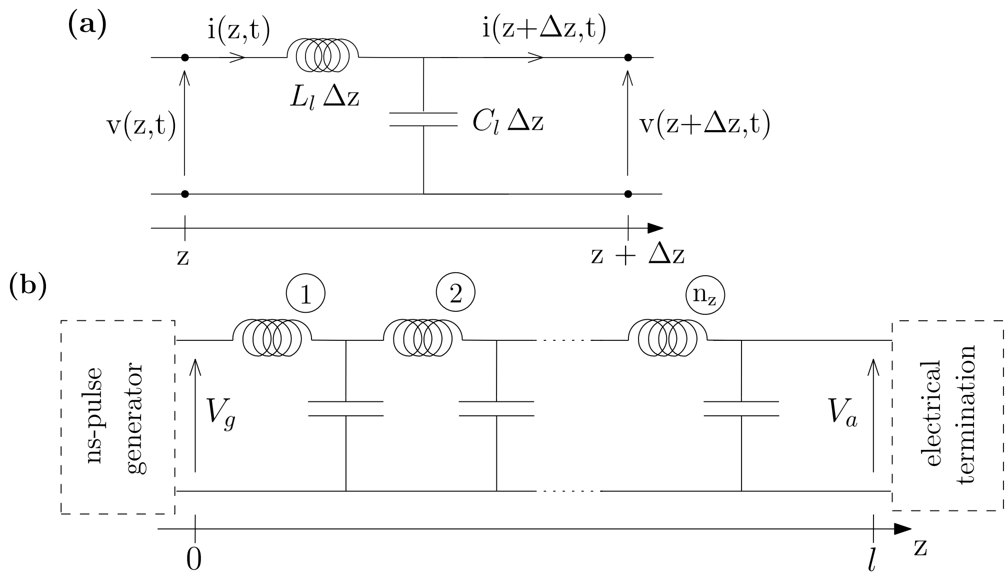

Figure I.8: Models of an element of line a) and the network b).

The propagation velocity of waves along the line is $1/\sqrt{L_l C_l} = 2\times10^8$ m/s and the characteristic impedance of the line is $\sqrt{L_l/C_l} = 50\ \Omega$.
The closing conditions are obtained by applying Kirchhoff's circuit laws at the lumped elements of the ends of line. The set of equations is solved using a standard one dimensional FDTD method.

Results and discussion

The ends of line are the lumped components of electrical circuit depicted in Figure I.6. The receiving end voltage is the voltage V_a actually applied to the electrical termination. The sending voltage is delivered by pulse generators, V_g. Shape of these voltage pulses differ from square waveforms, with a non zero component remaining after the pulse (as shown in Figure I.2). For a sake of simplicity we assume an *ideal* voltage pulse for modeling. Figure I.9 compares the *ideal* pulse with a standard pulse delivered by the 10 kV - pulse generator. The key features are similar, i.e. amplitude, rise time and FWHM.

Figure I.10 presents the incident and reflected pulses at the ends of the line. The line stands is a 10 m long coaxial cable. The device capacitances considered are 10 pF and 20 pF. The timescale is chosen to observe the total reflection. The time origin is imposed by the voltage pulse delivered by the generator. The incident pulse V_i is the *ideal* pulse V_g. It propagates during 50 ns, it is applied to the load and reflected in the same time. The reflection is composed of two pulses due to the high frequency mismatch, i.e. during rise and fall times of the incident pulse. The first pulse is negative because the equivalent impedance of the electrical termination is lower than the characteristic impedance of the cable. Then, the reflection is fully absorbed by the output impedance of the generator and

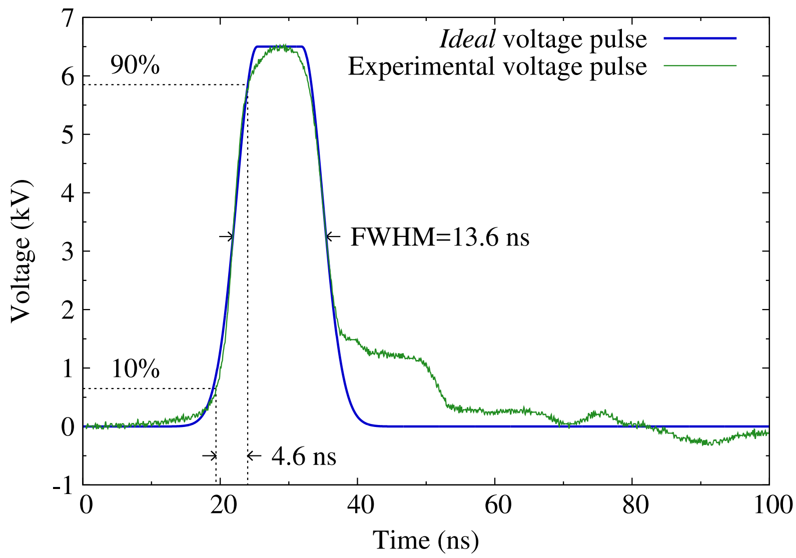

Figure I.9: Experimental voltage pulse and *ideal* voltage pulse for modeling.

no reflected signals remains. The applied voltage is the sum of the incident and reflected pulses. Note that one can also access to $V_a(t)$ by reconstructing : $V_a(t) = V_i(t - t_p) + V_r(t + t_p)$ with $t_p = 50$ ns the propagation time.

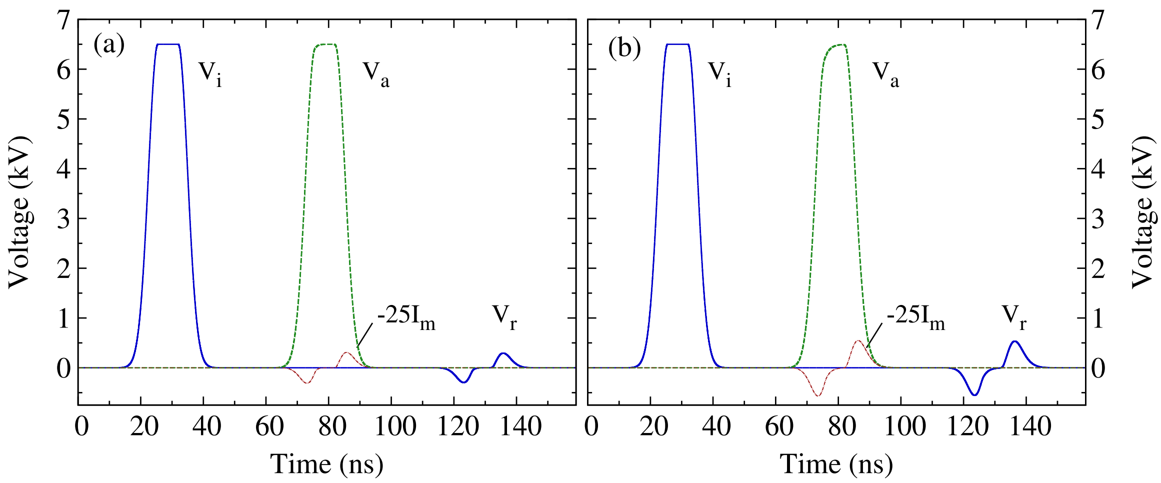

Figure I.10: Incident V_i and reflected V_r pulses (solid lines) at the input of the line and applied voltage pulses V_a to the electrical termination (dashed line) for C = 10 pF (a) and C = 20 pF (b). I_m is the current flowing the measure resistor.

The amplitude of reflected pulses increase with the device capacitance C. For C = 20 pF, it is about 10% of the incident pulse. In other words, less than 5% of the incident pulse energy is reflected towards the generator. So only a weak percentage of the incident pulse energy is reflected toward the generator, even for a high value of capacitance. Numerical results show the efficiency of the circuit matching by the load impedance.

Figure I.10 also compares the current flowing through the measure resistor I_m and the reflected voltage. The reflected current and voltages are linked up with

$$V_r(t) = \frac{Z_L - Z_c}{Z_L + Z_c} V_i(t) - \frac{Z_L Z_c}{Z_L + Z_c} I_m(t) = -\frac{50}{2} I_m(t) \tag{I.4}$$

when placing at the termination. The reflection is only due to the current flowing through the measure resistor.

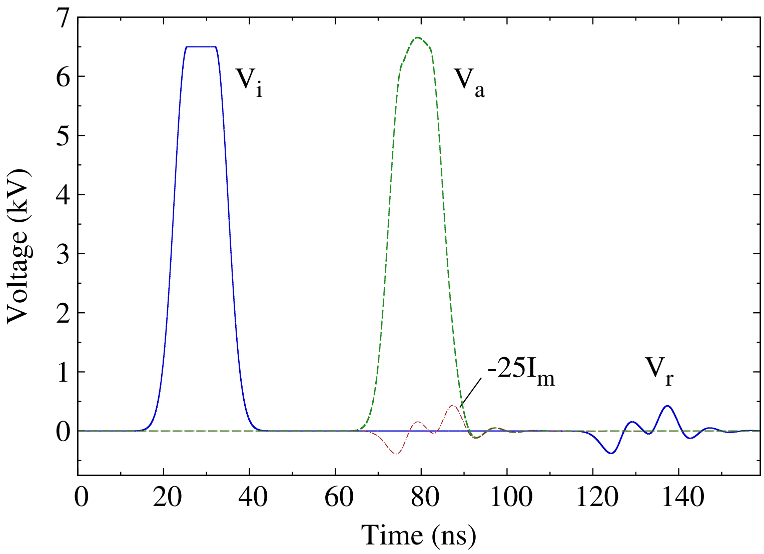

Figure I.11: Incident V_i and reflected V_r pulses (solid lines) at the input of the line and applied voltage pulses V_a to the electrical termination (dashed line) for C = 10 pF and a stray inductance of L = 0.2 μH. I_m is the current flowing the measure resistor.

In addition, stray inductance due to connections can not be neglected at high frequency. Thereby we study the effects of a self inductance in series with the measure resistor. The capacitance is 10 pF. The value of the inductance is chosen to be the maximum value that can be found in experiments : L = 0.2 μH for a wire connexion 20 cm long and of 2.5 mm diameter (Grover, 2009). Figure I.11 shows that the stray inductance causes oscillations in the voltage reflected pulse, and so over-voltages on the applied voltage V_a. Oscillations are evident also for the measured current pulses. In practical terms, the only way to reduce stray inductance effects is to minimize connection length.

I.4 Discharge electrical parameters

When considering dielectric barrier discharges, a classical electrical characterization consists in calculating the electrical parameters (voltages and currents) according to a known equivalent circuit (Liu and Neiger, 2003). So far for a sake of simplicity the exposure device was modeled by one capacitor. A classical equivalent electrical circuit of a DBD involves at least two capacitances to model the air gap where the discharge develops and one dielectric layer.

The equivalent circuit of our exposure devices now includes these two capacitances in series, C_{air} and C_{diel}. A stray capacitance C_p is also put in parallel. This equivalent circuit is similar to the one proposed by (Naudé et al., 2005) to determine the electrical parameters of DBD in a Townsend regime at atmospheric pressure. In this work, we consider this approach for nanosecond pulse excitation.

Figure I.12 shows the equivalent circuit included into the waveguide. The discharge is symbolized by closing a switch and forcing some of the current through the plasma channel, whose resistance $R_d(t)$ rapidly changes with time (Kogelschatz, 2003). A stray inductance is added in series with the measure resistance to model connexions that can not be neglected at high frequency (as discussed in Section I.3.2). This equivalent circuit stands for a suitable model for the ns-pulse DBD device as well as ns-pulse SDBD device. This will mainly depend on the stray capacitance value that is preponderant in the case of SDBD and weak in the DBD configuration.

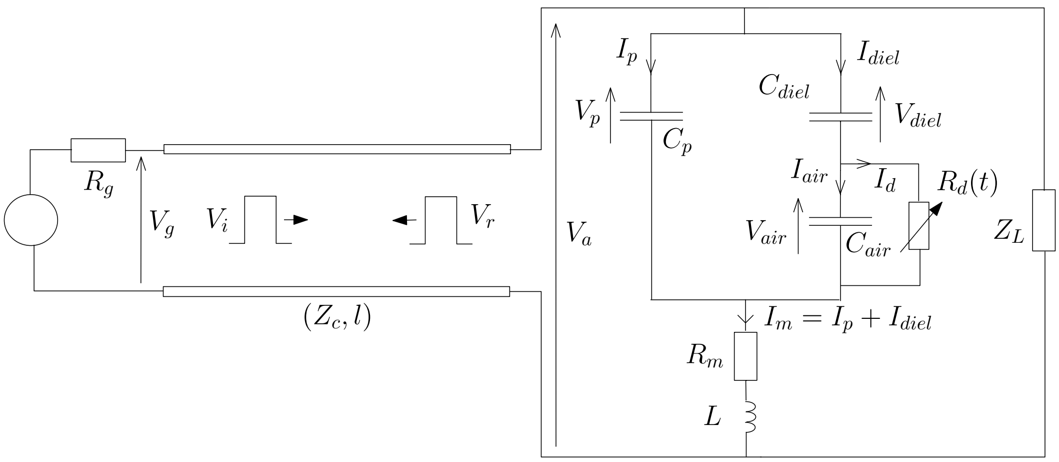

Figure I.12: Schematic illustrating the equivalent electrical circuit of exposure device.

I.4.1 Electronic circuit simulations

The current through the measure resistor I_m is the total current flowing the device, the discharge current is just one of its components. Whatever the experimental approach used to determine the discharge current from that measured, the accuracy will depend on the similarity in both currents. In other words, the more alike the currents, the more this determination will be accurate. In this section, we perform simulations to support the experimental approach. The modeling aims to contribute to characterizing the discharge current component in the total measured current. It also contributes to defining

experimental conditions suitable for the discharge current calculation.
Simulations are based on the transmission line model developed in Section I.3. The line is ended by the lumped elements depicted in Figure I.12. This equivalent circuit models the ns-DBD device or the ns-SDBD device, depending on the capacitance values. Numerical simulations are thus presented for different capacitances values consistent with both devices. The effect on electrical parameters, on discharge current especially, is discussed.

Results for a set of reference values

Conditions of simulations are similar to those of Section I.3: the coaxial cable length is 10 m and the voltage at the line input is the *ideal* pulse (see in Figure I.9). Table I.1 presents the electrical components values. They are chosen to be in a range of values consistent with the exposure devices. A set of reference values is in bold : C_{air} = 0.5 pF and C_{diel} = 40 pF, $C_{air} << C_{diel}$ by nature. The stray capacitance C_p = 0.1 pF is negligible. This set of reference values models a DBD device. The stray inductance is first neglected.

C_{air} (pF)	0.1	**0.5**	1	5
C_{diel} (pF)	5	10	20	**40**
C_p (pF)	**0.1**	1	10	20
R_d ($k\Omega$) $t > t_s$	-	0.25	**1**	5

Table I.1: Elements circuit values, reference values are in bold.

Figure I.13 shows the electrical parameters (voltages and currents) for the set of reference element values with and without discharge.
Without discharge, the circuit is a classical capacitive circuit. The voltage drop across the measure resistor R_m can be neglected. Voltages over the air gap and the dielectric layer follow

$$\begin{aligned} V_{air}(t) &\approx \frac{C_{diel}}{C_{air}+C_{diel}} V_a(t), \\ V_{diel}(t) &\approx \frac{C_{air}}{C_{air}+C_{diel}} V_a(t). \end{aligned} \quad \text{(I.5)}$$

As $C_{air} << C_{diel}$, the incident voltage pulse is mainly applied to the air gap : $V_{air}(t) \approx V_a(t)$ and V_{diel} negligible.
Currents are only displacement currents. The measured current is mainly due to C_{air} as

$$I_m(t) \approx \frac{C_{air}C_{diel}}{C_{air}+C_{diel}} \frac{dV_a(t)}{dt} + C_p \frac{dV_a(t)}{dt} \approx C_{air} \frac{dV_a(t)}{dt}. \quad \text{(I.6)}$$

The equivalent capacitance of the device is approximately $C_{air} + C_p$ = 0.6 pF, the reflection is then very weak.

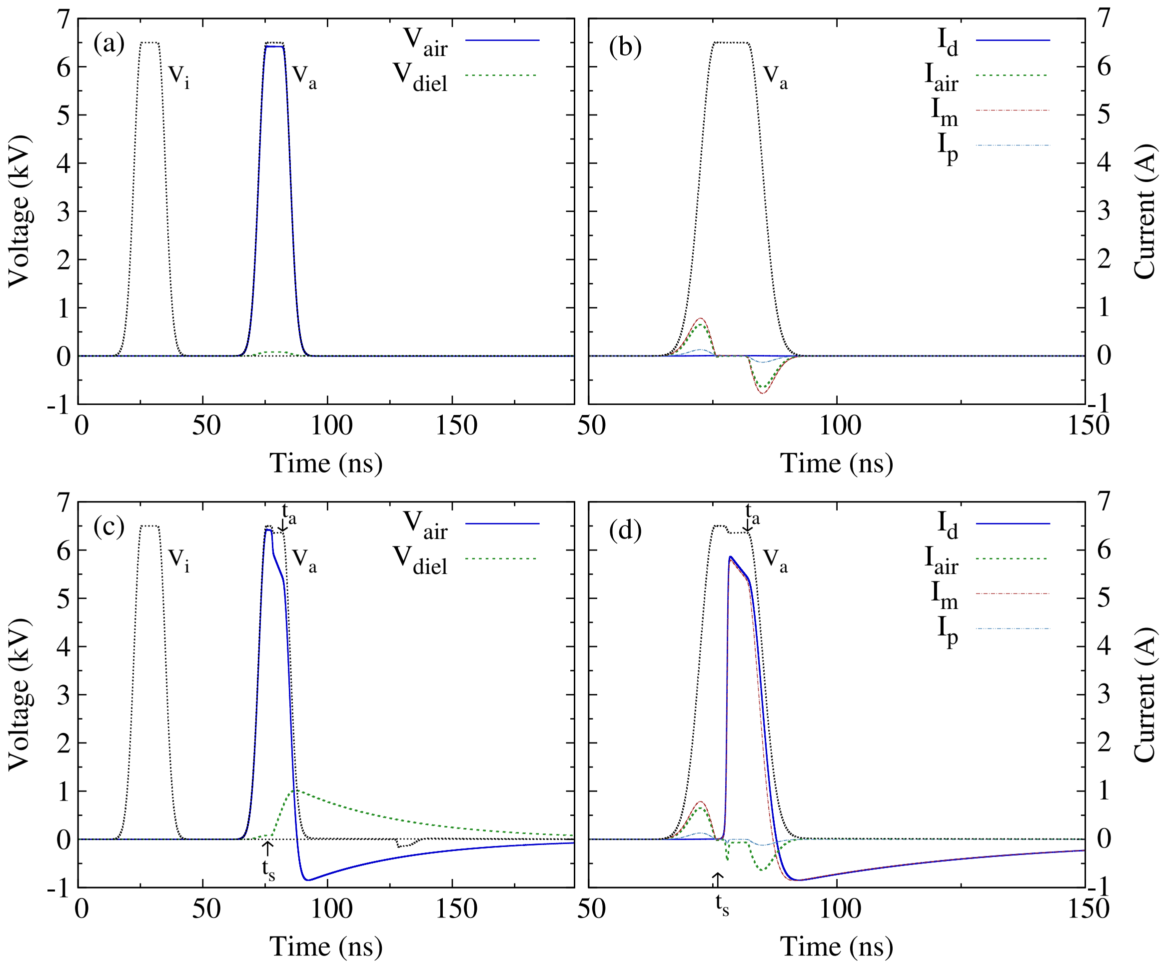

Figure I.13: Voltages and currents for the set of reference values for the circuit elements, for an *ideal* incident pulse V$_i$. t_s = 76 ns is the trigger of discharge and t_a = 82 ns is the time when the applied voltage begins to decrease. Results obtained without discharge (top figures) and with discharge (bottom figure). Applied voltage pulse V$_a$, voltages over the air gap V$_{air}$ and over the dielectric layer V$_{diel}$ (a) and (c). Discharge current I$_d$, current measured I$_m$ and currents in C$_p$ and C$_{air}$ (b) and (d).

The discharge is modeled by an interruptor and a resistor R$_d(t)$ in series (Kogelschatz, 2003). The resistance is a simplified model of the plasma channel. Note that the aim of the modeling is not to find an equivalent model of the discharge channel but to support the experimental approach. The resistance R$_d$ varies rapidly in time. The time of switch on is determined before the simulation. It is chosen at t_s = 76 ns, when the applied voltage is maximum and the capacitors are charged. Before switch on R$_d$ = 1 MΩ, the switching time is arbitrarily set to 2 ns, and then R$_d$ = 1 $k\Omega$. The rise time of discharge current depends on switching time, it is thus beyond the scope of discussion. The description of voltages and currents can be decomposed in 3 stages in time (see in Figure I.13 (c) and (d)) :

- *For $t < t_s$*, currents and voltages are identical to those without discharge.

- *For $t_s < t < t_a$*, with t_a the time when the applied voltage begins to decrease. As soon as the interruptor is switched on, C_{air} is in parallel with R_d. C_{air} starts to discharge through R_d. During this time R_d rapidly varies, V_{air} suddenly drops and I_{air} presents a negative minimum. Then C_{diel} begins to charge, V_{air} decreases while V_{diel} increases. The current I_{air} is then due to the discharge of C_{air}.
  The measured current I_m is very similar to the discharge current I_d. The maximum discharge current is about V_{air}/R_d. As the current I_{air} is negative, the discharge current is greater than the measured one ($I_m \approx I_{air} + I_d$, $I_p \approx 0$). These currents fall with a time constant approximate to $R_d C_{diel}$. Their maximum values only differ of about 1 %.

- *For $t \geq t_a$*. The measured current remains similar to the discharge current. The current flowing C_{air} is a displacement current. With the end of the applied voltage pulse, $V_{air} \approx -V_{diel}$ so the sign of V_{air} reverses. The amplitude of discharge current is then negative. This maximum mainly depends of the charge status of C_{diel} by I_d before the applied voltage ends.
  A discharge current is still flowing in R_d after the applied voltage pulse ending. This current is due to the discharge of C_{diel} through R_d. The surface charge on the dielectric (i.e. C_{diel}) can be driven in the discharge channel which is still modeled by a non infinite resistance ($R_d = 1 k\Omega$).

As discussed in Section I.3, the reflection is only due to the current flowing through the measure resistor following Equation I.4. So the discharge causes the reflected voltage pulses (see at 130 ns in Figure I.13(c)). Therefore, the applied voltage, that is the sum of incident and reflected pulses, drops.
It should be pointed out that the discharge current and measured current are very similar since the displacement currents are very weak. In that case one can easily obtain the discharge current from the measured one.

Parametric study

To further investigate the role of each circuit elements, we perform a parametric study with elements values considered in the Table I.1 :

- Figure I.14 shows results when C_{air} varies. The currents behavior is same to the one described in the reference conditions, except for case of high capacitance (5 pF). Maximum of discharge current is about V_{air}/R_d. The amplitude of V_{air} after switch depends on the charge status of capacitances C_{air} and C_{diel} before switch (see Equation I.5). When C_{air} increases (for a given C_{diel}) the maximum of discharge current reduces.

For C_{air} = 5 pF, the measured current is very different from the discharge current in shape and amplitude. Indeed the current I_{air}, that is a negative component in the measured current, is strengthened. After switch on, this component due to the discharge of C_{air} is no more negligible and the maximum of measured current is then lower. At pulse ending, the induced displacement current predominates and screens the component of discharge current in the measured one.

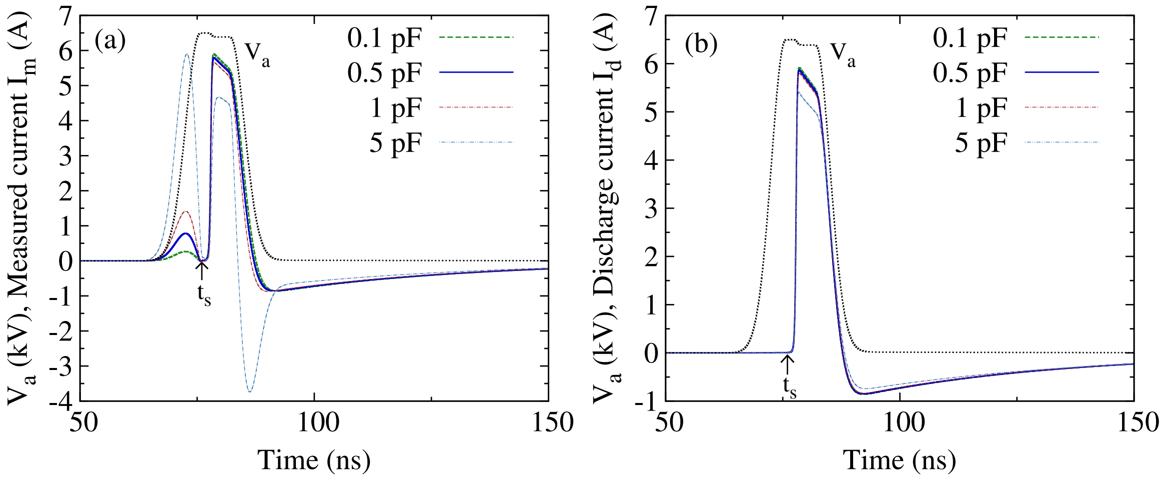

Figure I.14: Currents for C_{air} = 0.1 − 5 pF for an *ideal* incident pulse. t_s = 76 ns is the trigger of discharge and V_a is the applied voltage pulse for C_{air} = 5 pF. Results obtained for the reference values in solid line. Measured currents (a) and discharge currents (b).

- Figure I.15 shows that a decrease in C_{diel} changes the shape of both currents. The capacitance C_{diel} mainly drives the discharge current after its maximum. The time constant $R_d C_{diel}$ decreases with C_{diel}. This time constant governs the fall and the increase in current after both maxima (positive and negative). The current shape changes consequently. Moreover, the negative maximum in discharge current depends on the charge status of C_{diel} before pulse ends, following $V_{air} = -V_{diel}$.
  The maximum of discharge current decreases with C_{diel} as it depends on the values of V_{diel} and V_{air} before switch on (see Equation I.5). Enhancement of I_{air} leads to a distinction between maxima of measured and discharge currents. A difference of 10 % is observed for C_{diel} = 5 pF.

- Whatever the stray capacitance C_p, discharge current remains approximately unchanged while the measured current is significantly changed (see in Figure I.16). An increase in the C_p value leads to an increase in the displacement current component ($C_p dV_a/dt$ in Equation I.6). For high values (C_p > 10 pf in our conditions), displacement current component screens the component of discharge current in the measured current.
  A high stray capacitance value dominates the device impedance. For C_p = 20 pF

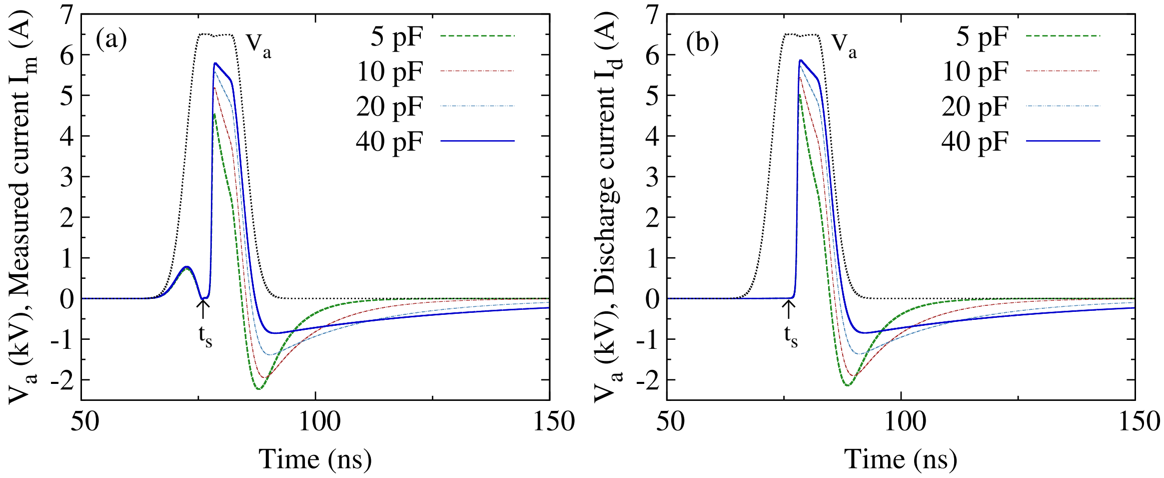

Figure I.15: Currents for $C_{diel} = 5 - 40$ pF for an *ideal* incident pulse. $t_s = 76$ ns is the trigger of discharge. V_a is the applied voltage pulse for $C_{diel} = 5$ pF. Results obtained for the reference values in solid line. Measured currents (a) and discharge currents (b).

Figure I.16(b) shows that the reflected pulses are the same to those presented in Figure I.10 for a same equivalent capacitance. This reflection superimposes to the one due to the discharge.

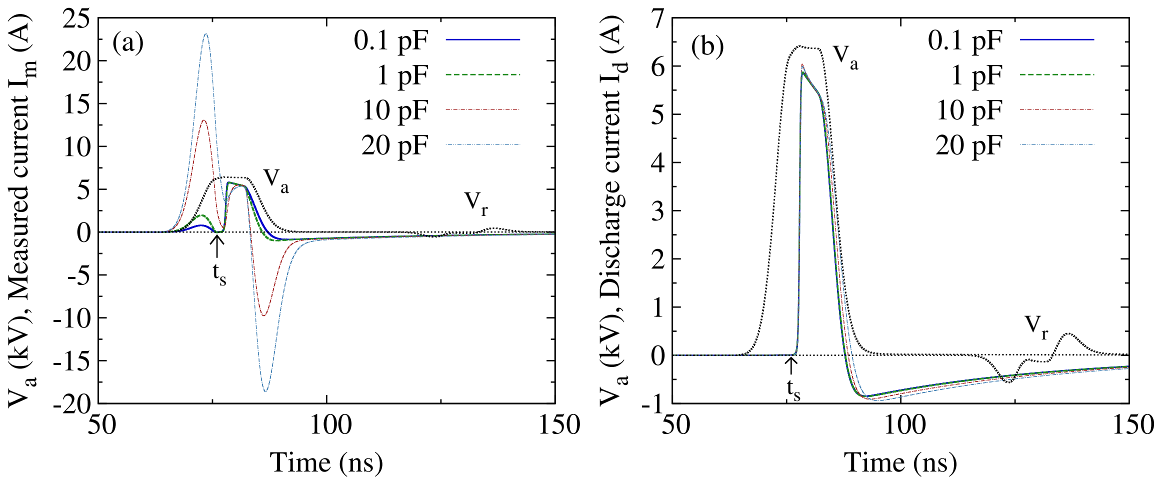

Figure I.16: Currents for $C_p = 0.1 - 20$ pF for an *ideal* incident pulse. $t_s = 76$ ns is the trigger of discharge. V_a is the applied voltage pulse and V_r the reflected pulses for C_p = 20 pF. Results obtained for the reference values in solid line. Measured currents (a) and discharge currents (b).

- Results depend on the modeling of variation in time of the resistor R_d that stands for a simplified model of discharge. We consider R_d as a circuit component. Figure I.17 compares results obtained when R_d varies (after switching). Discharge and measured currents are very similar. A decrease in R_d limits time constant of charge and discharge of C_{diel} through R_d as well as the maximum of discharge current (V_{air}/R_d). For a high value of R_d displacement current is no more negligible compared to the discharge current.

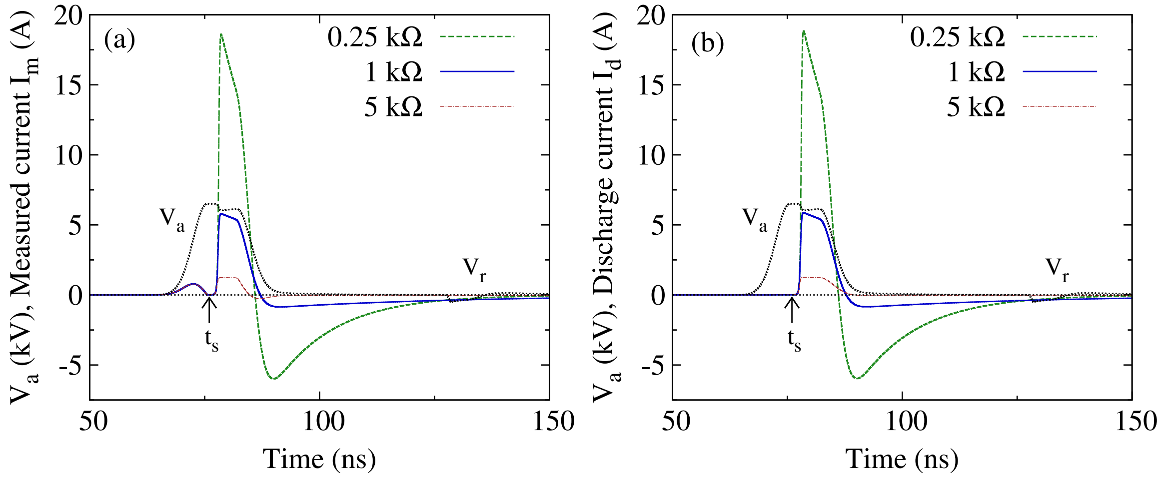

Figure I.17: Currents for $R_d = 0.25 - 5$ kΩ for an *ideal* incident pulse. $t_s = 76$ ns is the trigger of discharge. V_a is the applied voltage pulse and V_r the reflected pulses for R_d = 0.25 kΩ. Results obtained for the reference values in solid line. Measured currents (a) and discharge currents (b).

- The last case takes into account the self-inductance due to connexions. Figure I.18 compares the reference results and results obtained with L = 0.2 µH. Reflection caused by the discharge is increased. Oscillations occur in currents at a frequency of $(2\pi\sqrt{LC_{air}})^{-1}$ = 500 MHz. The stray inductance provides a realistic approach of connections effects at high frequency.

Conclusion

To summarize, the similarity between the discharge current and the measured one depends on capacitance values. When the stray capacitance is negligible, the equivalent circuit stands for a model of the ns-DBD device. In that case, both currents are very similar as long as C_{diel}/C_{air} >> 10. When C_{air} increases (for a given C_{diel} value) the associated current that is a negative component is strengthened. In a similar way, the associated displacement current screens the discharge current component in the measured current. The measured current is then very different from the discharge current in shape and amplitude. For a low C_{diel} value (for a given C_{air} value), the current flowing through C_{air} is strengthened. This leads to non negligible difference between maxima of discharge current and measured one.

When the stray capacitance impedance is preponderant, the circuit in Figure I.12 stands for an equivalent circuit of the ns-SDBD device. The displacement current component

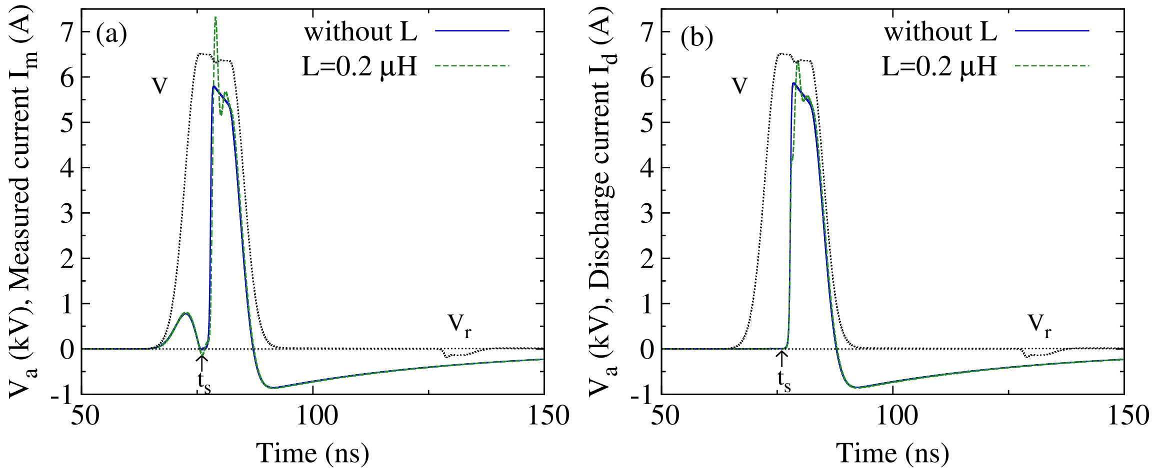

Figure I.18: Currents for an *ideal* incident pulse. t_s = 76 ns is the trigger of discharge. A stray inductance of L = 0.2 μH models connections. V_a is the applied voltage pulse and V_r the reflected pulses for L = 0.2 μH. Results obtained for the reference values in solid line. Measured currents (a) and discharge currents (b).

screens the component of discharge current in the measured one.

I.4.2 Electrical characterization

In experiments, the two waveforms available by measurements are :

- the total current flowing the exposure device given by using the measure resistor : $I_m = V_m/R_m$.
- The applied voltage V_a. The high voltage tap-off measures the incident and reflected pulses at the input of the exposure device (see in Figure I.1). The voltage actually applied to the exposure device is determined by using

$$V_a(t) = V_i(t - t_p) + V_r(t + t_p), \tag{I.7}$$

with t_p the wave propagation time that only depends on the length of cable between the tap-off and the exposure device.

We consider the equivalent circuit in Figure I.12 to calculate electrical parameters only based on the applied voltage $V_a(t)$ and the total current $I_m(t)$.

Let's define for convenience $V'_a = V_a - R_m I_m - L\dfrac{dI_m}{dt}$.

Applying the current Kirchhoff's law, the discharge current is given by

$$I_d = I_m - I_p - I_{air}, \tag{I.8}$$

with

$$I_p = C_p \frac{dV'_a}{dt}. \tag{I.9}$$

The applied voltage V'_a is the sum of the voltage across the air capacitance V_{air} and the voltage across the dielectric capacitance V_{diel}, hence

$$I_{air} = C_{air} \frac{dV'_a}{dt} - C_{air} \frac{dV_{diel}}{dt}. \tag{I.10}$$

By expressing the current through the dielectric capacitance

$$I_{diel} = C_{diel} \frac{dV_{diel}}{dt} = I_m - I_p, \tag{I.11}$$

and by using Equation I.10, one obtains

$$I_{air} = C_{air} \frac{dV'_a}{dt} - \frac{C_{air}}{C_{diel}}(I_m - I_p). \tag{I.12}$$

Finally Equation (I.8) becomes

$$I_d = (1 + \frac{C_{air}}{C_{diel}})I_m - (C_p + C_{air} + \frac{C_p C_{air}}{C_{diel}}) \frac{dV'_a}{dt}. \tag{I.13}$$

A complete electrical characterization of discharge can be achieved with the determination of the voltages across the gap air and the dielectric layer. By using Equations (I.12) and (I.9), the voltage across the air gap (per pulse) is expressed as

$$V_{air} = (1 + \frac{C_p}{C_{diel}})V'_a(t) - \frac{1}{C_{diel}} \int_0^t I_m(t)dt. \tag{I.14}$$

The voltage across the dielectric layer (per pulse) is given by

$$V_{diel} = \frac{1}{C_{diel}} \int_0^t I_m(t)dt - \frac{C_p}{C_{diel}} V'_a(t). \tag{I.15}$$

The expression I.13 gives the discharge current as a function of the waveforms I_m and V'_a. When considering $C_{air} << C_{diel}$

$$\begin{aligned} I_d &= I_m - C_p \frac{dV'_a}{dt} \quad \text{when} \quad C_p >> \frac{C_{air} C_{diel}}{C_{air} + C_{diel}} \\ I_d &= I_m - C_{air} \frac{dV'_a}{dt} \quad \text{when} \quad C_p << \frac{C_{air} C_{diel}}{C_{air} + C_{diel}} \end{aligned} \tag{I.16}$$

This leads to the common determination of the discharge current as the difference between the measured current and displacement current

$$I_d = I_m - I_{dis}. \tag{I.17}$$

Finally, the determination of the energy deposited into plasma is an important parameter for the biomedical applications. The determination of the energy also participates at the electrical characterization of the discharge. The energy deposited into plasma per pulse is defined as

$$E = \int_0^{\infty} V_{air}(t) I_d(t)\, dt, \tag{I.18}$$

where V_{air} is given by Equation I.14.

When the above electrical parameters can not be determined, the energy is commonly calculated from the measured waveforms I_m and V'_a

$$E = \int_0^{\infty} V'_a(t) I_m(t)\, dt = \int_0^{\infty} (V_a(t) I_m(t) - R_m I_m^2(t))\, dt \tag{I.19}$$

Finally, a classic problem in determination of energy arises from very small discharge currents. In that case, the voltage and current waveforms are nearly indistinguishable from the corresponding waveforms when no discharge is present. The energy is then calculated as

$$E_{\text{discharge}} = E_{\text{total}} - E_{\text{no discharge}} \tag{I.20}$$

Without discharge, no conduction current flows, and the energy $E_{\text{no discharge}}$ reflects parasitic losses.

I.4.3 Synchronization of voltage and current waveforms

The delay between the current and voltage waveforms has a strong influence on the determination of electrical parameters of discharges. We will determine the delay by using circuit simulations. We use the FDTD model. The sending voltage is the measured voltage for which the reflection is removed. We first compute the applied voltage and then we synchronize the waveforms considering the synchronization of numerical results.

Figure I.19(a) shows an exemple of applied voltage computed from incident and reflected experimental waveforms by using $V_a(t) = V_i(t - t_p) + V_r(t + t_p)$ (t_p is the wave propagation time). Before computation, the experimental data of voltage are filtered using one simple moving average filter (with 3 points) to reduce noise. The magnitude of the applied voltage is slightly larger than the incident pulse magnitude. A parasitic reflexion is found at the end of the fall time. To implement the calculation, we first computed the applied voltage from numerical results. Figure I.19(b) compares the applied voltage pulse directly obtained by simulation and that computed from numerical results. Both pulses superimpose which shows the accuracy of the applied voltage computation.

In simulation, results of current and voltage waveforms are synchronized. Therefore,

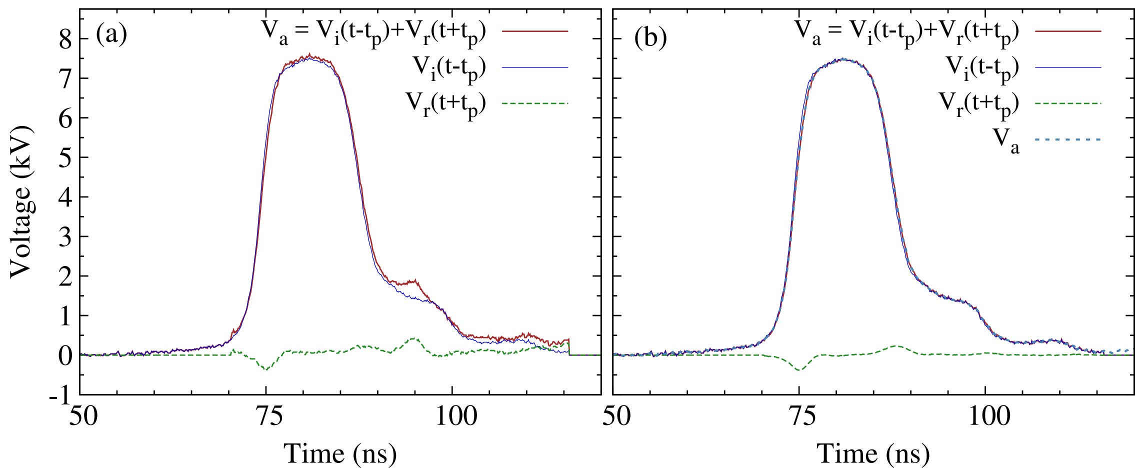

Figure I.19: Calculation of the applied voltage V_a from the experiments (a) and from the numerical results (b). t_p the wave propagation time.

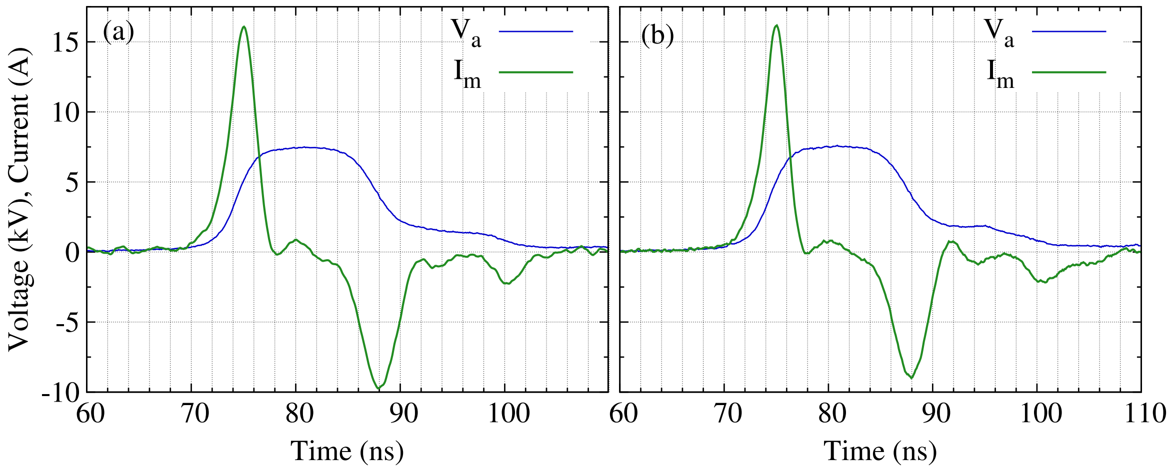

Figure I.20: Synchronization of applied voltage and current waveforms. Numerical results (a) and experiments (b).

the measured current is synchronized by matching the first pulse of displacement current to that of obtained in simulation. For example, in Figure I.20(b), the two curves were synchronized by shifting the measured current curve according to the numerical current showed in Figure I.20(a). This method provides a convenient way to synchronize the voltage and current waveforms, without and with discharge. The method uses the good accordance between displacement currents obtained in simulation and experiments.

The determination of the electrical parameters is thus based on the knowledge of the capacitances, which depend on the exposure device. Some of these values can be estimated using the classical expression

$$C = \frac{\epsilon_0 \epsilon_r S}{e} \tag{I.21}$$

where C is the capacitance of a capacitor made of two electrodes of surface S separated by a dielectric media of thickness e and relative permittivity ϵ_r. The above formula gives indicative values. Generally, we will adjust the capacitance values with respect to the displacement currents, by using circuit simulation in comparison with measurements. The capacitances determination will be detailed for each exposure device in their respective chapters.

I.5 Conclusion

This chapter aimed to present the experimental set-up that is common to both exposure plasma devices.

We first described the experimental set-up and the performance characteristics of its components. We detailed the measurement for voltage and current. The current is measured via a measure resistor in series with the discharge device. In experiments the measure resistance is the termination of a matched coaxial cable connected to the oscilloscope. It ensures a large frequency bandwidth required to measure nanosecond pulsed discharge current. The experimental set-up stands for a waveguide to apply and measure the voltage pulse, as well as to measure the current. In addition we provided a study on voltage pulses reflection. We developed a model of transmission line. Numerical results showed the efficiency of the circuit matching. Then we proposed an equivalent electrical circuit that stands to a suitable model for both ns-DBD and ns-SDBD devices. We presented numerical simulations to study the component of discharge current in the total measured one. A parametric study on capacitance values contributed to defining experimental conditions suitable for discharge current determination. The developed model will be used in the numerical treatment of experimental waveforms in the next chapters. Finally, we defined electrical parameters (voltages, currents and energy deposited per pulse) as a function of the measured waveforms, according to the equivalent circuit. We also described the method of waveforms synchronization to ensure an accurate delay determination.

Chapter II

Nanosecond-pulsed dielectric barrier discharge exposure device

Contents

II.1 Introduction

Dielectric barrier discharges can be realized in filamentary mode or in uniform mode. Filamentary DBDs are characterized by transient micro-discharges which result in inhomogeneous plasma treatment. An advantage of a uniform discharge in surface treatment applications is the uniform effect on the surface. The most common type of atmospheric air DBD is filamentary. It is known however that uniformity of DBD plasma could be improved by shortening the voltage rise time. On the phenomenological point of view, transition from filamentary to uniform regime can be explained using a simple time-scale analysis. Filaments develop as fast ionization waves. If the voltage rise time is shorter than the time needed to bridge the gap discharge develops under high over-voltage conditions. Uniformity is attributed to the high electric field in front of the ionization wave. The very high value of the field is responsible for the suppression of the instabilities by saturation of the ionization coefficient, the fast expansion of the plasma channels and their overlapping, the generation of UV radiation, and the generation of run-away electrons leading to pre-ionization of the gas (Ayan et al., 2009). Moreover results indicate that ns-DBD uniformity depends on applied electric field in the discharge gap (Liu et al., 2014). It is a threshold phenomenon. Uniform discharges are observed for fields applied to the air gap from 130 kV/cm to 185 kV/cm. The exposure device presented in this chapter is based on the work of Fridman et al. (Lin et al., 2015; Lin et al., 2017; Ranieri et al., 2017). The major difference is the magnitude of the applied voltage pulse that is lower here (29 kV in (Lin et al., 2017) and 10 kV in our study). The treatment distance is thus shorter in our work.

This chapter aims to present the experimental set-up and the electrical characterization of the ns-DBD. Section II.2.1 details the discharge exposure device that is integrated into the experimental set-up described in the Chapter I (Section I.2). In exposure conditions, the discharge develops in the air gap between the dielectric layer and the solution which is the counter electrode. We will discuss on the difficulty in electrically modeling the solution. Therefore in this chapter we will study the discharge generated between the dielectric layer and a metallic plane cathode, as a reference case. We will propose an equivalent circuit of the discharge device. The determination of the component values will be detailed. In Section II.3 we will electrically characterize the discharge. We first perform an experimental study on the discharge. Then we will determine the electrical parameters of the discharge according to the equivalent circuit. The discharge current, voltage across the air gap, voltage across the dielectric layer and energy deposited per pulse will be calculated. We will show that a Rompe-Weizel model, that is commonly used to model equivalent arc resistance, fits well with the ns-DBD electrical parameters. Finally, we will carry out a preliminary study on the discharge in the exposure conditions by using the biological solution as counter electrode.

II.2 Experimental set-up

II.2.1 Description

The ns-DBD exposure device is shown in Figure II.1. The pulse generating, measurements and monitoring are performed as described in Chapter I. For the performed experiments voltage pulses are delivered by the 10 kV generator. The exposure device in series with the measure resistor is inserted into the waveguide matched by the load impedance to ensure the propagation of the fast rising voltages pulses and to reduce reflection. The exposure device is connected to the supply coaxial cable with an HN connector, in parallel to the waveguide. This connexion length is minimized (around 5 cm) to reduce parasitic reflections.

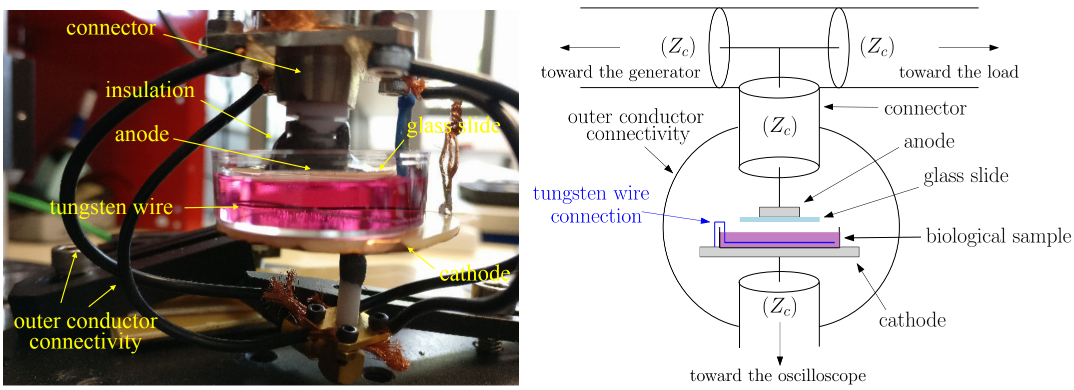

Figure II.1: Picture and schematic of the ns-DBD device with a Petri dish containing an aqueous solution (side view).

The discharge device is composed of :

- a high voltage electrode, the anode, connected to the inner conductor of the HV supply coaxial cable. The anode is made of a thin metallic film disk of 0.75 cm radius. The high voltage conductor is enclosed in a dielectric material for insulation.
- the anode is covered by disk glass slide as a dielectric barrier. The dielectric layer is 140 µm thick with a radius of 1.5 cm. The radius is greater than the radius of the HV electrode to assure a complete electrical insulation. We adapted device dimensions to expose biological sample contained in a standard Petri dish of 3.5 cm diameter.
- an air gap with the thickness varying using a micrometric positioning sliding plate. The reference gap distance is 350 µm.
- the cathode, which is made of a square copper plane of 5 cm side. This electrode is connected to the outer conductor of the set-up via the measure resistance. It should

be noted that a particular attention was paid at ensuring the continuity of the outer conductor. Four wires connected in parallel achieve this continuity ; the length of connection is then minimized.
The Petri dish containing the biological sample is placed on the copper plane. The Petri dish is filled with a constant volume of solution of 2 ml. The biological solution is a resistive conductor. It can act as the counter electrode, provided that it is electrically connected to the outer conductor. So a metallic wire immersed at a medium height connects the biological sample to the metallic copper plate. The wire is made of tungsten that is a non-oxidizable material and exhibits a low reactivity towards the biological sample. During plasma exposure, the discharge develops in the air gap, in between the biological sample surface and the dielectric layer on the upper side.

During plasma exposure, the surface of the biological solution acts as the counter electrode. The Petri dish, the solution height and the tungsten wire can induce, respectively, stray capacitances and stray inductance in the electrical circuit. Moreover, the biological solution as water-based substance medium is a dispersive medium. Such media present a complex frequency-dependent permittivity $\varepsilon(\omega)$ that account for their responses to electric field. A common dispersive model to approximate the frequency behavior of biological media permittivities is the Debye model

$$\varepsilon_r(\omega) = \varepsilon_\infty + \frac{\varepsilon_s - \varepsilon_\infty}{1 + i\omega\tau} + \frac{\sigma}{i\omega\varepsilon_0} = \varepsilon_\infty + \frac{\varepsilon_s - \varepsilon_\infty}{1 + (\omega\tau)^2} - i\left(\frac{\varepsilon_s - \varepsilon_\infty}{1 + (\omega\tau)^2}\omega\tau + \frac{\sigma}{\omega\varepsilon_0}\right), \quad \text{(II.1)}$$

where ε_s and ε_∞ are the relative permittivities of the medium in the limit of low frequencies and high frequencies, respectively. σ is the conductivity and τ is the dielectric relaxation time. An electrical conductivity of 1.5×10^{-2} S/cm and a relative permittivity of 76 were measured for the biological solution considered, at room temperature and in a frequency range up to few hundred of MHz (Kenaan et al., 2011). Figure II.2 illustrates the behavior of solution's relative permittivity as a function of the field's frequency. For low frequencies, the solution impedance is purely resistive due to the conductivity term. After 350 MHz, the dielectric component of the solution increases inducing a change in the solution impedance.

An electrical model of the counter electrode is thus not straightforward when considering the equivalent impedance of the solution, the Petri dish and the connection. Therefore we performed the study on the electrical characterization of discharges without Petri dish. The experimental set-up is same, the cathode is the metallic plane as shown in Figure II.3. Electrical measurements obtained in the case of the biological sample will be analyzed based on results obtained with the metallic plane.

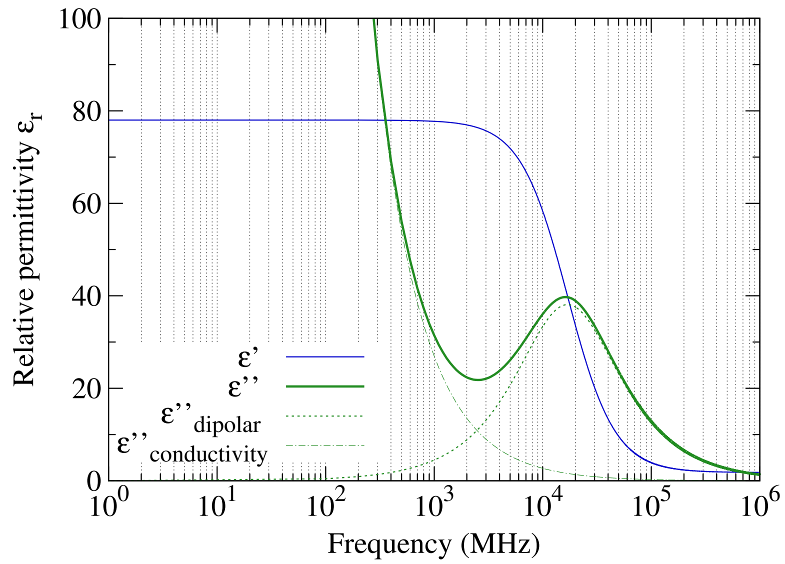

Figure II.2: Relative permittivity of water $\varepsilon_r = \varepsilon' - i\varepsilon''$ as a function of frequency of the electric field ($\varepsilon_s = 78$ and $\sigma = 1.5 \times 10^{-2}$ S/cm (Kenaan et al., 2011). $\varepsilon_\infty = 1.8$ and $\tau = 9.4 \times 10^{-12}$ s (values of water).

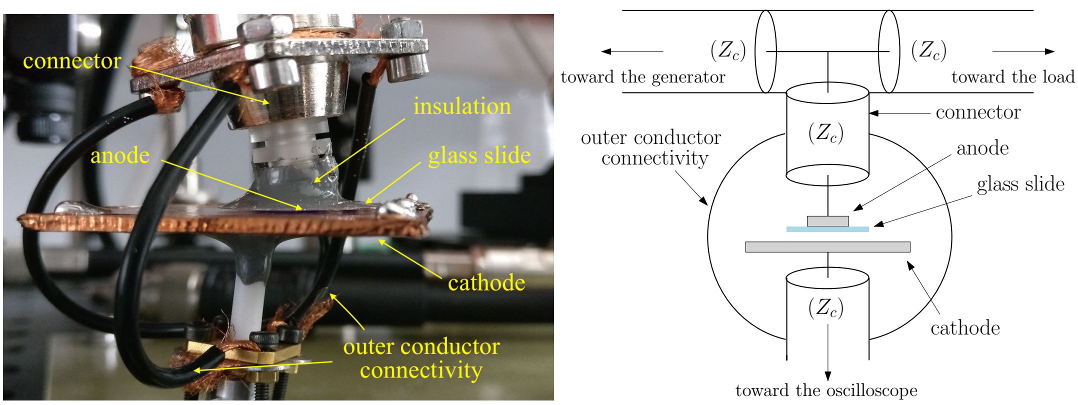

Figure II.3: Picture and schematic of the ns-DBD device (side view).

II.2.2 Frequency and time domain characterization

To determine frequency performance of the experimental set-up, we measured the S_{11} reflection coefficient. The real part and the imaginary part of the impedance are computed from the S_{11} parameter measurement. Results are given for both device configurations (the metallic plane and the biological solution). Figure II.4 shows a similar behavior in both cases till 300 MHz. The slight resonances observed in case of the experimental set-up with metallic plane do not affect its frequency bandwidth. When considering the biological solution, a resonance appears for each multiple of 175 MHz that leads to a mismatching beyond 300 MHz. This resonance is probably caused by the stray capacitances of the Petri dish containing the solution in series with the stray inductance due to connexion.

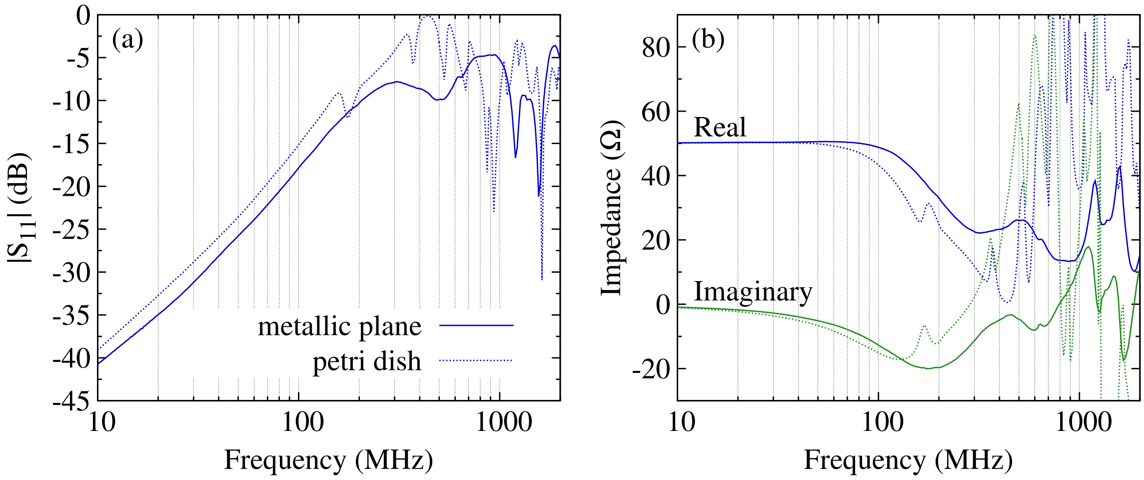

Figure II.4: Frequency domain measurements. Reflexion coefficient S_{11} (a) and impedance (b) of the ns-DBD device with the metallic plane (in straight line) and with the Petri dish containing the biological sample (in dotted line).

As illustrated Figure II.4(a), $|S11| < -7.5$dB for frequencies lower than 300 MHz for the set-up with the metallic plane. The latter value can be seen as an upper boundary defining the frequency bandwidth of the devices. When the counter electrode is the solution, the frequency bandwidth of the experimental set-up is then reduced to 210 MHz. A modification of its impedance reduces its bandwidth. Figure II.4(b) shows that for frequencies lower than 100 MHz the impedance of the set-up with the metallic plane is mainly resistive. As the frequency increases, the real part of the impedance progressively shifts from 50 Ω (22 Ω at 300 MHz), and the imaginary part increases. This is due to the equivalent capacitor of the discharge device. For the configuration with the biological solution, the equivalent capacitance of the discharge device is higher. The impedance mismatch is then stronger as it occurs for lower frequencies (around 50 MHz).

To complete the set-up characterization, Figure II.5 shows measurements of typical voltage and displacement current pulses obtained for the device with the cathode plane. The results are the raw measurement data, without numerical treatment or waveforms synchronization. The voltage is supplied by the 10 kV - generator to the ns-DBD device. The incident and reflected pulses are measured via the tap-off. The displacement current is measured via the measure resistor. The first current pulse rises in around 2.9 ns to 17.2 A. The incident pulse has a maximal magnitude of 7.56 kV, a full width at half magnitude (FWHM) of 13.6 ns and a rise time of 4.4 ns. The line is 5.18 m long between the tap-off and the discharge device, so the reflection is measured 51.8 ns after the incident pulse. This defines the propagation time $t_p = 25.9$ ns. The line length is sufficient to distinguish reflected and incident pulses. As discussed Section I.3.2, two pulses compose the reflection V_r. Their shape is not symmetric because of the incident pulse shape. A weak parasitic reflexion, probably due to the load impedance, adds 3 ns after V_r. Then, no voltage reflection is measurable. Less than 5 % of the incident pulse energy is reflected toward the generator. Results show the efficient matching of the device by the load impedance in the frequency bandwidth considered (up to 300 MHz).

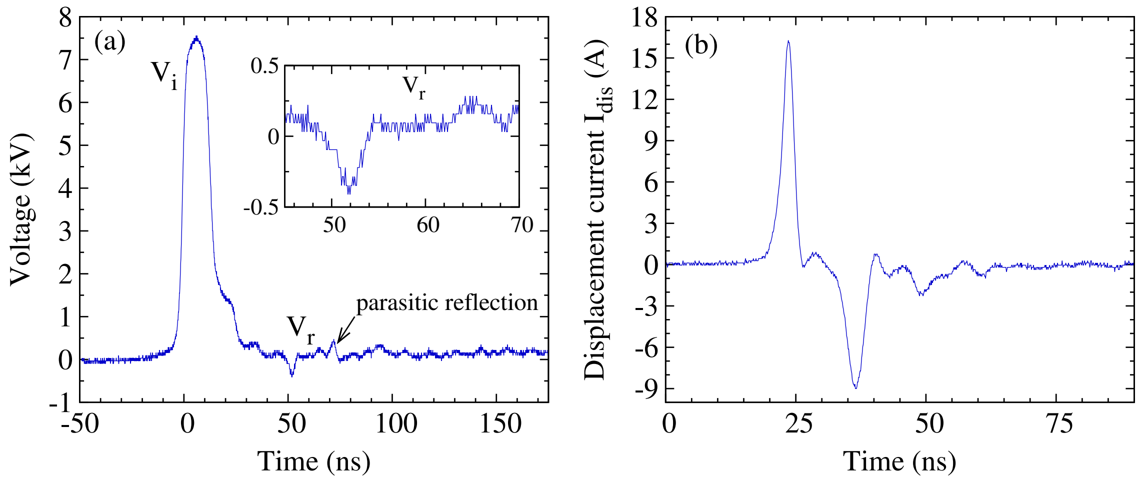

Figure II.5: Time domain measurements with the metallic plane. Incident and reflected pulses (a) and displacement current (b).

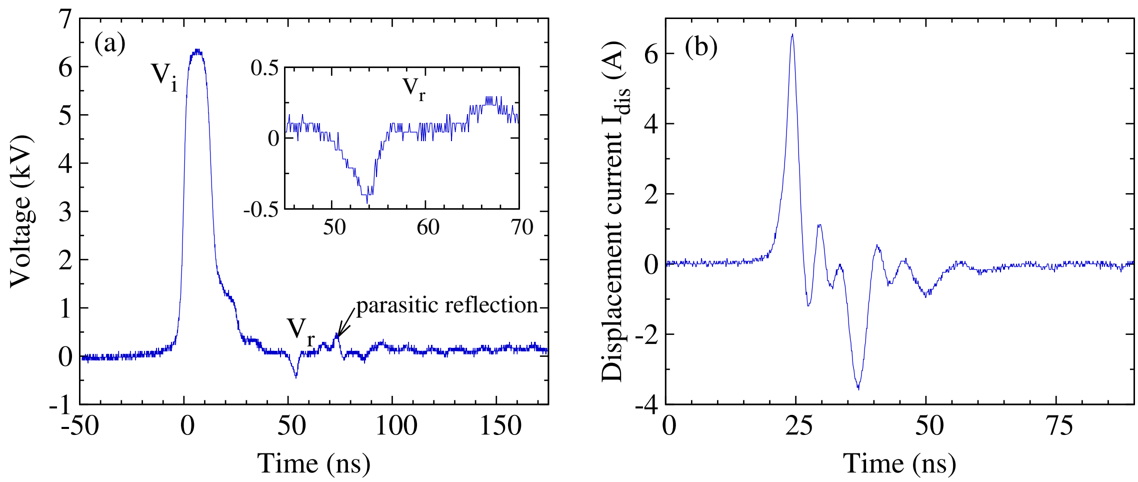

Figure II.6: Time domain measurements of the exposure device (with the Petri dish containing the biological sample). Incident and reflected pulses (a) and displacement current (b).

Figure II.6 shows the measurements obtained for the exposure device. The shape of displacement currents is similar to the waveforms obtained with a metallic cathode. One can observe oscillations in the displacement current. These oscillations correspond to the circuit resonance at 250 MHz (see in Figure II.4(b)).

II.2.3 Equivalent electrical circuit

To determine the electrical parameters of ns-DBDs, an equivalent model of the exposure device has to be assessed. Each element of the experimental device set-up is associated to an electrical component. In this way we arrive at the equivalent circuit of the ns-DBD device shown in Figure II.7, in which the cathode is the metallic plane. This equivalent circuit is the same as the one proposed in Figure I.12, the details are as follows :

- the impedance due to the matched load, $Z_L \equiv Z_c = 50\ \Omega$, at the device location.
- the equivalent capacitor of the dielectric barrier, C_{diel}.
  The dielectric layer is made of a 140 µm thick glass slide. The relative permittivity $\varepsilon_r = 7$. A first approximation of the capacitance can be given using $C = \varepsilon_0 \varepsilon_r S/e$. S is the anode surface of radius 0.75 cm. The capacitance C_{diel} is then estimated around 80 pF. Material and thickness of the dielectric layer were chosen to obtain a large value of C_{diel}, as discussed in Section I.4.1. This ensures to apply the voltage mainly to the air gap.
- the capacitance of the air gap, C_{air}.
  For a 350 µm gap distance, $C_{air} \approx 4.5$ pF by using the latter formula.
- the stray capacitance C_p that naturally exits in between the two electrodes.
  This capacitance can not be estimated using the latter formula, nor measured. Its value has to be estimated by using simulation.
- R_d that models the plasma resistance.
- the impedance due to the measure resistor, $R_m \equiv Z_c = 50\ \Omega$, at the device location.
- the stray inductance, L, due to wire connections. The large metallic plate (the cathode) in series with wires also induces stray inductance.
  As a first approximation, the stray inductance only due to outer conductor connectivity is around 25 nH for a 2.5 cm connection length.

The above values of lumped elements are indicative. These values should be adjusted by numerical simulations to model the exposure device.

II.2.4 Determination of circuit element values

We perform circuit simulations to validate the equivalent circuit of the ns-DBD device as well as to optimize the values of elements. We use the FDTD model presented in Section I.3.2. The electrical termination of the line is the proposed equivalent circuit of ns-DBD device. The line is 5.18 m long. The sending voltage is an experimental incident waveform, i.e. a measured voltage for which the reflection is removed.

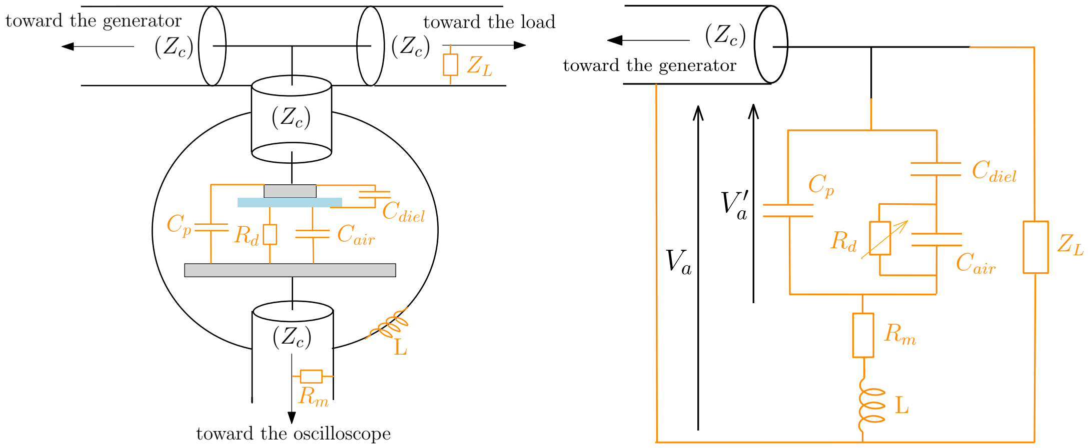

Figure II.7: Equivalent lumped elements of the exposure device/Equivalent circuit of the electrical termination.

Figure II.8 shows a set of numerical and experimental results of voltages and displacement current pulses. Experimental incident voltages have a magnitude of 5.8 kV and 7.56 kV. Numerical results are given for the set of optimized values presented in Table II.1. These values are determined by matching reflected pulses and displacement current to the experimental ones. A good agreement, in shape and magnitude, is obtained. The main difference is the magnitude of the second current pulse that is always over estimated by simulation. We focused on the accordance of the first current pulses.

C_{air} (pF)	C_{diel} (pF)	C_p (pF)	L (nH)
6.2	80	1.5	45

Table II.1: Elements circuit values for the ns-DBD device with the cathode metallic plane.

In addition to the circuit simulation, we calculated the equivalent impedance of the device for the set of given values. Figure II.9 compares theoretical and experimental results (also shown in Figure II.4). Results are in good agreement in the considered bandwidth frequency (up to 300 MHz). Beyond 450 MHz results behavior differs.

Finally, in the proposed equivalent circuit, the stray inductance is the only element that differs from classical electrical modeling of DBD at lower frequency. To analyse the role of this element, Figure II.10 compares the above results to results obtained without stray inductance. The capacitances are not changed. Shapes and magnitude of current pulses differ, in particular the first one, and the oscillations after the two pulses are not modeled. In the frequency domain, the equivalent impedances only agree at low frequency (up to 100 MHz). The stray inductance is of particular relevance to model the ns-DBD device up to 300 MHz.

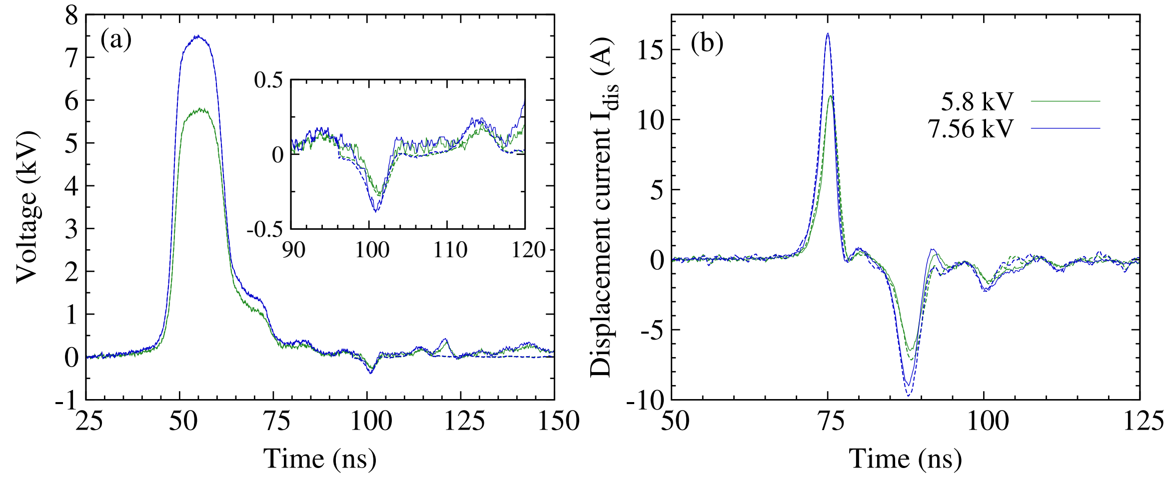

Figure II.8: Voltage pulses (a) and corresponding displacement current pulses (b). Measurements represented by a solid line and numerical results by a dotted line.

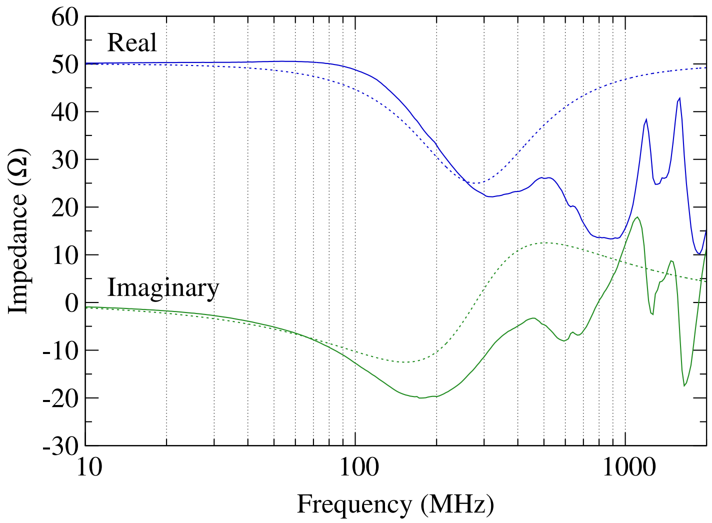

Figure II.9: Equivalent impedance of the device with the cathode metallic plane. Measurements represented by a solid line and numerical results by a dotted line.

To conclude, numerical results of voltage and displacement current pulses agree well with measurements for different voltage magnitudes. In the frequency domain, the equivalent impedance agrees well with experimental results in the considered bandwidth frequency. The good agreement validates the proposed equivalent circuit including the HF effect of connection via a stray inductance to model the ns-DBD device. This validation represents the first step in the determination of discharge electrical parameters. The values of elements (Table II.1) will be used in the following.

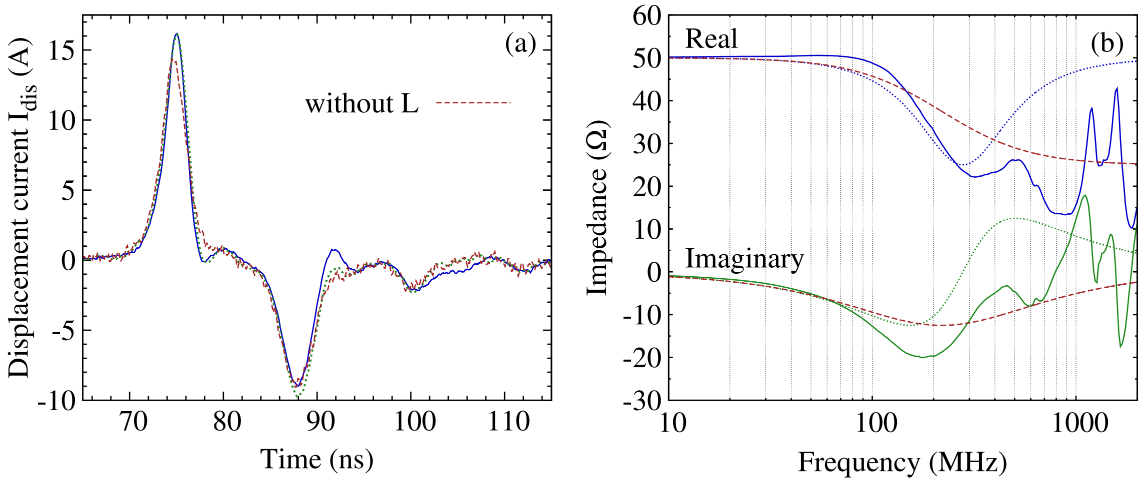

Figure II.10: Displacement current pulses (for a 7.58 kV voltage pulse) (a) and device impedance (b) without the stray inductance in the equivalent circuit. Measurements represented by a solid line and numerical results by a dotted line.

II.3 Electrical characterization of the discharge

We study the discharge with single-shot recorded. The discharge is not sensitive to the pulse repetition rate in the considered frequency range (up to 100 Hz). In Section II.3.1, we study the influence of electric field applied to the air gap by varying the applied voltage and the air gap distance. We first perform a statistical study on discharge time lag. Then we present the characteristics of the measured current pulses for a reference gap distance (350 µm). In Section II.3.2 we determine the electrical parameters of the discharge, as described in Section I.4.2. According to the equivalent electrical model, the discharge current, voltage across the air gap, voltage across the dielectric layer and energy deposited per pulse are calculated. In Section II.3.3 we show that a Rompe-Weizel model, that is commonly used to model equivalent arc resistance, fits with results computed from experiments. Finally, in Section II.3.4 we carry out a preliminary study on the influence of the Petri dish on the discharge.

II.3.1 Statistical study and current measurements

For the performed experiments the voltage pulses were delivered by the 10kV-generator. Pulses with different amplitudes were applied, from 4.67 kV to 10.45 kV. Their rise times are slightly dependent on the amplitude of the pulse, from 4.9 ns down to 4.4 ns. The FWHM is quite constant 13.8 – 13.9 ns. The air gap distances are 300 µm, 350 µm and 400 µm. We do not observe discharge for distances higher than $e = 400$ µm.

To characterize the ns-DBD, we first performed a statistical study of the discharge. It is commonly observed that the discharge breakdown is always preceded by a waiting period of time, namely the time lag to discharge ignition τ. This time lag is the sum of the statistical time lag τ_s and the formative time lag τ_f. The statistical time lag τ_s is the period of time between the instant of application of the electrical field and a sufficient generation of free electrons to lead to discharge ignition. The rate of production of free electrons naturally produced in the atmosphere is quite small, in the order of $10^3\ cm^{-3}\ s^{-1}$ (in normal circumstances). There is thus a small probability that free electrons are present in the gap during the voltage pulse. The most likely source of free electrons is secondary emission at the cathode surface. Once liberated, initiatory electrons start the multiplication avalanche leading to a discharge. This period of time is called the formative time-lag τ_f. It depends on the gas, the cathode material and the applied electrical field. In experiments the measured time lag is $\tau = \tau_s + \tau_f$. Note that a large number of initiatory electrons associated with a large over-voltage ensures a reliable discharge initiation whatever the discharge process considered.

Figure II.11 shows examples of results of the number of discharge occurrences as a function of the time lag. By convention, time $t = 0$ ns is defined as the time when the rising edge of the voltage pulse reaches 50% of its maximum value. The duration time of the voltage pulse is divided into regular periods of time. If a discharge occurs during the pulse rise the bar chart is colored in blue and in green if the period corresponds to the fall time. The probability density function is the skew-normal distribution with parameter α

$$\begin{aligned} f(x) &= 2\phi(x)\Phi(\alpha x), \\ \phi(x) &= \frac{1}{\sqrt{2\pi}} e^{-\frac{x^2}{2}}, \\ \Phi(x) = \int_{-\infty}^{x} \phi(t)\ dt &= \frac{1}{2}\left[1 + \text{erf}\left(\frac{x}{\sqrt{2}}\right)\right]. \end{aligned} \tag{II.2}$$

This distribution is a continuous probability distribution that generalizes the normal distribution for non-zero skewness. Indeed, statistical time lags are usually determined by using voltage pulses with fast rise time and long time duration. The duration of the pulse is here very short, around 13.8 ns. The skewness of the probability density function observed for the highest values of the time lags is due to the limited pulse duration. Therefore the selected statistical time lag τ at a given distance and incident voltage is taken as the mode of the arbitrary probability density function, not the mean. Table II.2 summarizes the results.

The time lag to discharge ignition increases as the incident voltage amplitude decreases for all gap distances. For $e = 300$ µm time lags are inferior to 3 ns. However the time lags less than 2 ns are associated with discharges occurring during the rise time of the voltage pulse (Figure II.11(a)). It is then difficult to conclude about a dependance on the maximum voltage. For the larger distances, distributions are similar. The time lags are

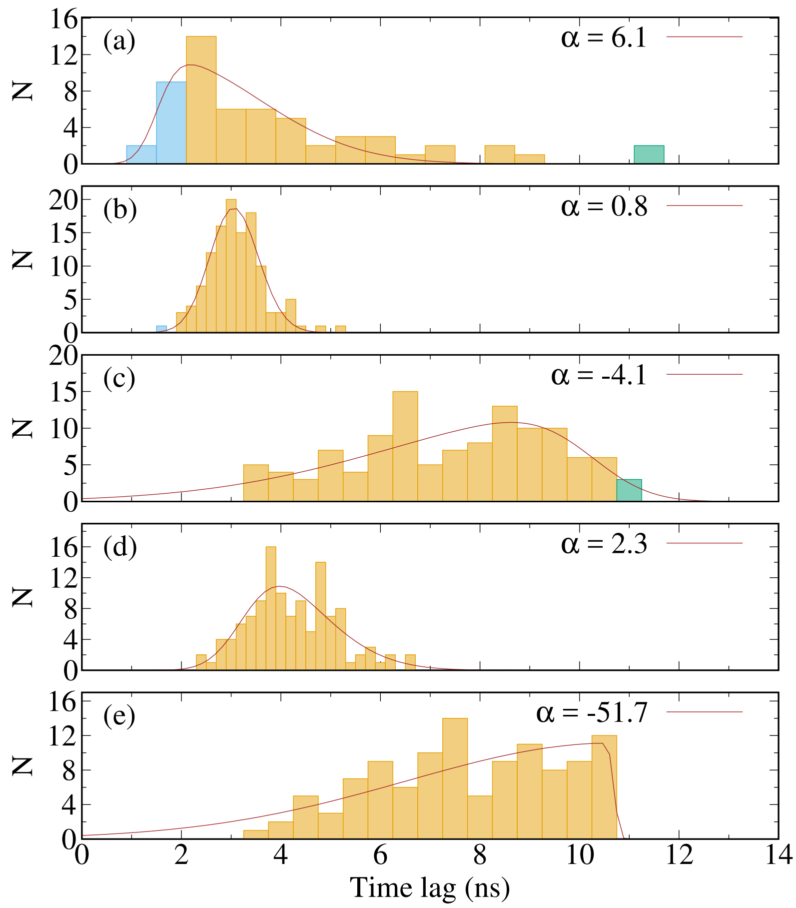

Figure II.11: Number of discharge occurrences N as a function of the time lag. $e = 300$ µm and V = 6.4 kV (a), $e = 350$ µm and V = 9.7 kV (b), $e = 350$ µm and V = 8.5 kV (c), $e = 400$ µm and V = 10.6 kV (d), $e = 400$ µm and V = 9.6 kV (e). α is the skewness factor determined by fitting.

close to 4 ns at high voltage (see in Figures II.11(b),(d)) and close to 9 ns at low voltage (see in Figure II.11(e)). In between, a transition appears in the time lag : the discharge time lag is randomly distributed over the duration of the voltage pulse between 4 ns and 10 ns, as shown in Figure II.11(c).

Figure II.12 shows the measured current for incident voltage pulses in the range 6.37 – 9.83 kV. The air gap distance is 350 µm. The lowest voltage is the inception voltage. To illustrate the time lag variation, the current pulses are synchronized on the displacement currents. The figure also shows an incident voltage shifted of $-t_p$. In between 8.5 and 9 kV, the measured current randomly distributed over the presented waveforms. The maximal amplitudes of the current gradually increases with the voltage amplitude, from 42.2 A to 76.8 A. Whatever the incident voltage amplitude, the shape of the measured current pulses is the same. The rise time of pulses is 600 ps. Currents exhibit a step in the tree-quarters of their rises. After reaching their maximum, the current pulses start to

$e = 300$ μm		$e = 350$ μm		$e = 400$ μm	
V (kV)	τ (ns)	V (kV)	τ (ns)	V (kV)	τ (ns)
8.5	1	9.8	4.1	10.6	4
7.7	1.2	9.7	3	10	8.5
7	1.2	9.4	3.9	9.1	10
6.4	2	9	4.1	9.6	11
5.7	2.5	8.9	8.7		
4.7	3	8.3	8.5		

Table II.2: Time lag as a function of the incident voltage pulse for the 3 considered air gap distances.

decrease, with a hump after the current peak. The current decreases up to the end of the voltage plateau. As the voltage pulse ends, the current falls up to reach a negative value. The FWHM of the current pulses then depends on the time lag. The duration is around 5.1 ns for short time lags and 6.5 ns otherwise. A current is still measured several tens of nanoseconds after the maximum current instant. The characteristics of the measured current are not sensitive to the applied field. The changes in the discharge time-lag can be explained by different electron emission processes at high field that reduce the statistical time lag.

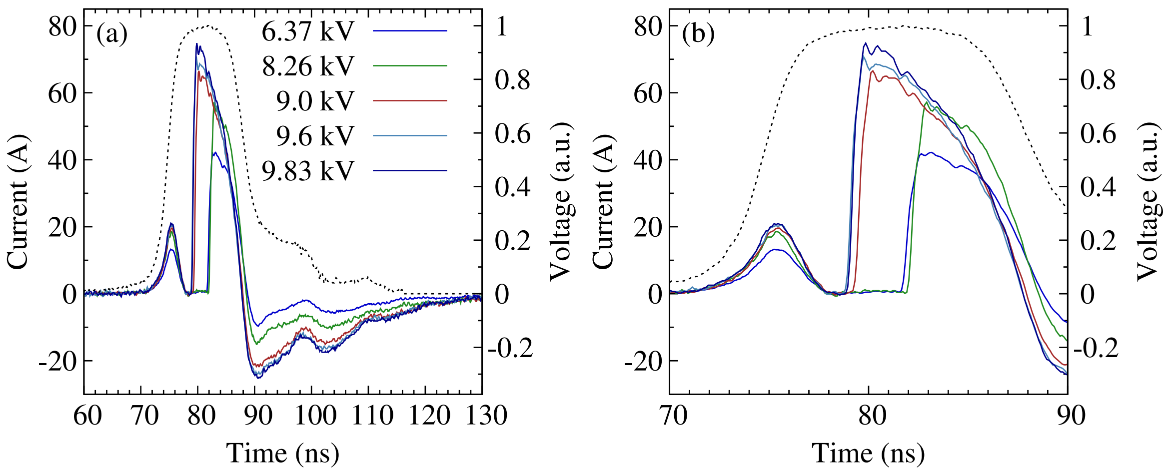

Figure II.12: Current pulses measured for incident voltage pulses of amplitude in the range 6.37 – 9.83 kV. The air gap distance is 350 μm.

Figure II.13 shows pictures of the discharge. It can be seen that discharge occupies the entire gap region. The luminosity appears to be diffuse. Note that the uniformity of the discharge cannot be discussed because of the long exposure time.

Figure II.13: Pictures of the ns-DBD. The exposure time is 4 seconds. The incident voltage amplitude is 10 kV for a 400 µm air gap distance, and the repetition rate frequency is 10 Hz.

II.3.2 Electrical parameters of the ns-DBD

In this section, we present one example of a typical result using the discharge electrical parameters.

Figures II.14(a),(b) show typical waveforms of voltage and current pulses measured. The results are the raw measurement data. The incident voltage pulse has a rise time of 4.4 ns, a maximum amplitude of 9 kV, and a FWHM of 13.6 ns. The applied voltage calculated from the incident and reflected pulses is shown in Figure II.14(c). The applied pulse rise is similar to the incident one. Then the applied voltage drops of 1.5 kV, because of the reflection due to the discharge. Parasitic reflections induce a plateau in the latter third of the pulse fall.

The measured current and the applied voltage are synchronized in Figure II.14(d). The synchronization was performed according to the method described in Section I.4.3. By convention, time $t = 0$ ns is defined as the beginning of voltage recording. The measured current is synchronized by matching the first pulse of displacement current to that of obtained in simulation. The two curves were synchronized by shifting the measured current curve by −24 ns, according to the numerical current. The experimental delay between the voltage and current pulses is thus 24 ns. The method uses the good accordance between displacement currents obtained in simulation and experiments (as shown in Figure II.8). The synchronization accuracy is thus estimated at ±0.1 ns for the 10 GS/s oscilloscope.

The current pulse starts to rise as the voltage has reached its maximum. The current pulse rises in 600 ps to a maximum of 66.5 A. In the same time the applied voltage drops. The current presents a step at the three-quarter of the pulse (see in Figure II.14(b)). Then the current pulse starts to decrease, with a hump after the current peak. As the voltage pulse ends, the current falls down to −21.5 A. The FWHM of the current pulse is 6.5 ns. Finally the current increases (up to 0 A) during 50 ns. A current is still measured after the applied voltage pulse ending.

In Section I.4.2 we defined the electrical parameters of the ns-DBD according to the equivalent circuit proposed in Figure II.7. The electrical parameters are then calculated from the measured current and the applied voltage. It should be noted that for the computa-

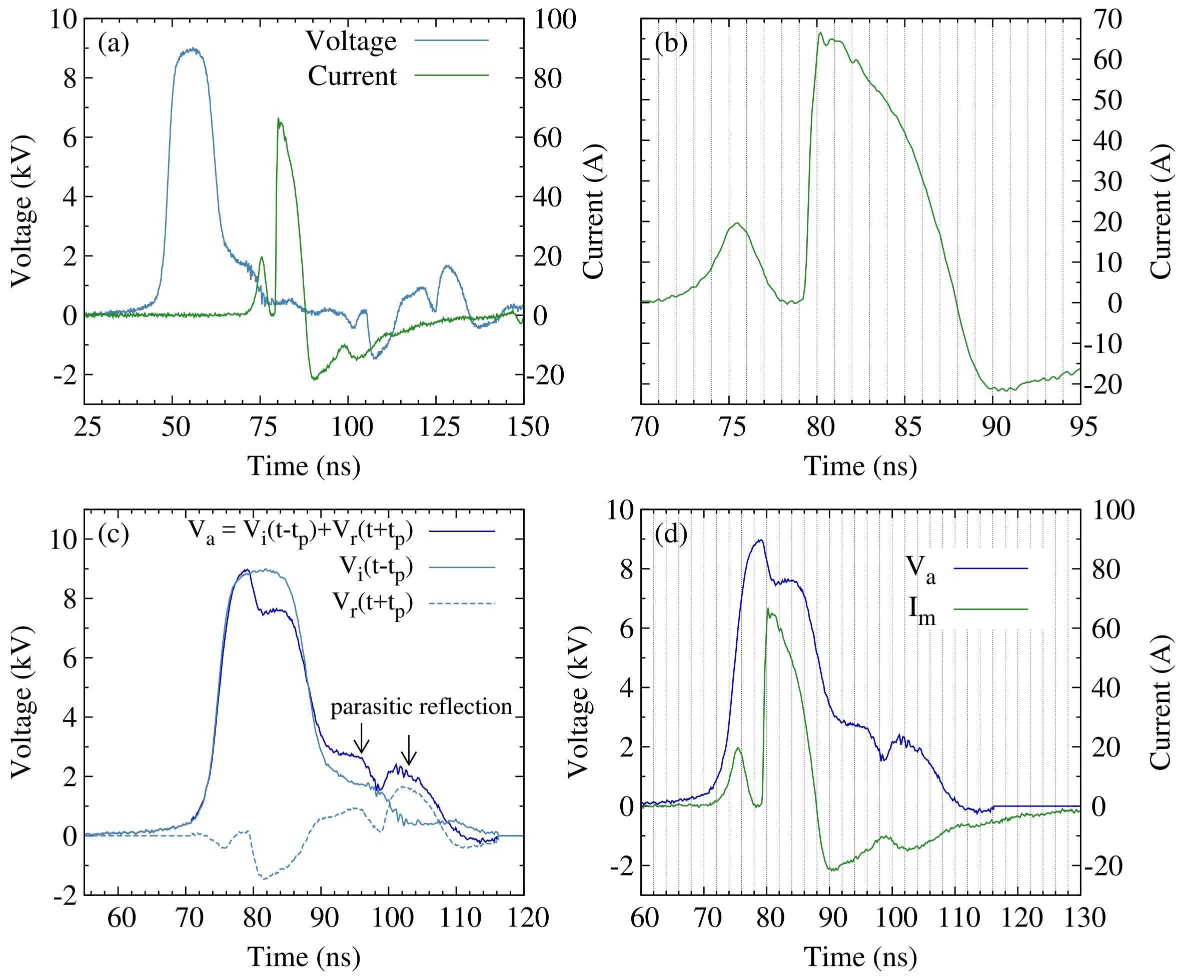

Figure II.14: Measurements with discharge. Incident and reflected voltage pulses and current pulse (a) and (b), calculation of the applied voltage V_a (c) and waveforms synchronization (d).

tion the experimental data of the current and the applied voltage were filtered using one simple moving average filter (with 5 points).

Figure II.15 shows the discharge current that is computed from Equation (I.13)

$$I_d = (1 + \frac{C_{air}}{C_{diel}})I_m - (C_p + C_{air} + \frac{C_p C_{air}}{C_{diel}})\frac{dV'_a}{dt},$$
$$V'_a = V_a - R_m I_m - L\frac{dI_m}{dt}$$

The oscillations in the discharge current are due to the circuit resonance between 1 and 2 GHz (see in Figure II.4). The rise of the discharge current pulse is very different from the measured one. The discharge current starts 0.6 ns before the measured current and exhibits a peak. The peak decreasing corresponds to the step in the leading edge of the measured current pulse. After the peak, the shape of both currents are similar, the discharge current amplitude (on average) is slightly larger than that of the measured one.

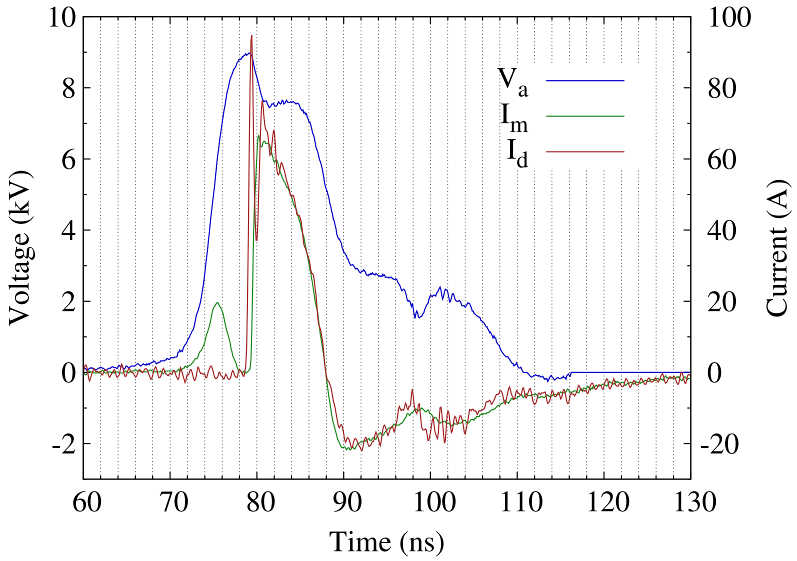

Figure II.15: Electrical parameters of ns-DBD. Applied voltage, measured current and discharge current computed from measurements.

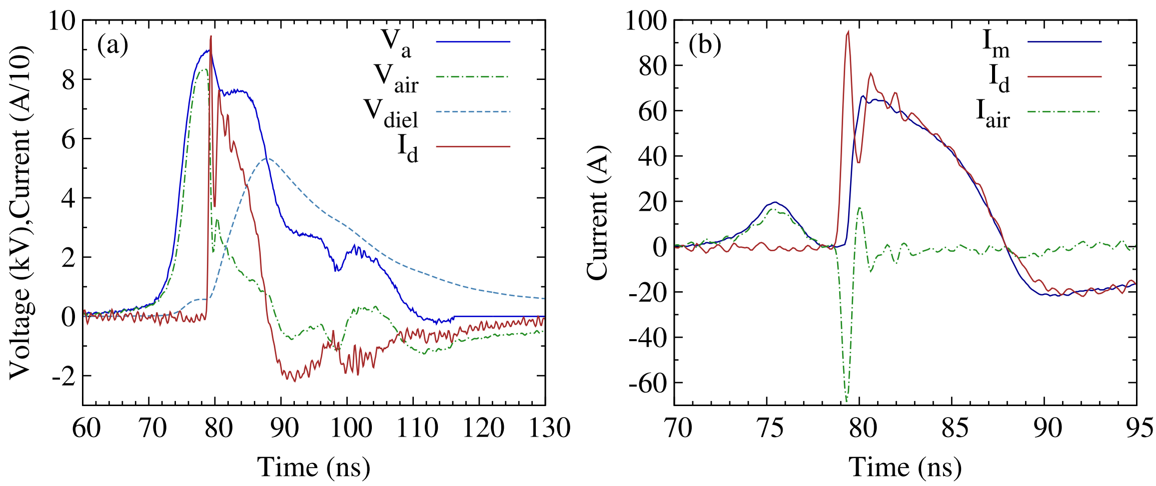

Figure II.16: Electrical parameters of ns-DBD. Applied voltage, voltages across the air gap and the dielectric layer and discharge current (a). Measured current, discharge current and current through the air capacitance (b).

The voltages across the air gap and the dielectric layer, and the current through the air capacitance are shown in Figure II.16(a). These parameters are computed from measurements using Equations (I.14) and (I.15) respectively. Figure II.16(b) presents the current through the air gap capacitance, I_{air}, computed with Equation (I.12). The measured current is the sum of the discharge current and the current flowing the air capacitance (when considering C_p as negligible).

As C_{diel} >> C_{air}, more than 90 % of the voltage is applied to the air gap. When the discharge ignites, C_{air} discharges in the discharge resistor. V_{air} suddenly drops of 75 % and I_{air} falls. The peak of the discharge current is thus the current due to the sudden discharge of C_{air}. The peak of the discharge current rises in 0.4 ns, for a maximum amplitude of 94.8 A and a FWHM of 0.7 ns. These characteristics depend on the numerical filter applied to the experimental data, even for a weak filtering. As well the discharge current calculation is based on numerical derivation (of applied voltage and measured current). Moreover the frequency bandwidth of the peak is around 1 GHz, which is out of the equivalent circuit bandwidth (300 MHz). Therefore, these values are only indicative.

As soon as the discharge is ignited, C_{air} is in parallel with the equivalent discharge resis-

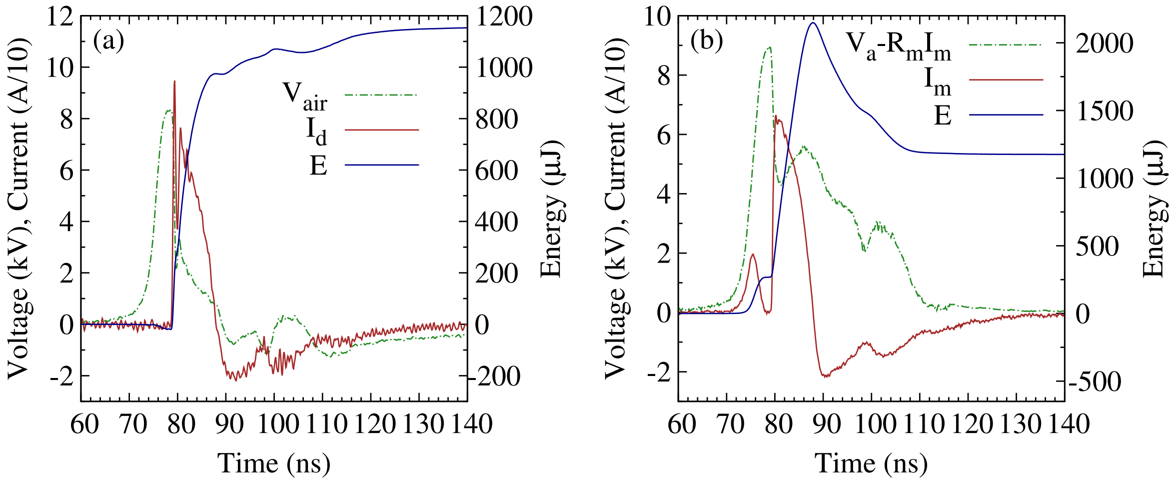

Figure II.17: Electrical parameters of ns-DBD. Energy deposited into the plasma per pulse. Result obtained by using Equation (I.18) (a) and Equation (I.19) (b).

tance that is of very low value. The discharge current charges C_{diel} and V_{diel} increases. V_{air} thus decreases, following $V_{air} \approx V_a - V_{diel}$, so the discharge current decreases. When the applied voltage starts to fall, V_{air} and thus the discharge current falls. C_{diel} keeps charging until the discharge current reaches 0A, 9.4 ns after the discharge ignition. At this instant the charge deposited on the dielectric layer is maximum, q_{max} = 15 mC. The corresponding surface charge density is σ = 8.5 mC/cm^2 when considering a uniform discharge (the discharge occupies a cylindrical volume of section equal to the anode surface). The density of surface charge is large, the sign of electric field applied to the gap thus reverses. The discharge current then becomes negative. A discharge current is still flowing in the plasma resistor after the applied voltage pulse ending. Indeed a voltage is still applied to the air gap as long as C_{diel} discharges. This capacitance discharges in the measure resistance. As well, the surface charge driven in a remaining plasma channel can contribute to the discharge of C_{diel}, on the considered time scale.

To complete the electrical characterization of the ns-DBD, the energy as a function of time is shown in Figure II.17(a). The instantaneous power applied to the plasma is obtained by multiplying the voltage applied to the air gap and the discharge current waveforms. The power waveform is then integrated in time over the total current duration to yield the energy deposited by the pulse into the plasma. The energy rapidly increases during the current pulse duration (i.e., the FWHM). From that moment on the energy slowly increases until the current reaches 0 A. The energy due to the discharge current peak is around 290 µJ. When considering that the peak amplitude is estimated at ±50 % and the final energy at 1.15 ±0.15 mJ.
Figure II.17(b) compares the energy deposited par pulse computed from the measured waveforms V_a and I_m (Equation I.19). In that case, the variation of the energy over the time is not described but the total energy is close to the reference one, around 1.17 mJ.

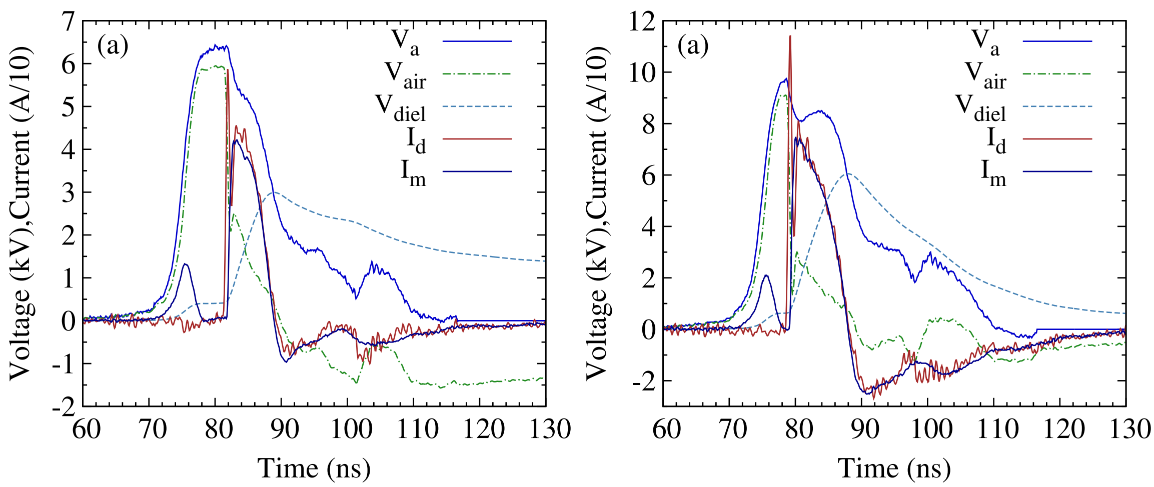

Figure II.18: Electrical parameters of ns-DBD. Applied voltage, voltages across the air gap and the dielectric layer, discharge current and measured current for a 6.37 kV - voltage pulse (a) and for a 9.83 kV - voltage pulse (b).

The above electrical parameters were calculated for discharges obtained when applying voltages of 6.37 kV (i.e. the inception voltage) and 9.83 kV. Results are shown in Figures II.18 and II.19. The applied electric fields to the air gap are 170 kV/cm and 260 kV/cm, respectively. Except for the characteristics depending on the applied voltage amplitude (magnitudes and time lags), the behavior of the electrical parameters is identical to the reference case. The main difference between results is the constant time in the decreasing phase of the voltage across the dielectric layer. This time constant decreases with an increase in the applied voltage. C_{diel} not only discharges in the 50 Ω measure resistance, but also in the equivalent resistance of a remaining plasma channel. This equivalent resistance decreases with an increase in the applied voltage. The energy deposited into plasma

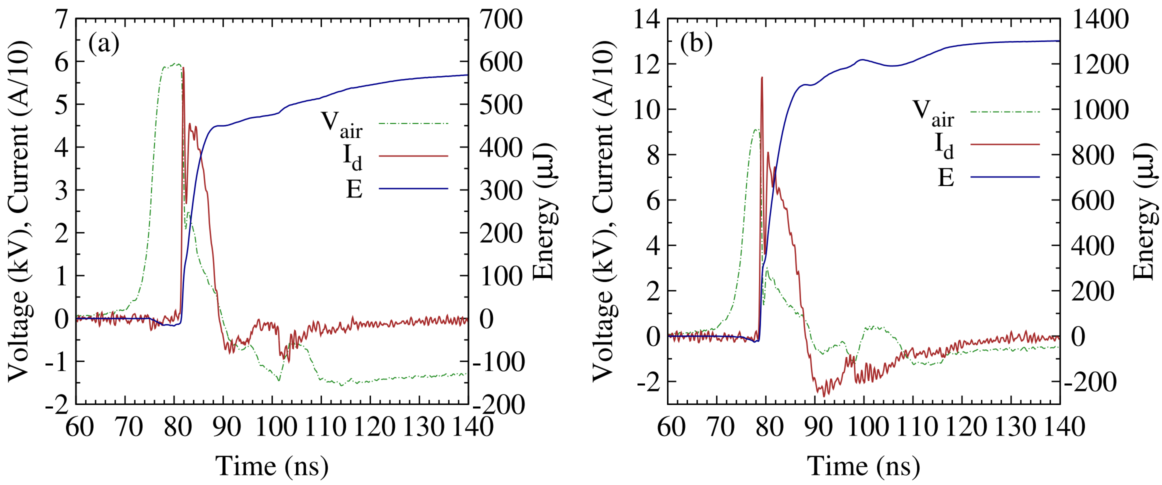

Figure II.19: Electrical parameters of ns-DBD. Energy deposited into the plasma per pulse for a 6.37 kV - voltage pulse (a) and for a 9.83 kV - voltage pulse (b).

per pulse is around 0.58 ± 0.07 mJ and 1.3 ± 0.16 mJ, respectively.

The behavior of electrical parameters (discharge current, voltages across the air gap and the dielectric layer, and energy) are not sensitive to field applied to the air gap in the considered range (170 – 260 kV/cm). Based on the similarity in results, we can consider that a same discharge regime is obtained in the considered conditions. According to (Liu et al., 2014) the ns-DBD obtained in similar conditions is uniform for field applied to the gap in the range 140 – 190 kV/cm.

II.3.3 Circuit simulations with a Rompe-Weizel model

The above results of the ns-DBD electrical parameters are similar to the numerical results obtained in Section I.4.1. The main difference is the peak in the discharge current. The numerical results were obtained using a very simplified model of discharge. The discharge was modeled by an interruptor and a resistor $R_d(t)$ in series. The value and the variation in time of the resistance were arbitrarily chosen. To further investigate the electrical behavior of the discharge, we perform here similar circuit simulations using a Rompe-Weizel model to model the discharge. The line is ending by the given equivalent circuit with elements values of Table II.1 and the sending voltage is the experimental incident voltage.
The Rompe-Weizel model is a current controlled resistance to model arc developing in air between metallic electrodes. The resistance is calculated at each time step but only the ignition time is chosen. (Jobava et al., 2000) found that a Rompe-Weizel model can model the arc resistance of electrostatic discharges. If a voltage pulse of 5 kV is applied to

an inter-electrode system of 323 µm spacing, the measured current pulse is characterized by an amplitude of 75 A, a rise time of 136 ps and a duration of around 5 ns. The pulse shape is very similar to the one obtained in our study. Therefore we propose a Rompe-Weizel model to take into account the discharge in electrical circuit simulations. The arc resistance as a function of time is given by:

$$\mathrm{R}_d(t) = \frac{2e}{\sqrt{2a_\mathrm{R}\int_0^t \mathrm{I}_d^2(t')dt'}} + \mathrm{R}, \qquad \text{(II.3)}$$

where $2e$ is the length of the discharge and its image, $\mathrm{I}_d(t)$ is the discharge current and a_R a parameter derived from basic ionization processes. The Rompe-Weizel model implies a constant electric field along the discharge channel. The model is here completed by adding a resistance R in series to model a DBD.

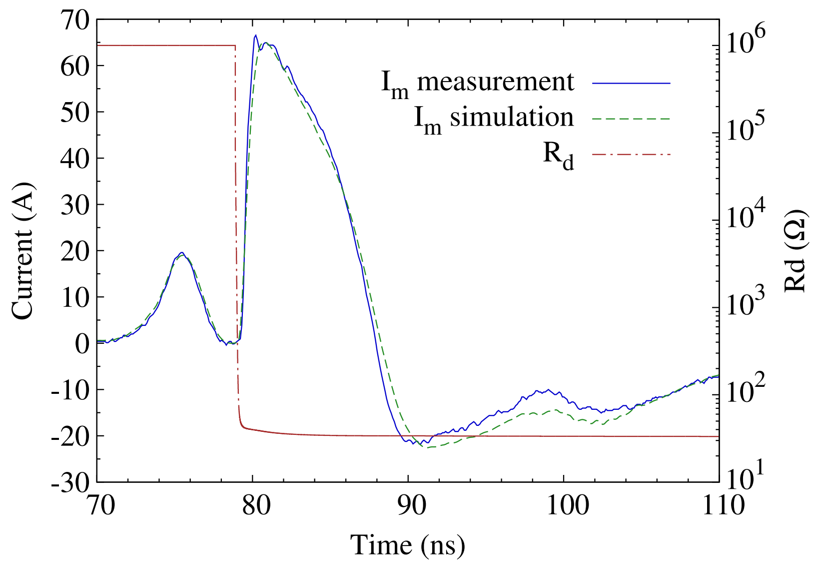

Figure II.20: Measured current obtained in experiments (solid line), in simulations (dotted line) and the discharge resistance modeled by the Rompe-Weizel model.

Figure II.20 shows the discharge resistance, the experimental measured current and the calculated current obtained by simulation. We choose the ignition time of discharge compared to the experimental result. The measured current significantly increases after a time delay which is a function of the a_R parameter. The pulse characteristics depend on a_R and R. In our conditions, $a_\mathrm{R} = 3 \times 10^{-4}\ \mathrm{m}^2/\mathrm{V}^2\mathrm{s}$ and $\mathrm{R} = 28\ \Omega$ give a good agreement with experiments. Figure II.21 compares the electrical parameters of discharge obtained in simulation to those computed from experiments. These results are in accordance. The shape of the discharge current is similar including the peak. The rapid variation in time of R_d (in less than 1 ns) driven by the Rompe-Weizel model gives satisfactory results to model electrical parameters of the ns-DBD. The main difference between results appears during the last stage. The decrease in the voltage across the dielectric layer is a little quicker with the Rompe-Weizel model. Nevertheless we can estimate the equivalent resistance of the remaining plasma channel at around 32 Ω.

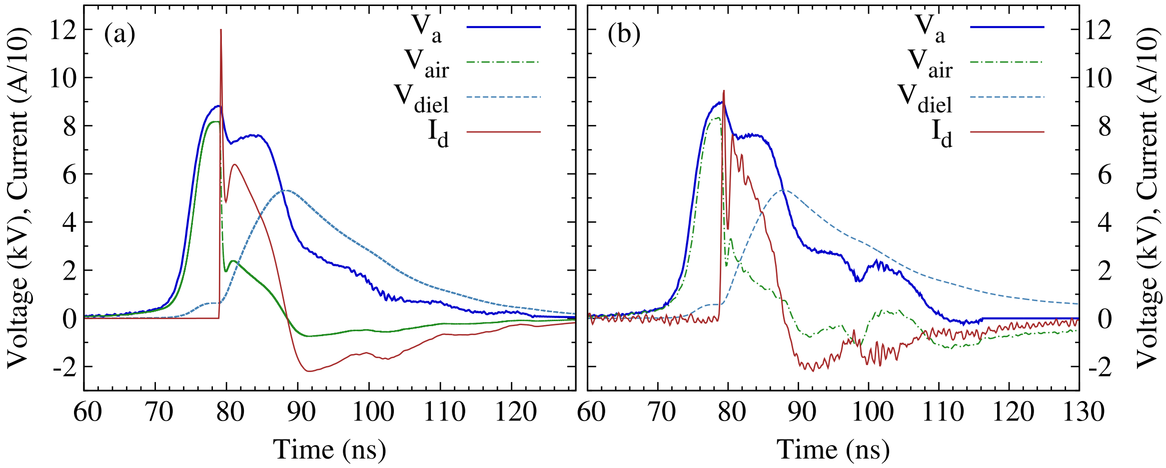

Figure II.21: Electrical parameters of discharge. Circuit simulations (a) and results obtained from experiments (b).

It should be noted that results obtained with the Rompe-Weizel model are in accordance with experiments for the considered range of applied voltages, namely 6.37 – 9.8 kV (results not shown). This is especially the case for voltages superior to 8 kV. R was in the range 30 – 22 Ω. In all cases, $a_R = 3 \times 10^{-4}\ m^2/V^2s$ which is in accordance with (Jobava et al., 2000) for a similar applied field range.

II.3.4 Influence of the exposure conditions

In the previous sections, we established the electrical characterization of the ns-DBD discharge with a cathode - metallic plane. The purpose of this section is to study the influence of the Petri dish in the exposure conditions. The experimental set-up is the same. The biological solution is the counter electrode as presented in Section II.2.1.

We first performed a statistical study of the discharge time lag. For the experiments voltage pulses are delivered by the 10 kV generator. Under these conditions, discharges occur for gap distances from 650 µm to 1.5 mm. For shorter distances, a wave on the solution forms and brings the dielectric layer in contact with the solution. The visual aspect of the discharge is similar to that presented in Figure II.13 by using a metallic cathode.
We present the results obtained with the 650 µm gap distance. Discharges occur for a voltage amplitude around 8 kV. Figure II.22 shows the number of discharge occurences as a function of the time lag. The time lag decreases in an uniform way from 8 ns to 5 ns with an incremental increase in the voltage. We did not observe a transition in discharge

time-lags as for the case of the metallic cathode. The secondary emission at the cathode surface, that depends on the cathode material, governs the discharge initiation.

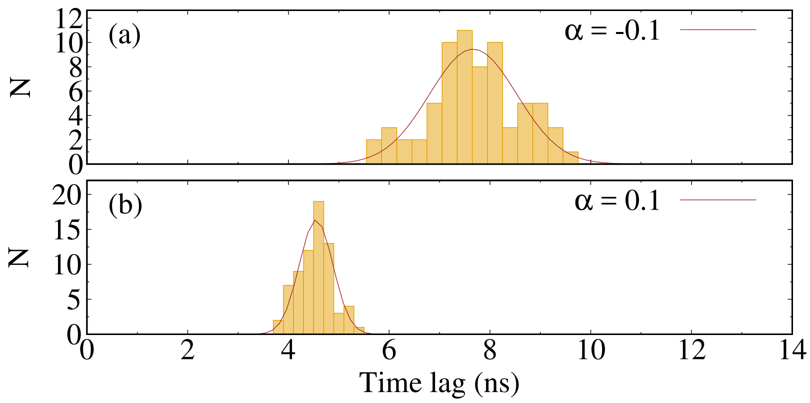

Figure II.22: Number of discharge occurrences N as a function of the time lag. The air gap distance is 650 μm. V = 8.9 kV (a) and V = 10.1 kV (b).

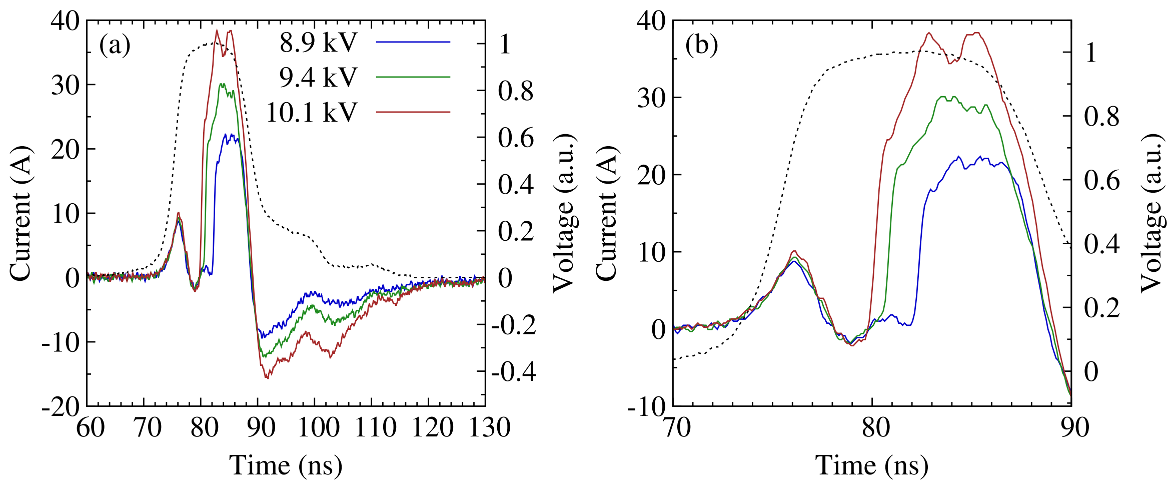

Figure II.23: Current pulses measured for incident voltage pulses of amplitude in the range 8.9 – 10.1 kV.

Figure II.23 shows the measured current for three amplitudes of incident voltage pulses, namely 8.9 kV, 9.4 kV and 10.1 kV. The current pulses are synchronized on the displacement currents to illustrate the time lag. An incident voltage which is shifted of $-t_p$ is also showed. The maximal amplitudes of the measured current are 22.4 A, 30.1 A and 38.4 A respectively. The amplitude has almost doubled for an increase in the incident voltage of only 1.2 kV. The shape of the measured current pulses is similar whatever the incident voltage amplitude. Current waveforms exhibit a step in the leading edge of the pulse (in the tree-quarters of their rises). The rise time up to the step is 0.6 ns, that is similar to the rise time measured with a metallic plane. After rising the current waveform forms a plateau. For the highest voltage, the plateau is formed of two successive maxima. As the voltage pulse ends, the current falls down to reach a negative value. The FWHM of the current pulses then depends on the time lag. The duration is around 5.7 ns for short time lags and 8 ns otherwise. A current is still measured several tens of nanoseconds after the maximum current instant.The rise and fall characteristics of the pulse are similar to those observed with the metallic cathode. The step in the leading edge of the pulse is more pronounced. The main difference is the plateau at maximum amplitude.

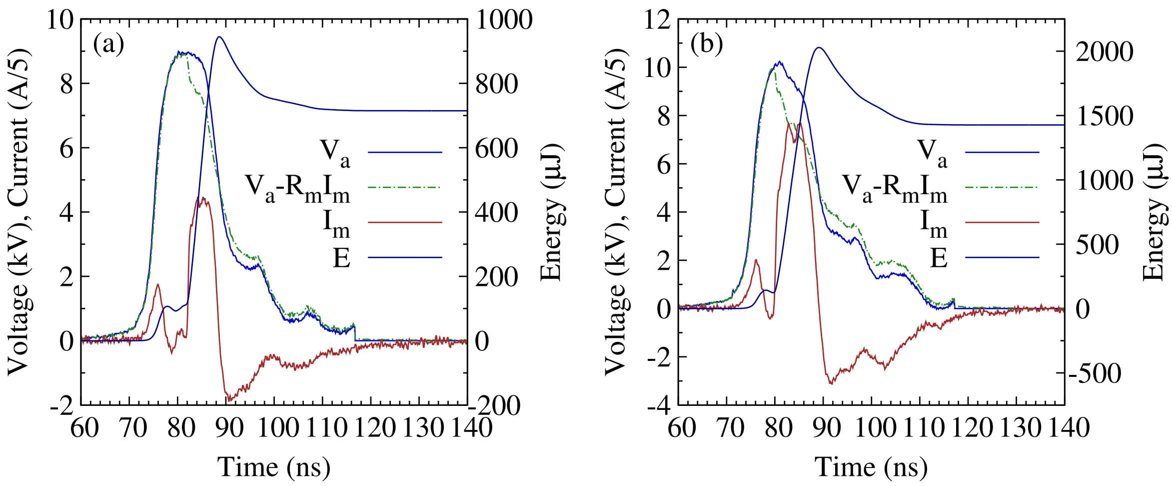

Figure II.24: Applied voltage, measured current and energy for a 8.9 kV voltage pulse (a) and for a 10.1 kV voltage pulse (b).

To further investigate the exposure conditions, we calculated the energy deposited per pulse. We calculated the energy from the experimental waveforms V_a and I_m by using Equation (I.19). Figure II.24 shows the results for two different voltages. The current and voltage waveforms were synchronized by shifting the measured current curve by −20 ns. The energy is around 0.71 mJ for a 8.9 kV incident voltage and 1.43 mJ for a 10.1 kV incident voltage. The energy depends on the voltage and current amplitudes. It also depends on the FWHM of the current pulse that is based on the discharge time-lag. In the given exposure conditions, the measured currents are repeatable in time-lag, amplitude and shape of the waveforms. The energy deposited per pulse is thus reproducible at a given applied electric field, as shown in Figure II.25. The values are consistent with that used in [Lin2015] (i.e. 0.9 mJ/pulse) for tumor cell killing by uniform ns-DBD plasma treatment.

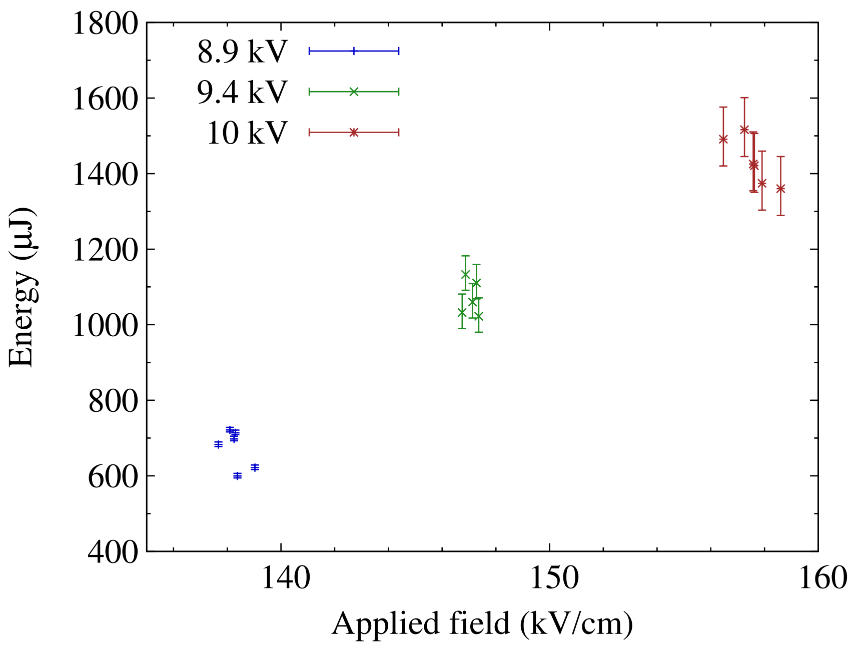

Figure II.25: Energy per pulse as a function of the applied electric field. The air gap distance is 650 µm.

II.4 Conclusion

In this chapter we described the experimental set-up of the ns-DBD exposure device. We discussed on the difficulty in electrically modeling the solution. Therefore we studied the ns-DBD device with a metallic cathode as a reference case. We proposed an equivalent circuit of the discharge device. A good agreement between experiments and simulations was found in the time domain, as well as in the frequency domain in the considered bandwidth (up to 300 MHz). Then we performed an electrical characterization of the discharge. We first performed a statistical study on the discharge. Subsequently we determined the electrical parameters of the discharge according to the equivalent electrical model. We calculated the discharge current, voltage across the air gap, voltage across the dielectric layer and energy deposited per pulse. We showed that the behavior of electrical parameters (discharge current, voltages across the air gap and the dielectric layer, and energy) are not sensitive to field applied to the air gap in the considered range. When a discharge ignites, the air capacitance suddenly discharges that leads to a peak in the discharge current. The discharge pulses ends as the applied voltage decreases. The current then falls to a negative value depending on the surface charge density on the dielectric layer. The surface charges are then driven in the remaining plasma channel. This leads to the presence of a discharge current in the circuit after the voltage pulse ends. We also showed that a Rompe-Weizel model, that is commonly used to model equivalent arc resistance, fits well with the ns-DBD electrical parameters. Finally, we carried out a preliminary study of the discharge in the exposure conditions. The measured currents are repeatable in terms of time-lag, amplitude and shape of the waveforms. The energy deposited per pulse is thus reproducible that is a key feature for the solution exposure. To further investigate the ns-DBD in the exposure conditions, it would be interesting to determine an equivalent electrical model of the solution.

Chapter III

Nanosecond-pulsed surface dielectric barrier discharge exposure device

Contents

III.1 Introduction

In this chapter, we present a ns-SDBD device for plasma treatment of biological medium. Common applications of ns-SDBDs are plasma-based flight control (Starikovskii et al., 2009; Takashima et al., 2011b; Bayoda et al., 2015; Moreau et al., 2016) and plasma combustion (Stepanyan et al., 2014; Nudnova et al., 2015). In this context the work of (Soloviev et al., 2017) can be considered relevant for our application. Ns-SDBDs were initiated by a high-voltage pulse of negative polarity, with a 20 ns FWHM, 2.5 ns rise front and 24kV of amplitude (48 kV applied voltage). The authors showed that the discharge starts at the edge of the HV electrode and propagates along the surface of the dielectric layer. Numerical simulation and experiments agreed in demonstrating that the discharge propagates as two successive ionization fronts. One develops during the rise time of the voltage pulse and contributes to charge the dielectric surface. The main energy deposition into the gas occurs at the stage of the leading edge and during the plateau. At the trailing edge, the discharge evolves as a streamer propagating above the dielectric surface. The height of the discharge is about 40 µm.

During plasma exposure, the biological sample faces the discharge device. By contrast to the DBD configuration, the discharge is not in direct contact with the surface of the solution. Ns-SDBD are known for inducing high values of electric field, up to 250 kV/cm (Shcherbanev, 2017). Under these conditions, a significant fraction of energy deposited into the discharge goes to electronic excitation of atoms, molecules and dissociation of molecules by direct electron impact. As a result, active species are efficiently generated. On the other hand, in ns-SDBD plasma actuators, compression waves in quiescent air are generated by fast localized heating during the nanosecond pulse (Starikovskii et al., 2009). Both first and second stroke of a single voltage pulse produce a current peak. It was then demonstrated in (Benard et al., 2012) that each of the peaks leads to the production of a pressure wave propagating in the surrounding medium. The results also indicate that the intensity of the pressure wave can be changed by the amplitude of applied pulse, by the rise time of the leading edge or by the period of HV pulses. This compression wave formation could strengthen the influence of long life active species on the biological sample.

Section III.2 details the exposure device that is integrated into the experimental set-up described in the Chapter I (Section I.2). We will propose an equivalent circuit of the exposure device. The determination of the component values will be detailed. In Section III.3 we will electrically characterize the discharge. As a reference case we will study the discharge generated by voltage pulses delivered by the 10 kV generator, without a Petri dish. Finally, we will carry out a preliminary study on the discharge in the exposure conditions in Section III.4. Some preliminary biological results will also be presented.

III.2 Experimental setup

III.2.1 Description

The ns-SDBD exposure device is shown in Figure III.1. The pulse generating, measurements and monitoring are performed as described in Chapter I. For experiments voltage pulses are delivered by the 10 kV generator. The exposure device in series with the measure resistor is inserted into the waveguide matched by the load impedance to ensure the propagation of the fast rising voltages pulses and to reduce reflection. The exposure device is connected to the supply coaxial cable with a HN connector, in parallel to the waveguide. This connexion length is minimized (around 5 cm) to reduce parasitic reflections. The exposure device is very similar to the DBD exposure device previously described. It consists in an HV electrode system separated by a dielectric layer. The active electrode as well as the biological solution are grounded for safe exposure. The dimensions of the device are adjusted to the Petri dish diameter.

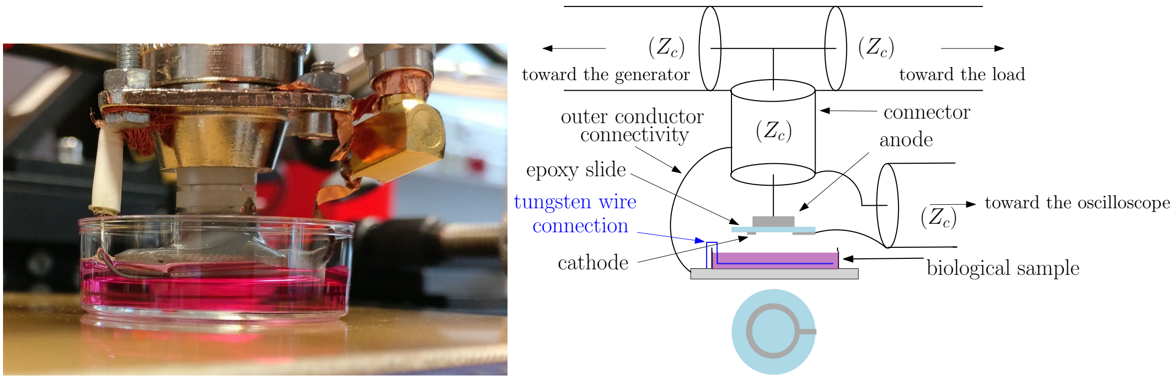

Figure III.1: Picture and schematic of the ns-DBD device with a Petri dish containing a biological sample (side view).

The discharge device is composed of :

- a high voltage electrode, the anode, connected to the inner conductor of the HV supply coaxial cable. The anode is made of a thin copper film in the form of a disk (66 µm thick) with a 0.75 cm radius. The high voltage conductor is enclosed in a dielectric material for insulation.
- the anode is covered by disk shaped epoxy plate as a dielectric barrier. The relative permittivity is 4.3. The dielectric layer is 1.6 mm thick with a radius of 1.5 cm. The radius is greater than the radius of the HV electrode to insure a complete electrical insulation. We adapted device dimensions to expose biological sample contained in a standard Petri dish of 1.75 cm radius.

- the cathode, which is a copper ring of 1 cm diameter and 66 µm thickness. Figure III.1 shows the electrode shape (in grey) on the dielectric disk (in blue). The cathode is connected to the outer conductor of the set-up via the measure resistor. The length of connection is minimized.

- the distance between the Petri dish and the discharge device can be varied by using a micrometric positioning sliding plate.

The Petri dish containing the biological sample is placed on the copper plane. The Petri dish is filled with a 2 ml constant volume of solution. The biological solution is a resistive conductor. It is connected to the outer conductor by a metallic wire immersed in the biological sample. By contrast to the DBD configuartion, the solution is not an electrode. Discharges develop at the surface of the dielectric layer in the vicinity of the cathode (at the inside and outside of the ring), with or without a Petri dish.

III.2.2 Frequency characterization

The S_{11} reflection coefficient was measured in order to determine the frequency performance of the experimental set-up. The real part and the imaginary part of the impedance are computed from the S_{11} parameter measurement. Results in Figure III.2 are given in two configurations : the device is in a free space and the device faces the Petri dish far from 500 µm (distance from the cathode).
A satisfactory matching corresponding to a S_{11} lower than −3 dB is achieved in both configurations in the considered bandwidth, i.e. up to 300 MHz. A complete mismatch is observed at 500 MHz without the Petri dish. This mismatch is less pronounced if the device faces the Petri dish. Then the S_{11} magnitude decreases from this frequency up to 1GHz in both configurations.The equivalent impedance shows a similar behavior for both configurations up to 300 MHz. The real part of the impedance is 50 Ω at low frequency whereas the imaginary part is very weak up to 100 MHz. Then the real part decreases because of the equivalent capacitance of the device. The imaginary part increases at the same time because of the parallel resonances observed beyond. A huge parallel resonance is marked at 450 MHz without the Petri dish, that causes the mismatch observed in the S_{11} parameter. This resonance corresponds to an electromagnetic mode of the exposure device. With the Petri dish, this resonance is weaker and appears at higher frequency (800 MHz). This can be due to the electrical losses to the biological solution. A serial resonance precedes each parallel resonance at 230 MHz with Petri dish and at 200 MHz without.

III.2.3 Equivalent electrical circuit

To determine the electrical parameters of ns-SDBDs, an equivalent model of the exposure device is determined. Each element of the experimental device set-up is associated with

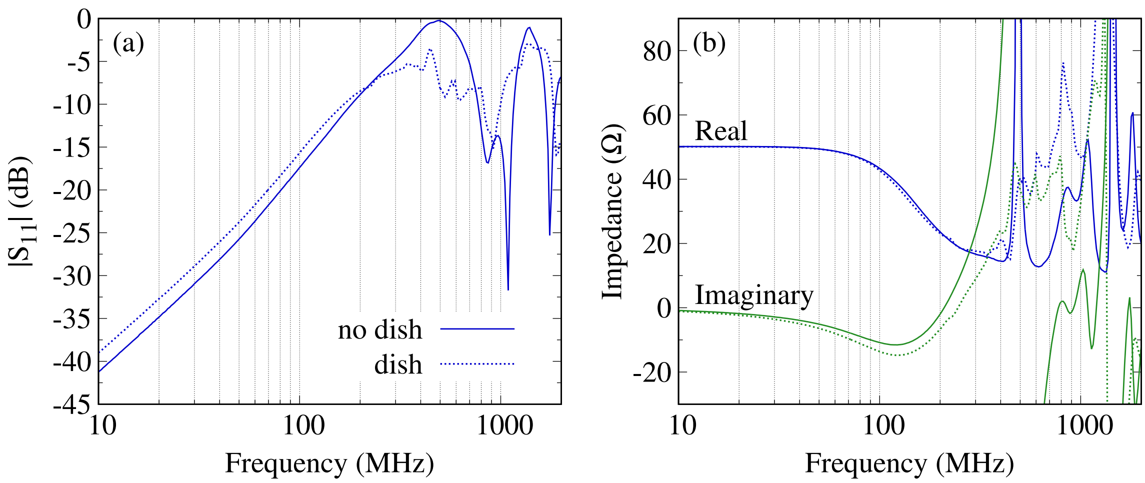

Figure III.2: Frequency domain measurements. Reflexion coefficient S_{11} (a) and impedance (b) of the ns-SDBD without a Petri dish (in straight line) and with the Petri dish containing the biological sample (in dotted line).

an electrical component as seen in Figure III.3 :

- the impedance due to the matched load, $Z_L \equiv Z_c = 50\ \Omega$, at the device location,
- the equivalent capacitor of the dielectric barrier between the anode and the air gap, C_{diel},
- the capacitance of the air volume where discharge develops, C_{air},
- the equivalent capacitor of the dielectric layer between the two electrodes, that is taken into account as a stray capacitance C_p,
- R_d that models the plasma resistance,
- the impedance due to the measure resistor, $R_m \equiv Z_c = 50\ \Omega$, at the device location,
- the stray inductance, L, due to wire connections.

The corresponding equivalent circuit is showed in Figure III.4 on the left side. This circuit is the same as the one of the DBD configuration, as discussed in Chapter I Section I.4). However, the determination of the three capacitances C_{air}, C_{diel} and C_p is challenging in SDBD configuration (Pang et al., 2014). Indeed, C_{air} and C_{diel} values increase in time as the discharge develops along the surface. However C_p is preponderant considering the device configuration. Its value is constant. Therefore we model the SDBD device by an equivalent capacitance, $C_{eq} \approx C_p$, as a first approach.

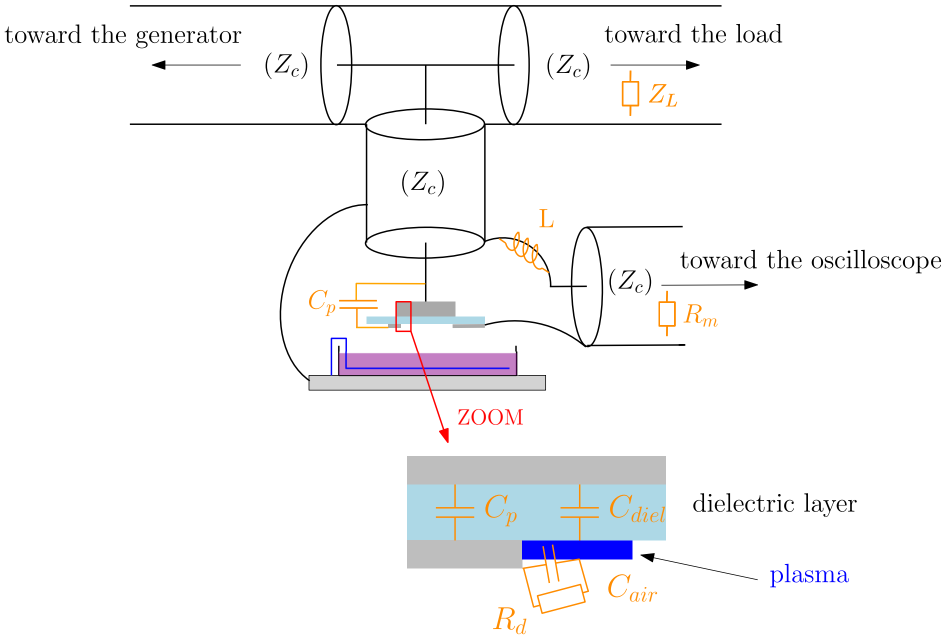

Figure III.3: Equivalent lumped elements of the exposure device.

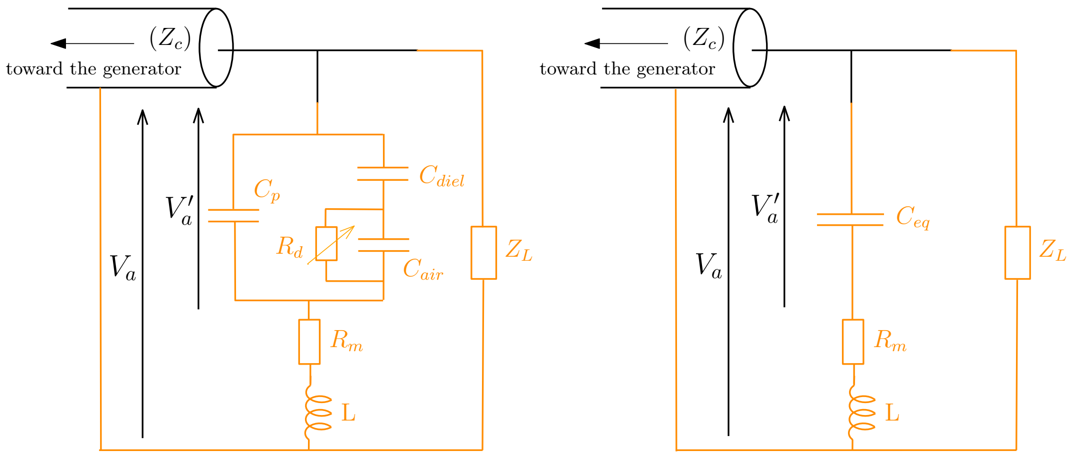

Figure III.4: Equivalent circuit of the electrical termination.

III.2.4 Determination of circuit element values

The determination of the element values is achieved by using circuit simulations. The electrical termination of the line is the proposed equivalent circuit of the ns-SDBD device. The line is 5.18 m long. The sending voltage is an experimental incident waveforms. We first compares numerical results to waveforms measured without a Petri dish facing the device.

The displacement current obtained in simulation is compared to the experimental one in Figure III.5. A satisfactory agreement is found for the set of values given in Table III.1. Slight differences appear in between the two pulses and on the amplitude of the second pulse. We focused on the accordance of the first current pulse. The comparison of equivalent impedances is also presented to complete the study. A good agreement is obtained up to 250 MHz. Beyond, the electromagnetic mode resonance can not be reproduced by using the proposed equivalent circuit. It should noted that the good agreement (in transient and frequency domains) is achieved by modeling the HF effect of connection with the stray inductance.

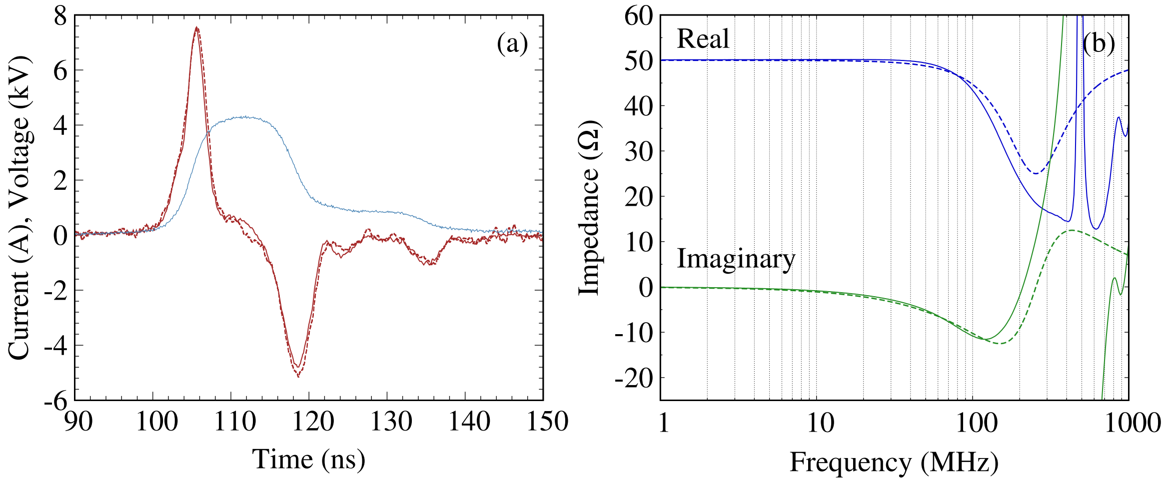

Figure III.5: Displacement current pulses (for a 4.3 kV voltage pulse) (a) and device impedance (b). Measurements in straight line and numerical results in dotted line.

without Petri dish		with Petri dish	
C_{eq} (pF)	L (nH)	C_{eq} (pF)	L (nH)
7	56	6.3	56

Table III.1: Elements circuit values of the ns-SDBD.

A similar study is performed when a Petri dish is located 500 µm below the the device. The experimental results are shown in Figure III.6 (in straight line). For a same voltage pulse, experimental currents are very similar. The equivalent impedances also present only slight differences below 250 MHz. The main difference occurs beyond : the resonance is very minimized when the Petri dish facing the device. Therefore we assume that the electrical influence of the dish on the ns-SDBD is weak. The same equivalent circuit is then used to model the ns-SDBD device with and without a Petri dish. Only the equivalent capacitance is adjusted (see in Figure III.1) to fit with experiments as shown in Figure III.5. Results are in good agreement in the time domain and in the frequency domain up to 250 MHz.

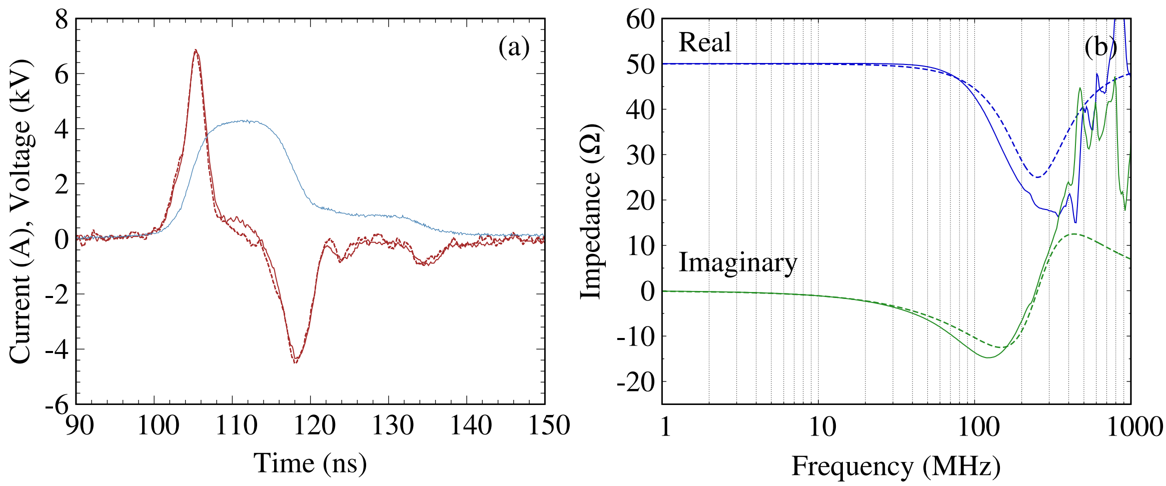

Figure III.6: Displacement current pulses (for a 4.3 kV voltage pulse) (a) and device impedance (b) with a Petri dish located 500 µm from the cathode. Measurements represented by a solid line and numerical results by a dotted line.

III.3 Electrical characterization of the discharge

Figure III.7 shows pictures of the discharge. The discharge uniformly develops from the cathode along the dielectric surface. Some darks areas are observed at concave irregularities of the electrode surface. The uniformity of the discharge cannot be discussed because of the long time exposure.

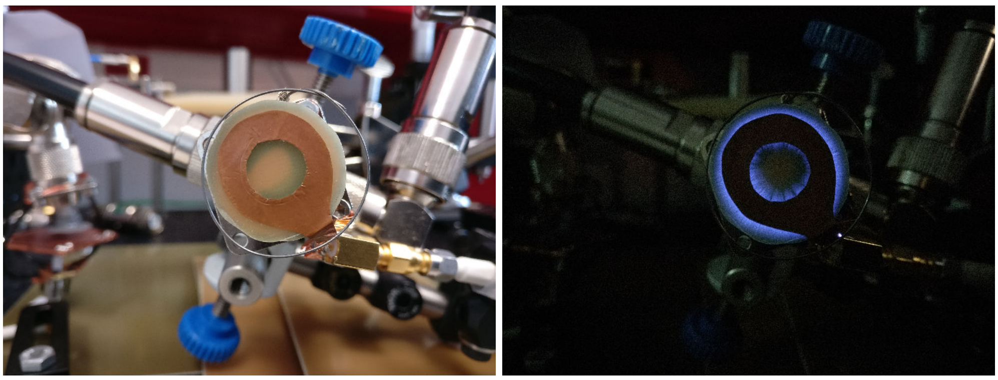

Figure III.7: Pictures of the ns-DBD. The exposure time is 4 seconds. The incident voltage magnitude is 9 kV and the repetition rate frequency is 10 Hz.

We study the discharge with single-shot recorded. The discharge is not sensitive to the pulse repetition rate in the considered frequency range (up to 100 Hz). In Section III.3.1 we present a statistical study on discharge time-lag and we describe the measured current pulses. In Section III.3.2 we will determine the energy deposited into plasma per pulse according to the equivalent electrical circuit. In Section III.3.3, we will propose circuit simulations in which the discharge is modeled by a resistance varying in time. This simplified model will provide a first approach of electrical parameters of the ns-SDBD. Finally, in Section III.4 we will study the discharge in the exposure conditions. The influence of the Petri dish is studied by varying the distance from the discharge device. Moreover, the 20 kV generator is used for plasma exposure as it is preferred to the 10 kV generator for a long-time used at a high repetition rate. So the influence of the voltage pulse, especially the rise time, is also studied. Finally preliminary biological results will be presented.

III.3.1 Statistical time lags and current measurement

For the experiments, the voltage pulses were delivered by the 10kV-generator. Pulses with different amplitudes were applied, from 4.3 kV to 7 kV. Figure III.8(a) shows the measured currents for a given incident voltage (6.1 kV). The maximum amplitude of the pulse due to the discharge (2.3 A) is very weak compared to the maximum of displacement current (12.5 A). As a consequence it is difficult to identify weak discharge activity. We estimate that discharges ignite when a 5.6 kV voltage pulse is applied. The inception voltage is defined as the minimum applied voltage for measuring a discharge current. A discharge activity can occur without inducing sufficiently high current to be measured. An optical UV light detection is clearly lacking for precise inception voltage measurement.

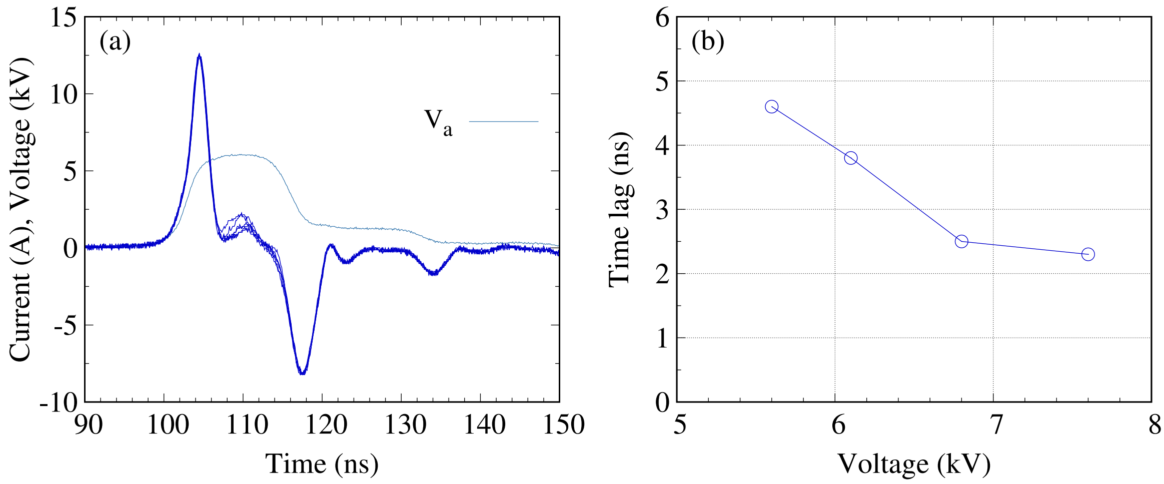

Figure III.8: Measured current I_m (a) and time lags as a function of the incident voltage (b).

If the applied voltage to the ns-SDBD device is too low, no discharge leading to a measurable current is observed. On the other hand when the applied voltage is too high, the discharge activity is mainly recorded in the trailing edge of the first displacement current pulse. Statistical variation of the time lag is thus only observed for a limited voltage range. Two examples of measurable statistics are given in Figure III.9. The estimated time lags are then 3.7 ns for 6.1 kV and 2.5 ns for 6.8 kV. The statistical time lag decreases with the applied voltage as shown in Figure III.8(b). The time lag decreases linearly by considering that the value found for the highest voltage is affected by the displacement current pulse. Moreover, the amplitude of the current pulse due to the discharge is typically greater as time lags decrease. It remains in a few amperes range.

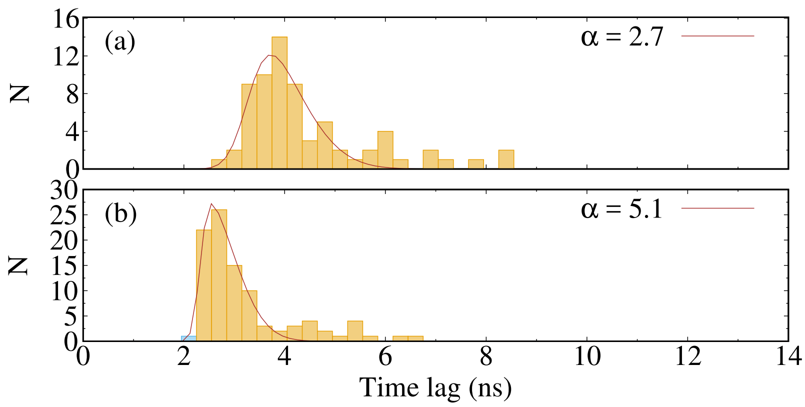

Figure III.9: Number of discharge occurences N as a function of the time lag. V = 6.1 *k*V (a) and V = 6.8 *k*V (b). α is the skewness factor determined by fitting.

III.3.2 Electrical parameters of the ns-SDBD

The issue in the electrical characterization of the ns-SDBD discharge is very different from the DBD configuration. The equivalent capacitances of C_{air} and C_{diel} can not be estimated in a simple way. Moreover, the voltage and current waveforms are very close from the corresponding waveforms when no discharge is present because of small discharge currents.

In this case the discharge current and the energy deposited per pulse are calculated as follows :

- the discharge current is estimated as the difference between the total measured current and the displacement current : $I_d = I_m - I_{dis}$, with $I_{dis} = C_{eq}\dfrac{dV'_a}{dt}$. The displacement current is calculated by using circuit simulations.
- For small discharge currents, the energy within the discharge is $E_{\text{discharge}} = E_{\text{total}} - E_{\text{no discharge}}$. The total energy per pulse is obtained by multiplying the measured voltage and current waveforms, and integrated in time during the pulse duration. $E_{\text{no discharge}}$ reflects parasitic losses.
  In our conditions we estimated that $E_{\text{no discharge}} << E_{\text{total}}$, the energy deposited into plasma per pulse is thus calculated from Equation (I.19)

$$E = \int_0^{\infty} V'_a(t) I_m(t)\, dt = \int_0^{\infty} (V_a(t) I_m(t) - R_m I_m^2(t))\, dt$$

The applied voltage pulse V_a is calculated from the incident pulse and the reflected one. The delay that we apply to the current is determined by synchronizing the measured current and displacement current obtained in simulations. The experimental delay between the voltage and current pulses is 24 ns. Figure III.10 shows the measured current and the applied voltage waveforms. The voltage magnitude is 6.8 kV. The reflection due to the discharge current is negligible, no drop in voltage is observed. The discharge current is obtained by the difference between measured current and numerical displacement current. The weak difference in the shape of these currents induces negative values before and after the discharge current pulse, at 102, 105 and 120 ns respectively. The discharge current rises in 2 ns up to 2.5 A. A peak is observed of 3 ns - FWHM. Then the current decreases and forms a plateau (1 A) till the voltage pulse ending.

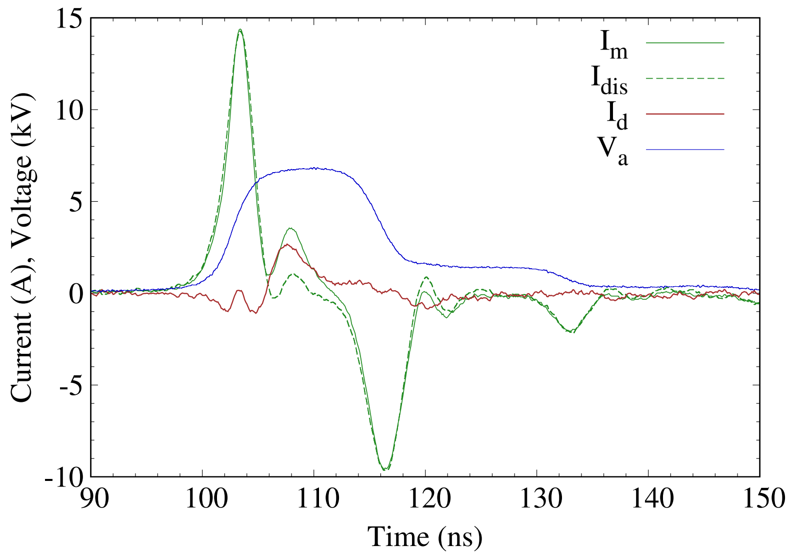

Figure III.10: Applied voltage, measured current, displacement current and discharge current for a 6.8 kV applied voltage.

Figure III.11(a) shows the energy deposited into the plasma per pulse for a 6.8 kV applied voltage. The statistics of the measured current for the given applied voltage is plotted. Statistical changes in the discharge current lead to dispersion in the limit value of the energy. The final energy is estimated to $60 \pm 10 \mu J$. The mean value of energy as a function of the applied voltage is plotted in Figure III.11 (b). The mean value is obtained by averaging five randomly distributed events for each voltage. The energy linearly increases with the voltage. The energy is in the range of plasma actuators in (Bayoda et al., 2015).

III.3.3 Circuit simulation

For applied voltages lower than 6.5 kV, the voltage and current waveforms are nearly indistinguishable from the corresponding waveforms when no discharge is present. In that

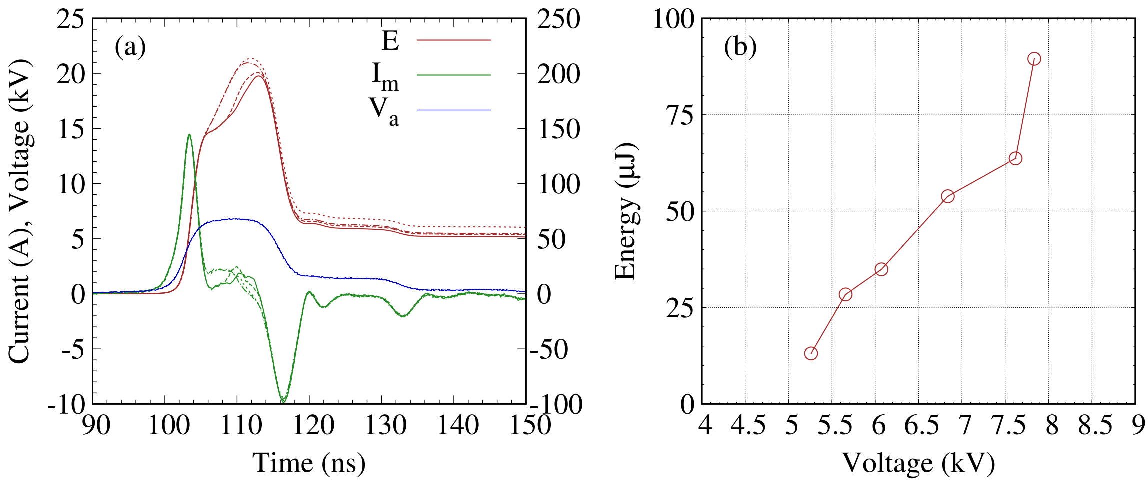

Figure III.11: Applied voltage, measured currents and energies for a 6.8 kV applied voltage (a). Mean values of energy as a function of applied voltage (b).

case we performed circuit simulations to support the experimental approach in the determination of current and energy for low currents. We consider the complete equivalent circuit of the ns-SDBD device shown in Figure III.4. The capacitances C_{air} and C_{diel} were estimated in comparison with experimental waveforms. The discharge is modeled by a simplified model of resistance rapidly varying in time. The value and the variation in time of the resistance were chosen to fit with experiments. In the given conditions, the discharge is switched on at 103.7 ns. The equivalent resistance of the discharge channel is set to 7.5 $k\Omega$.

Figure III.12 compares experiments and results obtained in simulations. C_{air} and C_{diel} are estimated to 0.4 pF and 12 pF respectively. These values are consistent with those experimentally determined in (Pang et al., 2014) in ns-SDBD actuator configuration. The stray capacitance is slightly decreased to 6.8 pF, and the stray inductance is unchanged. A satisfactory agreement is obtained between experimental and numerical results. Both discharge currents rise during the leading edge of the voltage pulse. The magnitude of the simulated current is 0.75 A and that obtained in experiments is 1 A. The pulses end when the voltage pulse decreases. The final energy obtained in simulation by considering the discharge current is also consistent.

To further investigate the discharge, Figure III.13 shows the voltages across the air gap and the dielectric layer, and the currents flowing through the capacitances. Results are very similar to those presented in Figure I.16 in Chapter I. The displacement current due to stray capacitance is dominant. It should be noted that to obtain a satisfactory accordance between simulation and experiments, the discharge is ignited one nanosecond before the rise of the measured current.

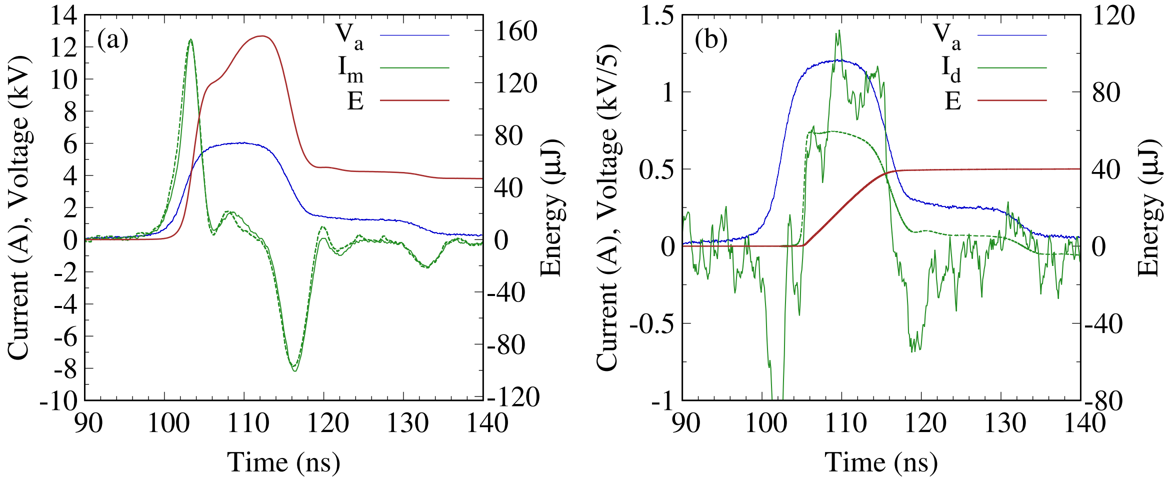

Figure III.12: Applied voltage, measured current (experiments in straight line and simulation in dotted line) and energy (a), applied voltage, discharge current (experiments represented by a solid line and simulation by a dotted line) and energy (b) for a 6.07 kV pulse.

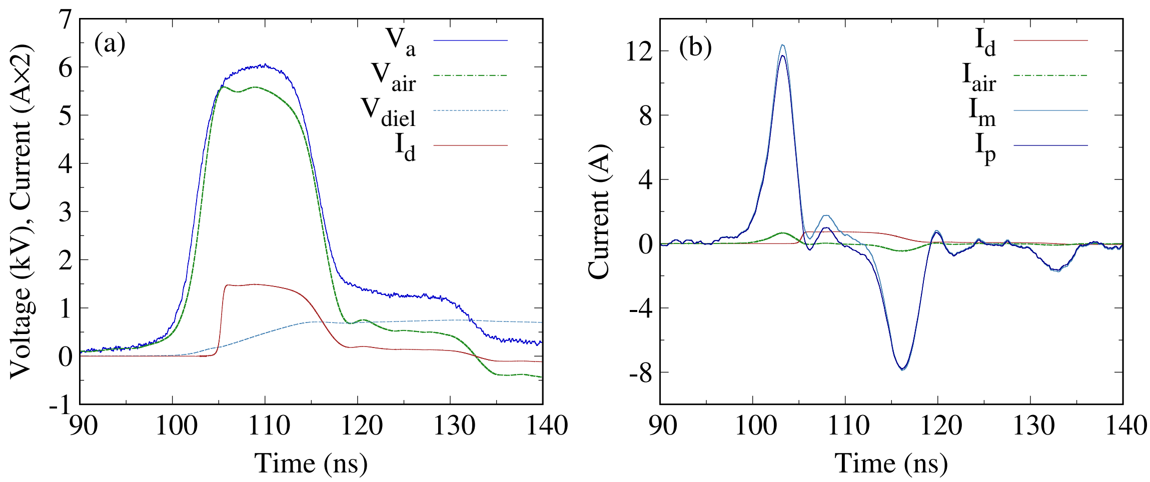

Figure III.13: Numerical results. Applied voltage pulse V_a, voltages over the air gap V_{air} and the dielectric layer V_{diel} (a). Discharge current I_d, measured current I_m and currents in C_p and C_{air} (b).

III.4 Discussion on biomedical applications

In this Section we study the discharge under the exposure conditions. The influence of the Petri dish is studied by varying the distance from the discharge device. Moreover, the 20 kV generator is used for plasma exposure as it is preferred to the 10 kV generator for a long-time used at a high repetition rate. So the influence of the voltage pulse, especially the rise time, is also studied. Finally preliminary results on plasma treatment of glioblastoma cells will be presented.

III.4.1 Influence of the exposure conditions

As a first step, the influence of the Petri dish containing the biological sample is studied by using the 10kV generator. Figure III.14 (a) compares the measured current with and without a Petri dish. The Petri dish faces the device at a distance of 500 µm from the cathode. The voltage is adjusted so that the two displacement currents are superimposed. Hence the difference between the two currents is only due to a change in the discharge activity. Figure III.14(b) shows the discharge current calculated by using element values of Table III.1. The discharge current ignited in the last phase of the leading edge of the voltage pulse. The rise time is 1.3 ns and the magnitude is 2.5 A.

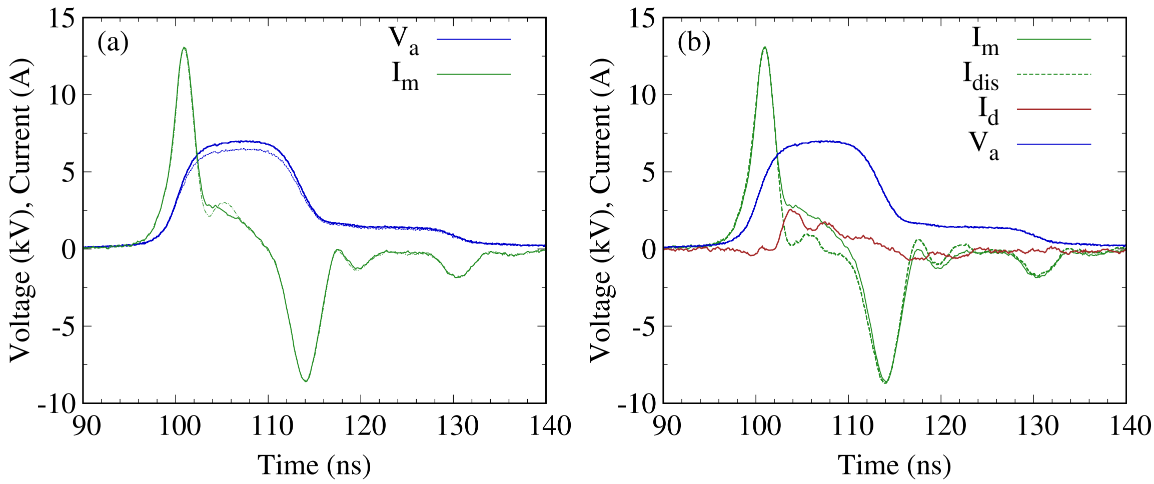

Figure III.14: Influence of the Petri dish. The Petri dish is at a distance of 500 μm from the device and V_a = 7 kV. With Petri dish (in straight line) and without Petri dish (in dotted line) for a same incident voltage (a). With a Petri dish: applied voltage, measured current (solid line), displacement current (dotted line) and discharge current (b).

Figure III.15 presents several currents measured for a same applied voltage (V_a = 6.8 kV). The changes in the measured current due to the discharge activity are very weak when varying the distance. Moreover no statistical variations in the discharge time lag is

observed. The measured discharge time lag is short, 1.2 ns, so the discharge current component is screened by the displacement current.
The Petri dish influences the discharge characteristics as it prevents any statistical distribution of the ignition time lag. Moreover, the discharge ignites earlier when the Petri dish faces the device, whatever the distance or the applied voltage. The petri dish facing the device may modify the transverse electric field distribution. Discharge ignition depends on the electrons multiplication factor along the field line (Pedersen, 1989).

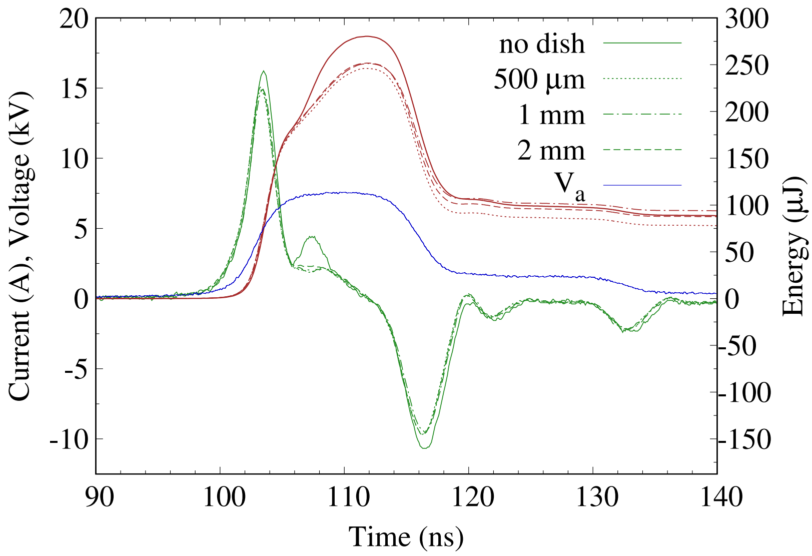

Figure III.15: Influence of the distance between the Petri dish and the exposure device. Applied voltage, measured current and energy deposited per pulse for a 7.6 kV applied voltage.

For technical considerations, the 20 kV generator will be used for plasma exposure. The influence of applying a voltage pulse with a shorter rise time of 2.35 ns is proposed in Figure III.16. The distance between the Petri dish and the device is 500 µm. The measured current is very different from the one described in Figure III.15. The displacement current is obviously two times higher. The current pulse due to the discharge is fully screened by the displacement current. Oscillations are due to the 450 MHz resonance circuit, that is beyond the bandwidth of the equivalent circuit (shown in Figure III.6). That's why the displacement current obtained in simulation is not in accordance with experiments. A complete characterization is thus challenging. The energy deposited is only given as the calculation is based on an accurate synchronization of waveforms. The final value of the energy is around 50 µJ.

The energy deposited into the discharge per pulse as a function of applied voltage is

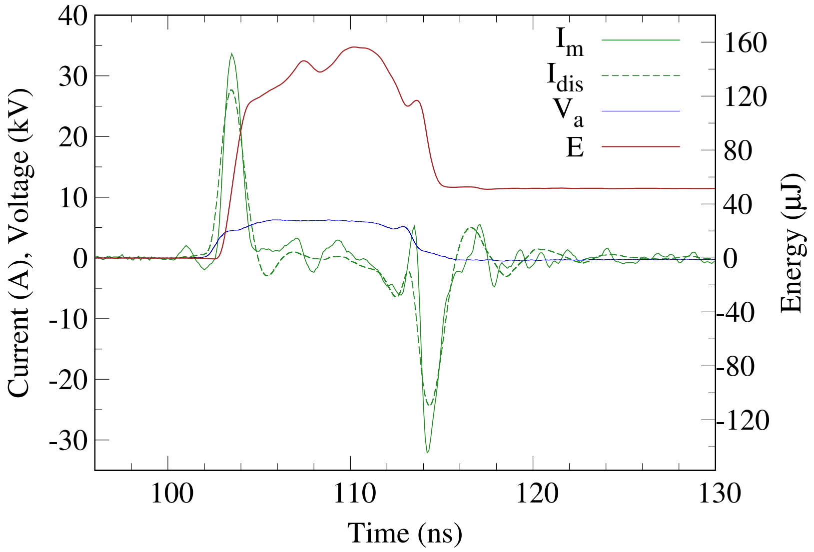

Figure III.16: Influence of the use of the 20 kV voltage pulse generator. The Petri dish is at a distance of 500 µm from the exposure device. Applied voltage, measured current, displacement current and energy for a 6.3 kV applied voltage.

shown in Figure III.17. The pulses are generated by the two generators. The Petri dish is 500 µm from the device. The variations of the energy against the applied voltage is nearly linear for each configuration. The Petri dish has a weak effect on the energy deposited. However a shorter rise time leads to an increase in the deposited energy by a factor of 2.

III.4.2 Preliminary study on biological targets

A preliminary study on the plasma treatment of biological samples was performed. Typically, U87 glioblastoma cells contained in a Petri dish are exposed to ns-SDBD. The applied voltage pulses were delivered by the 20 kV pulse generator. The rise time of voltage pulses is 2.35 ns and the FWHM is 11 ns.
Human U87-MG glioblastoma (ECACC, 89081402) cancer cell line was grown at 37°C in a 5% CO_2 humidified atmosphere in Modified Essential Medium with EARLES salts (10370-047, Gibco) supplemented with 10% fetal bovine serum (10500-064, Gibco), 0.2% Glucose (19002-013, Gibco), 2 mM L-glutamine (X0550, Dominique Dutscher), and 100 U.ml^{-1} penicillin 100 µg.ml^{-1} streptomycin (15140155, Gibco). The viability of cells was > 90% as determined by visual counts using Trypan Blue exclusion on a Malassez cell. Prior to ns-SDBD exposure, cells were trypsinized, washed, and suspended at 0.3 million ml^{-1} in complete medium in a volume of 2 ml in a 35 mm Petri dish (734 – 2417, VWR). The cells were homogeneously distributed.
The coupling of the discharge with the biological sample is governed by the distance between the active electrode and the sample surface. This distance is 500 µm. The Petri dish

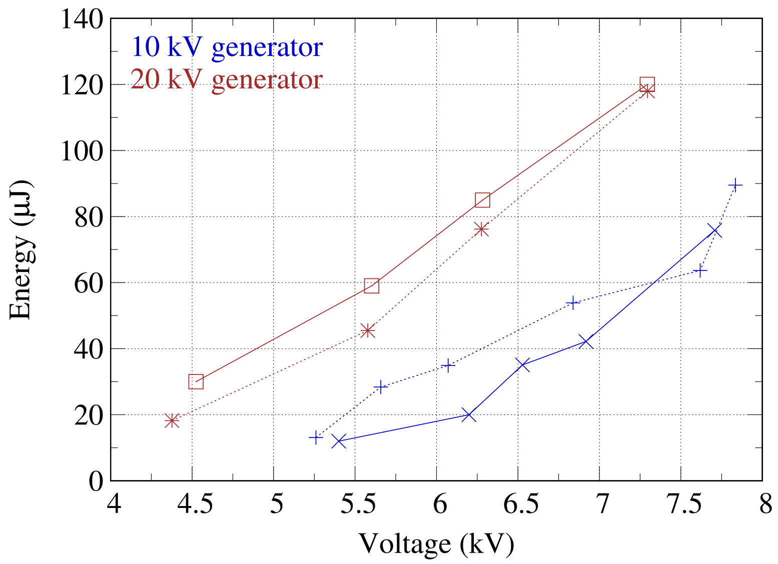

Figure III.17: Energy deposited per pulse as a function of the applied voltage amplitude V_a by using the 10 kV generator and the 20 kV generator, in two configurations : with Petri dish (in straight line) and without Petri dish (in dotted line).

is exposed during 30 min in a sterilized environment. The voltage amplitude varies between 5.9 kV and 7.4 kV, the repetition rate is 100 Hz. The control Petri dish (not exposed) is located at the vicinity of the exposure system during the experiment. The temperature of a MEM (Minimal Essential Medium) solution 500 µm from the exposure device has been measured during and after applying 6.5 kV pulses at 100 Hz for more than half an hour. The outcome was that no temperature change has been observed.

Immediately after exposure, all Petri dishes were incubated at 37°C in a 5% CO_2 humidified atmosphere for 15 – 16h. The total volume of each dish was transferred to 15 ml tubes after washing with PBS 1X (D8537, Sigma-Aldrich) and trypsinization. After 10 min centrifugation at 500 g, the pellet was resuspended in 500 µl supplemented medium. Cells were subsequently loaded with 3 nM of TMRM (TetramethylrhodamineMethyl Ester, FP – 41391A, FluoProbes) over 20 min at 37°C in a 5% CO_2 humidified atmosphere, and labeled with 3 µM of 7– AAD (7-Aminoactinomycin D, A9400 – 1MG) for 5 min at room temperature.

Determination of the mitochondrial membrane potential (ΔΨm by TMRM) and cell viability (by 7-AAD) was simultaneously measured by fluorescence using a flow cytometer (M*use*© Cell Analyzer, Millipore). Figure III.18 shows the results in terms of cells viability after exposure to ns-SDBD. The glioblastoma cells viability is presented in function of the energy deposited into plasma per pulse. According to this preliminary result the plasma has an influence on the viability of the cells under consideration from 90 µJ, namely 16 J in total. The range of the total energy can not be compared to that commonly used in ns-DBD as the interaction processes are different. These preliminary results are encouraging since the exposure conditions are not optimized.

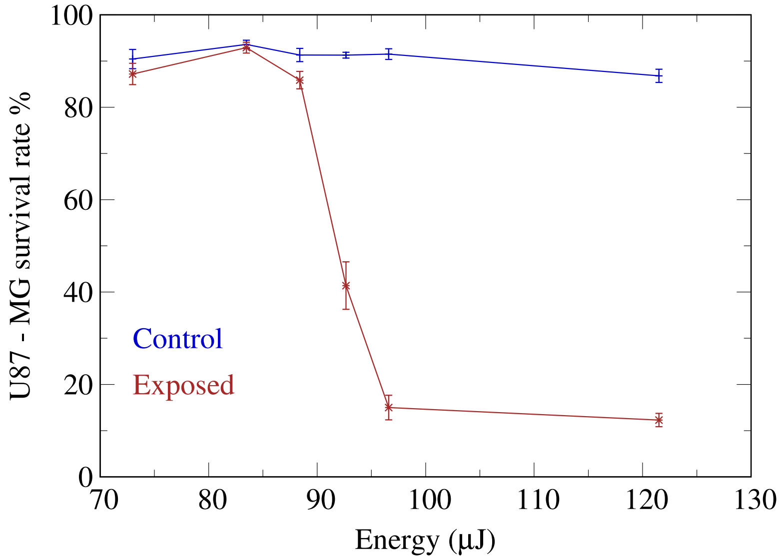

Figure III.18: Biological experiments of U87−MG glioblastoma cells. Viability of U87−MG glioblastoma cells after exposure (at a repetition frequency of 100 Hz during 30 min) as a function of the energy deposited per pulse.

III.5 Conclusion

In this chapter we described the experimental set-up of the ns-SDBD exposure device. We proposed an equivalent circuit of the discharge device. We discussed on the challenges to determine the equivalent capacitances of the air gap and of the dielectric layer. Therefore we proposed a simplified equivalent circuit. The SDBD device is then modeled by one equivalent capacitance, that is approximately the stray capacitance. A good agreement between experiments and simulations was found in the time domain, as well as in the frequency domain up to 250 MHz. The same equivalent circuit is used when a Petri dish faces the device with a small change in the capacitance value. Then we performed an electrical characterization of the discharge. We first performed a statistical study on the discharge. The discharge time-lag linearly reduces as the voltage increases. The discharge is characterized by small currents (few Amperes). The discharge current is obtained by subtracting the displacement current from the measured current. The energy deposited per pulse linearly increases with the voltage in a the range of several tens of μJ. Finally, we carried out a preliminary study on the discharge in the exposure conditions. When the Petri dish faces the device, the discharge ignites earlier without any statistical distribution of the discharge time lag, whatever the distance or the applied voltage. This could be explained by a change in the transverse electric field. Discharges were also generated by the 20 kV generator. The energy deposited per pulse was determined. We showed that the Petri dish has a weak effect on the energy whereas a shorter rise time of the voltage pulse leads to an increase in the deposited energy by a factor of 2. We showed preliminary results of glioblastoma cells treated by ns-SDBD. In the given conditions, the plasma has an influence on the viability of the cells under consideration.

Conclusion

In this Ph.D. thesis, the nanosecond pulse method was implemented to generate either DBD and SDBD for plasma treatment of biological samples. The plasma was created using short (10-14 ns of FWHM) high-voltage (up to 11 kV) pulses of fast rise times (2-5 ns depending on the pulse generator). Both exposure devices are designed in a same way. The dimensions allow plasma treatment of biological sample contained in a standard Petri dish. The voltage polarity is chosen for a safety use. Both exposure devices are inserted into the same experimental set-up which is a waveguide matched by a load impedance. The devices are interchangeable and can be used in a biological laboratory as no EMI disturbance was observed. A high voltage tap-off measures the incident and reflected voltage pulses. The current is measured via a measure resistor in series with the discharge device. It ensures a large frequency bandwidth required to measure nanosecond pulsed discharge current. We showed that the same equivalent circuit can model both devices.

In both cases we first studied the electrical characteristics of the discharge in a reference case without a Petri dish. In the ns-DBD configuration, the measured currents rise in 600 ps up to several tens of amperes. The FWHM depends on the voltage pulse duration. A negative current is still measured after the voltage pulse ends. The discharge current presents a sharp peak, then the current decays as the voltage pulse ends. Then a peak of current of the opposite polarity is observed. It has been related to the reversal of electric field sign in the gap because of a high surface density on the dielectric layer. The surface charges are then driven in the remaining plasma channel. This leads to a discharge current in the circuit after the voltage pulse ends. The energy deposited into plasma per pulse is in the order of millijoule. In the ns-SDBD configuration, the electrical characterization is more challenging as the discharge currents are very low (few amperes). We calculated the energy deposited into plasma per pulse in a range of tens of μJ.

Then, we have investigated the influence of the exposure conditions for the two devices. Although the discharges are very different, we have noticed that the presence of the solution promotes reproducible results in both cases. For the ns-DBD, the measured currents are repeatable in terms of time-lag, amplitude and shape of the signals. The energy deposited per pulse is thus reproducible that is a key feature for the solution exposure. For the ns-SDBD, the discharge ignites earlier without any statistical distribution of the discharge time lag whatever the distance or the applied voltage. We have suggested that the Petri dish changes the transverse electric field distribution. There is a weak influence on the final energy. However, the rise time of the voltage pulse has a strong influence on the energy. Finally, a preliminary study on treatment of biological samples by ns-SDBD plasma was performed. The glioblastoma cells viability was presented as a function of the energy deposited into plasma per pulse. According to this preliminary result the ns-SDBD plasma has an influence on the viability of the cells in the given conditions.

In a future work, the considered biological sample will be treated by the ns-DBD plasma. To complete the ns-DBD characterization, it should be interesting to consider ICCD fast imaging to study the uniformity of the discharge. In the ns-SDBD configuration, fast imaging could also be used to optically determine the area covered by the ns-SDBD in order to estimate the C_{diel} capacitance. Measuring the discharge current of the ns-SDBD in the exposure configurations is challenging because the discharge current is very low compared to the displacement current. An experimental set-up with a lower C_p value could be dedicated to study the discharge current. Replacing the classical coaxial connexion by a strip line could sufficiently reduce C_p value. On the other hand, preliminary effects with ns-SDBD plasma treatment should be confirmed and reinforced by experiments with other conditions in terms of discharge and biological parameters. The treatment distance and the time of exposure could be optimized. Moreover the measure of reactive oxygen species (ROS) density could give informations about the efficiency of the plasma treatment. In a future work both exposure devices could be combined with ns-PEF.

Conclusion

Dans ce travail de thèse, la méthode basée sur les décharges nanosecondes a été mise en oeuvre afin de concevoir deux dispositifs d'exposition plasma, basés sur les décharges ns-DBD et ns-SDBD, pour le domaine bio-médical. Le plasma de décharge est créé à l'aide d'impulsions très courtes (de 10 à 14 ns de largeur à mi-hauteur) haute tension (jusqu'à 11 kV) et de temps de montée très brefs (2-5 ns). Les deux systèmes d'exposition ont été conçus selon la même stratégie. Leurs dimensions permet de traiter des cellules en culture au sein d'une solution biologique dans une boite de Pétri classique. La polarité de l'électrode active pour le traitement est sécurisée. Les deux systèmes s'insèrent dans un même système d'ondes guidées terminé par une impédance d'adaptation. Ils sont interchangeables, et peuvent être utilisés dans un laboratoire de recherche en biologie grâce à des émissions parasites très réduites. Un diviseur de tension permet de mesurer l'impulsion de tension incidente et réfléchie. Le courant de décharge est mesuré via une résistance de mesure placée en série avec le système d'électrodes. La dispositif permet de mesurer des courants de décharge de temps de montée inférieur à la nanoseconde. D'autre part, nous avons montré que les deux systèmes peuvent être modélisés par le même schéma électrique équivalent.

Les caractéristiques électriques des décharges ont été obtenues sans boîte de Pétri, comme cas de référence, pour les deux systèmes d'exposition plasma. En configuration ns-DBD, le courant mesuré a un temps de montée de 600 ps et une amplitude de plusieurs dizaines d'Ampères. La décroissance du courant est liée à celle de l'impulsion de tension appliquée. Un courant d'amplitude négative est toujours enregistré après la fin de l'impulsion de tension. Le courant de décharge comporte tout d'abord un pic étroit, puis décroît et chute à la fin de l'impulsion de tension. Un pic d'amplitude négative est alors observé. Cette composante négative est due à l'inversion du champ électrique dans l'intervalle, causée par le stockage important de charges à la surface du diélectrique. Les charges sont alors transportées dans le canal de décharge résiduel. L'ordre de grandeur de l'énergie déposée par la décharge par impulsion est de l'ordre du mJ. Dans le cas de la ns-SDBD, une caractérisation électrique de la décharge s'avère plus complexe, car les courants mesurés sont de faible amplitude (quelques ampères). Nous avons calculé l'énergie déposée dans le plasma par la décharge, elle est de l'ordre de quelques dizaines de microjoules par impulsion.

Ensuite, nous avons étudié l'influence des conditions d'exposition sur la décharge pour les deux systèmes. Bien que les régimes de décharge soient différents entre ces deux systèmes, nous avons noté que la présence de la solution biologique dans la boite de Pétri est à l'origine d'une meilleure reproductibilité de la décharge. Dans le cas des décharges ns-DBD, les courants de décharges sont reproductibles en termes de temps d'apparition,

d'amplitude et d'allure. L'énergie déposée par la décharge est par conséquent aussi reproductible, ce qui est appréciable pour une exposition plasma.
Dans la configuration ns-SDBD, la décharge s'initie plus tôt sans dispersion statistique, quelle que soit la distance à laquelle se trouve la surface de la solution à traiter. On peut penser que la présence de la boîte de Pétri modifie les lignes de champ électrique en surface de diélectrique. L'influence de la présence de la solution sur l'énergie déposée par la décharge est faible. Par contre, le temps de montée de l'impulsion de tension a une influence importante sur l'énergie déposée. Enfin, des résultats préliminaires sur le traitement d'échantillons biologiques sont présentés. La viabilité de cellules cancéreuse de type glioblastome est étudiée en fonction de l'énergie déposée par la décharge ns-SDBD. Ces résultats montrent que le plasma généré a une influence sur la viabilité des cellules exposées, dans les conditions de l'étude.

Ce travail doit se poursuivre par l'exposition de cellules cancéreuses dans le cas du système ns-DBD. Pour compléter les caractérisations électriques de la décharge ns-DBD, il serait intéressant d'étudier l'uniformité de la décharge par imagerie rapide. En configuration ns-SDBD, l'imagerie rapide pourrait aussi aider à la détermination de la surface occupée par la décharge en surface de diélectrique, et ainsi obtenir un ordre de grandeur de la capacité diélectrique équivalente. Par ailleurs, le courant de déplacement mesuré pour la ns-SDBD est plus important que le courant de décharge, ce qui rend la détermination de ce dernier difficile à réaliser. Un nouveau montage à faible capacité parasite pourrait alors être mis au point pour étudier le courant de décharge. D'autre part, les résultats biologiques préliminaires obtenus par exposition avec le système ns-SDBD devront être reproduits. Les conditions d'exposition devront également être optimisées en termes de distance de traitement et de temps d'exposition. Enfin, la mesure de densité de ROS pourrait donner des informations sur l'efficacité du traitement plasma. A long terme, l'exposition plasma devrait être combinée à l'application de champs électriques pulsés nanosecondes.

Bibliography

Adamovich, I, S D Baalrud, A Bogaerts, P J Bruggeman, M Cappelli, V Colombo, U Czarnetzki, U Ebert, J G Eden, P Favia, D B Graves, S Hamaguchi, G Hieftje, M Hori, I D Kaganovich, U Kortshagen, M J Kushner, N J Mason, S Mazouffre, S Mededovic Thagard, H R Metelmann, A Mizuno, E Moreau, A B Murphy, B A Niemira, G S Oehrlein, Z L Petrovic, L C Pitchford, P U Pu, S Rauf, O Sakai, S Samukawa, S Starikovskaia, J Tennyson, K Terashima, M M Turner, M C M van de Sanden, and A Vardelle. "The 2017 Plasma Roadmap: Low temperature plasma science and technology". In: *Journal of Physics D: Applied Physics* 50.32 (2017), p. 323001.

Anikin, N. B., S. M. Starikovskaia, and A. Yu. Starikovskii. "Study of the oxidation of alkanes in their mixtures with oxygen and air under the action of a pulsed volume nanosecond discharge". In: *Plasma Physics Reports* 30.12 (2004), pp. 1028–1042. DOI: 10.1134/1.1839956.

Arnaud-Cormos, D., S. Kohler, D. Bessières, R.P. O'Connor, J. Paillol, and P. Leveque. "Electrical measurements for nanosecond repetitive pulsed discharges". In: *IEEE Transactions on Plasma Science* 42.7 (2014), pp. 1909–1916. DOI: 10.1109/TPS.2014.2324286.

Ayan, H., D Staack, G Fridman, A Gutsol, Y Mukhin, A Starikovskii, A Fridman, and G Friedman. "Application of nanosecond-pulsed dielectric barrier discharge for biomedical treatment of topographically non-uniform surfaces". In: *Journal of Physics D: Applied Physics* 42.12 (2009), p. 125202. URL: http://stacks.iop.org/0022-3727/42/i=12/a=125202.

Babaeva, N Y and M J Kushner. "Intracellular electric fields produced by dielectric barrier discharge treatment of skin". In: *Journal of Physics D: Applied Physics* 43.18 (2010), p. 185206.

Bardet, Sylvia M., Lynn Carr, Malak Soueid, Delia Arnaud-Cormos, Philippe Leveque, and Rodney P. O'Connor. "Multiphoton imaging reveals that nanosecond pulsed electric fields collapse tumor and normal vascular perfusion in human glioblastoma xenografts". In: *Scientific Reports* 6 (Oct. 2016), p. 34443.

Bayoda, K.D., N. Benard, and E. Moreau. "Elongating the area of plasma/fluid interaction of surface nanosecond pulsed discharges". In: *Journal of Electrostatics* 74 (2015), pp. 79–84. DOI: https://doi.org/10.1016/j.elstat.2014.12.004.

Bazinette, Rémy, Jean Paillol, Jean-François Lelièvre, and Françoise Massines. "Atmospheric Pressure Radio-Frequency DBD Deposition of Dense Silicon Dioxide Thin Film". In: *Plasma Processes and Polymers* 13.10 (2016), pp. 1015–1024. DOI: 10.1002/ppap.201600038.

Benard, N., N. Zouzou, A. Claverie, J. Sotton, and E. Moreau. "Optical visualization and electrical characterization of fast-rising pulsed dielectric barrier discharge for airflow control applications". In: *Journal of Applied Physics* 111.3 (2012), p. 033303. DOI: 10.1063/1.3682568.

Bessières, D., J. Paillol, and N. Soulem. "Negative corona triggering in air". In: *Journal of Applied Physics* 95.8 (2004), pp. 3943–3951. DOI: 10.1063/1.1667599.

Boisvert, J-S, J Margot, and F Massines. "Transitions of an atmospheric-pressure diffuse dielectric barrier discharge in helium for frequencies increasing from kHz to MHz". In: *Plasma Sources Science and Technology* 26.3 (2017), p. 035004.

Bouzidi, M C, X Bonnin, N Naudé, H Piquet, A Belinger, and N Gherardi. "Maximization of the working domain of an Atmospheric Pressure Townsend Discharge (APTD) using a current-source static converter". In: *Journal of Physics: Conference Series* 550.1 (2014), p. 012044.

Brandenburg, Rony. "Dielectric barrier discharges: progress on plasma sources and on the understanding of regimes and single filaments". In: *Plasma Sources Science and Technology* 26.5 (2017), p. 053001.

Carr, L, S Bardet, R Burke, D Arnaud-Cormos, P Leveque, and R P O'Connor. "Calcium-independent disruption of microtubule dynamics by nanosecond pulsed electric fields in U87 human glioblastoma cells". In: *Scientific Report 7* 41267 (2017).

Chen, Zhitong, Hayk Simonyan, Xiaoqian Cheng, Eda Gjika, Li Lin, Jerome Canady, Jonathan H. Sherman, Colin Young, and Michael Keidar. "A Novel Micro Cold Atmospheric Plasma Device for Glioblastoma Both In Vitro and In Vivo". In: *Cancers* 9.61 (2017). DOI: 10.3390/cancers9060061.

Correale, G., R. Winkel, and M. Kotsonis. "Energy deposition characteristics of nanosecond dielectric barrier discharge plasma actuators: Influence of dielectric material". In: *Journal of Applied Physics* 118.8 (2015), p. 083301. DOI: 10.1063/1.4929362.

Dawson, R. and J. Little. "Characterization of nanosecond pulse driven dielectric barrier discharge plasma actuators for aerodynamic flow control". In: *Journal of Applied Physics* 113.10 (2013), p. 103302. DOI: 10.1063/1.4794507.

Fridman, Gregory, Gary Friedman, Alexander Gutsol, Anatoly B. Shekhter, Victor N. Vasilets, and Alexander Fridman. "Applied Plasma Medicine". In: *Plasma Processes and Polymers* 5.6 (2008), pp. 503–533. DOI: 10.1002/ppap.200700154.

Fridman, Gregory, Alexey Shereshevsky, Monika M. Jost, Ari D. Brooks, Alexander Fridman, Alexander Gutsol, Victor Vasilets, and Gary Friedman. "Floating Electrode Dielectric Barrier Discharge Plasma in Air Promoting Apoptotic Behavior in Melanoma

Skin Cancer Cell Lines". In: *Plasma Chemistry and Plasma Processing* 27.2 (2007), pp. 163–176. DOI: 10.1007/s11090-007-9048-4.

Gibalov, V I and G J Pietsch. "The development of dielectric barrier discharges in gas gaps and on surfaces". In: *Journal of Physics D: Applied Physics* 33.20 (2000), p. 2618.

Grover, Frederick W. "Inductance calculations". In: *Dover publications, inc. Mineola New-York* (2009).

Haas, Alexis J., Yann Le Page, Maxim Zhadobov, Ronan Sauleau, Yves Le Dréan, and Christian Saligaut. "Effect of acute millimeter wave exposure on dopamine metabolism of NGF-treated PC12 cells". In: *Journal of Radiation Research* 58.4 (2017), pp. 439–445. DOI: 10.1093/jrr/rrx004.

Han, D and Cho J M. "Antitumorigenic effect of atmospheric-pressure dielectric barrier discharge on human colorectal cancer cells via regulation of Sp1 transcription factor". In: *Sci. Rep. 7* 43081 (2017).

Jobava, R., D. Pommerenke, D. Karkashadze, P. Shubitidze, R. Zaridze, S. Frei, and M. Aidam. "Computer simulation of ESD from voluminous objects compared to transient fields of humans". In: *IEEE Transactions on Electromagnetic Compatibility* 42.2 (2000). DOI: 10.1109/15.831704.

Keidar, Michael, Alex Shashurin, Olga Volotskova, Mary Ann Stepp, Priya Srinivasan, Anthony Sandler, and Barry Trink. "Cold atmospheric plasma in cancer therapy". In: *Physics of Plasmas* 20.5 (2013), p. 057101. DOI: 10.1063/1.4801516.

Kenaan, M., S. El Amari, A. Silve, C. Merla, L.M. Mir, V. Couderc, D. Arnaud-Cormos, and Leveque P. "Characterization of a 50-ohms exposure setup for high-voltage nanosecond pulsed electric field bioexperiments." In: *IEEE Trans Biomed Eng* 58 (2011), pp. 207–214.

Kogelschatz, Ulrich. "Dielectric-Barrier Discharges: Their History, Discharge Physics, and Industrial Applications". In: *Plasma Chemistry and Plasma Processing* 23.1 (2003), pp. 1–46. ISSN: 1572-8986. DOI: 10.1023/A:1022470901385.

Kong, M.G., G Kroesen, G Morfill, T Nosenko, T Shimizu, J van Dijk, and J L Zimmermann. "Plasma medicine: an introductory review". In: *New Journal of Physics* 11.11 (2009), p. 115012.

Lin, Abraham, Billy Truong, Sohil Patel, Nagendra Kaushik, Eun Ha Choi, Gregory Fridman, Alexander Fridman, and Vandana Miller. "Nanosecond-Pulsed DBD Plasma-Generated Reactive Oxygen Species Trigger Immunogenic Cell Death in A549 Lung Carcinoma Cells through Intracellular Oxidative Stress". In: *International Journal of Molecular Sciences* 18.966 (2017).

Lin, Abraham, Billy Truong, Arthur Pappas, Lawrence Kirifides, Ahmed Oubarri, Shuyang Chen, Shaojun Lin, Danil Dobrynin, Gregory Fridman, Alexander Fridman, Nianli Sang, and Vandana Miller. "Uniform Nanosecond Pulsed Dielectric Barrier Discharge Plasma Enhances Anti-Tumor Effects by Induction of Immunogenic Cell Death in Tumors and Stimulation of Macrophages". In: *Plasma Processes and Polymers* 12.12 (2015), pp. 1392–1399. ISSN: 1612-8869. DOI: 10.1002/ppap.201500139.

Liu, C., D. Dobrynin, and A. Fridman. "Uniform and non-uniform modes of nanosecond-pulsed dielectric barrier discharge in atmospheric air: fast imaging and spectroscopic measurements of electric fields". In: *Journal of Physics D: Applied Physics* 47.25 (2014), p. 252003.

Liu, S. and M. Neiger. "Electrical modelling of homogeneous dielectric barrier discharges under an arbitrary excitation voltage". In: *Journal of Physics D: Applied Physics* 36.24 (2003), p. 3144.

Ma, Yonghao, Chang Seung Ha, Seok Won Hwang, Hae June Lee, Gyoo Cheon Kim, Kyo-Won Lee, and Kiwon Song. "Non-Thermal Atmospheric Pressure Plasma Preferentially Induces Apoptosis in p53-Mutated Cancer Cells by Activating ROS Stress-Response Pathways". In: *PLOS ONE* 9.4 (Apr. 2014), pp. 1–14. DOI: 10.1371/journal.pone.0091947.

Moreau, E., A. Debien, N. Benard, and N. Zouzou. "Nanosecond-Pulsed Dielectric Barrier Discharge Plasma Actuator for Airflow Control Along an NACA0015 Airfoil at High Reynolds Number". In: *IEEE Transactions on Plasma Science* 44.11 (2016), pp. 2803–2811. DOI: 10.1109/TPS.2016.2603226.

Naudé, N., J.-P. Cambronne, N. Gherardi, and F. Massines. "Electrical model of an atmospheric pressure Townsend-like discharge (APTD)". In: *EPJ Applied Physics* 29.2 (2005), pp. 173–180. DOI: 10.1051/epjap:2004197.

Nudnova, M. M, S. V Kindysheva, N. L Aleksandrov, and A. Yu Starikovskii. "Fast gas heating in N2/O2 mixtures under nanosecond surface dielectric barrier discharge: the effects of gas pressure and composition". In: *Philosophical Transactions of the Royal Society of London A: Mathematical, Physical and Engineering Sciences* 373.2048 (2015). DOI: 10.1098/rsta.2014.0330.

Pai, David. "Nanosecond Repetitively Pulsed Plasmas in Preheated Air at Atmospheric Pressure". In: *PhD Thesis Ecole CentraleParis, France* (2008).

Pang, Lei, Kun He, Dongxu Di, Qiaogen Zhang, and Chunliang Liu. "Capacitances and energy deposition curve of nanosecond pulse surface dielectric barrier discharge plasma actuator". In: *Review of Scientific Instruments* 85.5 (2014), p. 053501. DOI: 10.1063/1.4871552.

Pedersen, A. "On the electrical breakdown of gaseous dielectrics-an engineering approach". In: *IEEE Transactions on Electrical Insulation* 24.5 (1989), pp. 721–739. DOI: 10.1109/14.42156.

Ranieri, Pietro, Lin, Shrivastav Ravi, Wang Mingkun, Abraham Lin, Alexander Fridman, and Gregory Fridman. "Nanosecond pulsed Dielectric Barrier Discharge induced Anti-Tumor Effects Propagate Through the depth of Tissue via Intracellular Signaling". In: *plasma medicine* 7 (2017).

Shao, T., Long Kaihua, Zhang Cheng, Wang Jue, Zhang Dongdong, Yan Ping, and Zhang Shichang. "Electrical characterization of dielectric barrier discharge driven by repetitive nanosecond pulses in atmospheric air". In: *Journal of Electrostatics* 67.2 (2009), pp. 215 –221. DOI: https://doi.org/10.1016/j.elstat.2008.12.001.

Shcherbanev, Sergey. "Filamentary nanosecond surface dielectric barrier discharge at elevated pressures. Streamer-to-filamentary transition and application for plasma assisted combustion." In: *PhD Thesis Ecole normale supérieure Paris-Saclay, France* (2017).

Soloviev, V R, V M Krivtsov, S A Shcherbanev, and S M Starikovskaia. "Evolution of nanosecond surface dielectric barrier discharge for negative polarity of a voltage pulse". In: *Plasma Sources Science and Technology* 26.1 (2017), p. 014001.

Soueid, M., M. Dobbelaar, S. Bentouati, S. M. Bardet, R. P. O'Connor, D. Bessières, J. Paillol, P. Leveque, and D. Arnaud-Cormos. "Delivery devices for exposure of biological cells to nanosecond pulsed electric fields". In: *Medical & Biological Engineering & Computing* (2017). DOI: 10.1007/s11517-017-1676-0.

Starikovskaia, S.M., K. Allegraud, O. Guaitella, and A. Rousseau. "On electric field measurements in surface dielectric barrier discharge". In: *Journal of Physics D: Applied Physics* 43.12 (2010), p. 124007.

Starikovskii, A Yu, A A Nikipelov, M M Nudnova, and D V Roupassov. "SDBD plasma actuator with nanosecond pulse-periodic discharge". In: *Plasma Sources Science and Technology* 18.3 (2009), p. 034015.

Stepanyan, S A, V R Soloviev, and S M Starikovskaia. "An electric field in nanosecond surface dielectric barrier discharge at different polarities of the high voltage pulse: spectroscopy measurements and numerical modeling". In: *Journal of Physics D: Applied Physics* 47.48 (2014), p. 485201.

Stoffels, E, I E Kieft, REJ Sladek, L J M van den Bedem, E P van der Laan, and M Steinbuch. "Plasma needle for in vivo medical treatment: recent developments and perspectives". In: *Plasma Sources Science and Technology* 15.4 (2006), S169.

Takashima, K., Y. Zuzeek, W.R. Lempert, and I.V. Adamovich. "Characterization of a surface dielectric barrier discharge plasma sustained by repetitive nanosecond pulses". In: *Plasma Sources Science and Technology* 20.5 (2011), p. 055009.

Takashima, Keisuke (Udagawa), Yvette Zuzeek, Walter R Lempert, and Igor V Adamovich. "Characterization of a surface dielectric barrier discharge plasma sustained by repetitive nanosecond pulses". In: *Plasma Sources Science and Technology* 20.5 (2011), p. 055009.

Vandamme, Marc, Eric Robert, Stéphanie Lerondel, Vanessa Sarron, Delphine Ries, Sébastien Dozias, Julien Sobilo, David Gosset, Claudine Kieda, Brigitte Legrain, Jean-Michel Pouvesle, and Alain Le Pape. "ROS implication in a new antitumor strategy based on nonthermal plasma". In: *International Journal of Cancer* 130.9 (2012), pp. 2185–2194. DOI: 10.1002/ijc.26252.

Weltmann, K-D and Th von Woedtke. "Plasma medicine". In: *Plasma Physics and Controlled Fusion* 59.1 (2017), p. 014031.

Zhang, Q., J Zhu, J Jia, F Tao, and L Yang. "Design of a current transducer with a magnetic core for use in measurements of nanosecond current pulses". In: *Measurement Science and Technology* 17.4 (2006), p. 895.